Growth and structure of graphene on metal and growth of organized nanostructures on top

Fabien Jean

Growth and structure of graphene on metal and growth of organized nanostructures on top

Fabien Jean

May 13, 2015

Contents

Chapter 0

Introduction

0.1 Graphene onto a metallic substrate

Graphene, a monolayer of graphite, is composed of carbon atoms arranged in a honeycomb lattice. The study of its unique electronic and optical properties from 2004, made possible by a simple preparation technique, was awarded the Novel Prize in Physics in 2010. From 2006-2007, this large effort worldwide stimulated a renewal in the studies devoted to epitaxial graphene on a metal, which was rapidly identified as an efficient method for large-area production of high quality graphene, and also was the matter of intense activities exploiting surface science approaches to address the various properties of graphene and of advanced systems based on graphene, for instance ordered lattice of metal nanoparticles on graphene.

Among other techniques, scanning tunneling microscopy, angle-resolved photoemission spectroscopy, and low-energy electron microscopy proved especially powerfull in revealing the structure, growth, and electronic properties of graphene on metals. At the time my PhD works started, few studies had exploited X-ray scattering techniques (performed with synchrotron radiation) to address the fine structure of graphene on metals. Our work widely rely on these techniques and focuses on a specific system, graphene on Ir(111), which is studied by sev-

eral ten research groups worldwide because of its high structural quality, ease of preparation, and its electronic properties, mimicking those of free-standing graphene. Besides, this system can serve as a support for highly-ordered assemblies of nanoparticles which are of interest for nanomagnetism and nanocatalysis. It was our purpose to address the structure, including deformations in three-dimensions, degree of order, and defects, of both bare graphene on Ir(111) and various kinds of nanoparticle lattices onto graphene/Ir(111), with the help of high resolution diffraction experiments performed in situ , within a ultra-high vacuum chamber where the samples can be prepared in a clean way and the temperature can be varied in a broad range.

0.2 Organisation of the manuscript

The first part of the manuscript is dedicated to an introduction and a brief review of the state-of-the-art on three topics. In the first chapter, nanoparticles on surfaces will be discussed, with a focus on the atom by atom growth on various patterned surfaces. The second chapter deals with epitaxial graphene on metals, from the different growth methods to graphene/metal interaction, and explaining the current debates about certain structural aspects. This chapter also details the system of specific interest for this thesis, graphene on Ir(111). The third chapter introduces surface X-ray diffraction, with our current system as an illustration. The experimental methods and challenges, measurements with a 2D detector and processing of the corresponding data, are also presented and discussed.

The second part of the manuscript presents our experimental results and their analysis. The fourth chapter combines and links two studies on the effects of preparation on the structure of epitaxial graphene and its tendency to commensurability. Epitaxial graphene was observed to go through transitions between several commensurate phases during growth and also as a full layer as function of temperature. The fifth chapter deals with the atomic structure of

graphene on Ir(111) measured with surface X-ray diffraction. A Fourier series model is used to model and describe this system, with a small number of parameters compared to the number of atoms in the superlattice unit cell. The last chapter presents the results of three types of nanoparticles grown on graphene on Ir(111), Pt_{40}, Pt_{20} and $Co_{20}Pt_{20}$, studied by surface X-ray diffraction. It addresses the issue of the interaction between graphene and the nanoparticles, of small-size structural effects, and of ordering of the nanoparticle lattices.

Chapter 1

Organisation of nanoparticles on surfaces

1.1 Introduction

The rapid development of research fields and applications using nanomaterials, in particular nanoparticles [Shipway *et al.* , 2000], has increased the need to produce them with high quality and in large amounts. Various methods of growth have been used to obtain nanoparticles, each of them having different yield or size distribution. Nanoparticles come in various shape and structure, such as nanocrystals, core-shells structures or coated with molecules on their surface. In addition, due to their small size they tend to aggregate in clusters, losing at the same time their specific properties. One of the possible way to circumvent this tendency and achieve high nanoparticle densities is to have nanoparticles grown on a surface with a regular spacing. Obtaining an array of nanoparticles has been one of the solution sought to uses more effectively and easily nanoparticles for various applications [Shipway *et al.* , 2000]. This is required if the particles will be used in some devices, such as sensors or electronic devices, single electron transistors or memory bits. This is also required when nanoparticles

are used as the basis for the growth of other systems, such as carbon nanotubes [Bower *et al.* , 2000] or silicon nanowires [Westwater *et al.* , 1997]. Lithography techniques will not be discussed here due to their inherent limits. This technique is well-adapted for scales around 100 nm but reaches the limits of patterning around 10-20 nm, with electron beams [Alexander Liddle *et al.* , 2011]. Below this limit, bottom-up techniques such as those that we will discuss here remain the only option. First, the shapes, some general properties and applications of metallic nanoparticles will be presented. Then we will discuss the nanoparticles grown or deposited on patterned surfaces with various approaches. Finally, we will review the specific case of using epitaxial graphene as a patterned surface inducing self-organization of nanoparticles.

1.2 General properties of nanoparticles and applications

Surfaces and thin films of materials often display specific physical properties compared to the bulk of the same material [Haruta, 1997]. Nanoparticles, which comprise a large fraction of surface atoms, also have specific properties. We will focus here on crystalline nanoparticles. Matter can crystallise at nanometric scale, usually in out-of-equilibrium forms, *e.g.* cubes, pyramids, small rods [Xia *et al.* , 2009].. Their final shape depends on a large number of parameters, influencing thermodynamics (*e.g.* surface energies, temperature), kinetics (*e.g.* deposition rate or concentration in solution, temperature), or both. Moreover, their properties change depending on their shape, size or local environment. For example, optical properties can be affected by their shape and ordering, changing their response upon excitation [Ye *et al.* , 2010, Henzie *et al.* , 2013] and catalytic properties can be tuned depending on support and temperature [Haruta, 1997].

Nanoparticles are already used in various applicative domains, such as medical imaging and treatment with gold nanoparticles. For example, cancerous cells

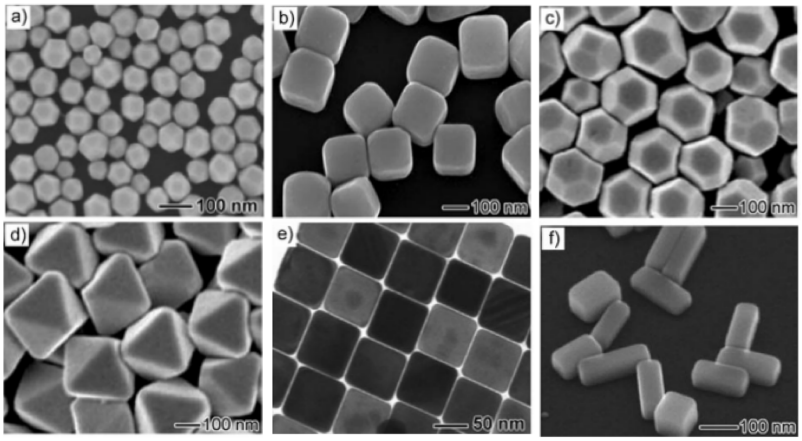

Figure 1.1: From Ref. [Xia *et al.* , 2009], SEM pictures of Ag nanoparticles of different shapes prepared in organic liquid solutions, (a) cuboctahedrons, (b) and (e) cubes, (c) truncated octahedrons, (d) octahedrons and (f) nanobars.

can be specifically targeted by coating nanoparticles with organic molecules designed to attach to the deficient cells [Huang *et al.* , 2006]. This proves useful to image precisely affected areas and then possibly destroy only the cancerous cells by specific excitation of the particles. Metal nanoparticles are also widely used for their enhanced catalytic properties. Industry pushes the development of ever more efficient catalytists, *i.e.* based on smaller and smaller nanoparticles. Platinum nanoparticles for instance make it possible to strongly reduce the amount of expensive material, compared to bulk systems, without loss of catalytic activity, as shown for instance for the oxygen reduction reaction [Nesselberger *et al.* , 2013]. Another example is bimetallic particules with platinum that have been investigated to remove the carbon monoxide pollution in fuel cells [Bonnemann *et al.* , 2000].

Furthermore, some nanoparticles have shown to have magnetic properties that could be used for various applications, especially when ferromagnetism can be stabilized at the scale of individual nanoparticles, rather than global paramagnetism [Woods *et al.* , 2001] or more complex states such as spin glasses [Jonsson, 2004]. One of the possible application of magnetic nanoparticles is data storage in ultra-high density devices, typically beyond the 25 nm pitch of

nowadays hard drives [Ahniyaz *et al.* , 2007].

For all these applications, the achievement of nanoparticles assemblies with narrow size distributions, in some case assembled in ordered assemblies, is highly desirable.

1.3 Nanoparticles on surfaces

Several methods can be used to obtain nanoparticles arrays on surfaces, relying on either on-surface growth or on on-surface deposition of pre-formed nanoparticles. One of the first method to obtain ordered arrays of nanoparticles has been to grow them on a patterned surface, as it was for instance extensively shown in the case of cobalt or iron nanoparticles onto the Au(111), which naturally exhibits a nanometer-scale pattern, its so-called herringbone reconstruction [Voigtländer *et al.* , 1991a, Voigtländer *et al.* , 1991b].

1.3.1 Deposition of preformed nanoparticles on surfaces

As we have discussed in a previous paragraph, the growth in a liquid phase is used widely but nanoparticles cannot be self-organised on a large scale in this environment. However, it has been observed in several studies that after deposition on surfaces and drying of the solvent, nanoparticles self-organise on the surface, with symmetries depending on their shapes. For example in Ref. [Burnside *et al.* , 1998], cubic nanoparticles have been observed to have various degrees of organisation depending on the temperature applied to dry the solvent. Lower temperatures lead to a slower drying, allowing a better arrangement of the particules with attractive-repulsive interactions due to the surfactant. It can be noted that too high temperatures results in the coalescence of the nanoparticles into a thin polycrystalline film, due to the decomposition of the organic shells of the nanoparticles. The organisation on amorphous carbon surface of oxide nanoparticles using a slow drying method has also been performed, showing hexagonal or cubic organisation depending on their shapes [Sun *et al.* , 2004].

A similar method has been used with gold nanoparticles with a organic shell deposited on silicon [Liu *et al.* , 2002]. The surface was functionnalized beforehand to enhance the adhesion and thus the nanoparticles are well dispersed on the surface after drying but with no organisation. A drop of a second solvent after that step results in the organisation of the nanoparticles in small domains, rotated relative to each others and with lots of vacancies between them.

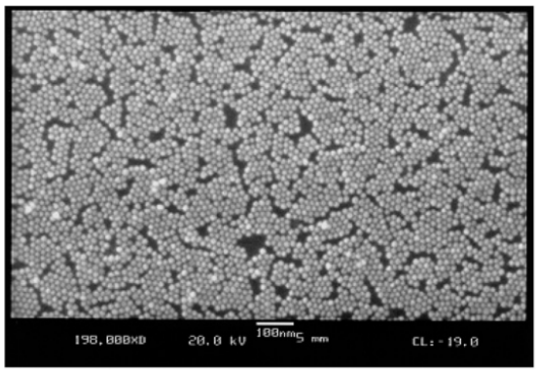

Figure 1.2: From Ref. [Liu *et al.* , 2002], SEM pictures of Au nanoparticles deposited on silicon and organised after the drying of their solvent.

Another method for preformed nanoparticles deposition on surfaces without a liquid phase is to use gases as a medium. For example, laser vaporization–gas condensation sources [Milani *et al.* , 1990, Bardotti *et al.* , 2011a] can be used, as shown in Fig.1.3. The source of the nanoparticles is a metallic bar in a vacuum chamber hit by a laser, forming briefly a plasma. Using in a pressure gradient (mbar range), a continuous flow of a neutral gaz in the chamber induces the growth of the nanoparticles. Various parameters can be tuned to change the particles size and size-distribution, such as the gas pressure or a quadrupole as a mass-selection deviator.

This setup allows both a broad range of materials to be used as a source, including bimetallic samples, and various diameters in the nanometers range, down below 2 nm [Alayan *et al.* , 2004], around a hundred atoms. In addition, the spread of the nanoparticles diameters is of $\pm 8\%$, showing a well defined size distribution [Bardotti *et al.* , 2011b]. Moreover, the flow of incoming is low

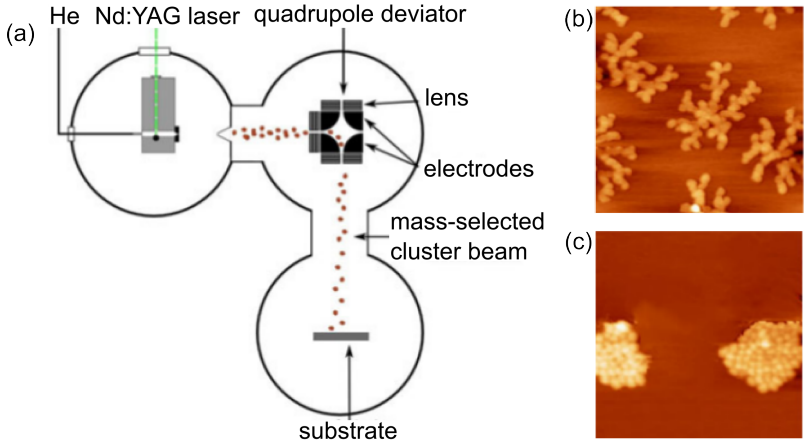

Figure 1.3: From Ref. [Bardotti *et al.* , 2011b], (a) sketch of the laser vaporization-gas condensation source, showing the several steps of preformed nanoparticles deposition. (b) and (c) STM images of 2.2 nm diameter nanoparticles, respectively gold and platinum, deposited on graphite.

enough so that nanoparticles only form two dimensional film and not three dimensional clusters, as shown in Fig. 1.3 with deposition on graphite. However, depending on the nature of the nanoparticles and their size, aggregations can result in coalescence of the nanoparticles. To prevent this, patterned surfaces can be used. Nanoparticles then stay in a determined site, thus are not prone to coalescence. Self-organized nanoparticles can be formed accordingly, for instance on pre-patterned graphite surfaces [Bardotti *et al.* , 2002, Hannour *et al.* , 2005].

1.3.2 Growth of nanoparticles on surfaces

Surfaces reconstructions have provided natural templates to grow arrays of nanoparticles atom-by-atom [Ibach, 1997, Shchukin & Bimberg, 1999, Rousset *et al.* , 2002]. The preparation of nanoparticles with this method requires ultra-clean environments such as available under ultra-high vacuum. Indeed, most metallic nanoparticles oxidise instantly if exposed to the atmosphere or will adsorb molecules on their surface.

For example, the Au(111) surface herringbone reconstruction presents preferential adsorption sites. The nucleation of the cobalt nanoparticles occurs at

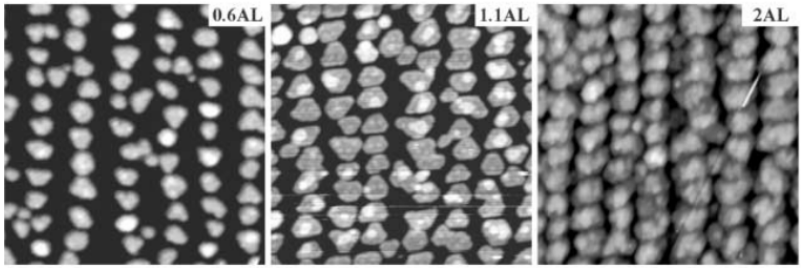

Figure 1.4: From Ref. [Fruchart *et al.* , 2003], STM pictures of self-organised Co nanoparticles grown on Au(111), with several coverages (0.6, 1.1 and 2 monolayers).

the bend part in the rectangular superlattice, which comprises two nucleation sites. The symmetry of the superlattice defines two characteristic distances between nucleation sites, a small periodicity, 7.7 nm, between two elbow along the stacking direction of the herringbone and a large one between the rows, 17 nm. Coalescence between nanoparticles sets in from one monolayer of Co deposited, and becomes prominent from the second Co monolayer [Fruchart *et al.* , 2003]. However, grazing incidence x-ray scattering experiments showed that despite coalescence, a periodic microstructure that is due to strains at the interface remains. Moreover, three rotational variants can be present with the herringbone reconstruction, with a 120° rotations between the domains, this results in domains in the hundred nanometers scale. In order to use only one variant, vicinal surfaces have been used [Rousset *et al.* , 2002].

Other gold surfaces have been used to grow nanoparticles, such as Au(788) [Repain *et al.* , 2002, Weiss *et al.* , 2005]. This surface is made of (111) terraces and shows a $(\sqrt{3} \times 22)$ reconstruction with domain walls perpendicular to the steps. The intersection of these two is the site of nucleation of the cobalt nanoparticles as shown in Fig. 1.5. However, coalescence starts at a lower coverage than on Au(111) surfaces, at 0.75 monolayer, preventing a narrow size distribution. In addition, temperature is an important factor to obtain organisation in such samples [Repain *et al.* , 2002]. It was shown that deposition at low temperature, 130 K, improved organization and that higher temperature,

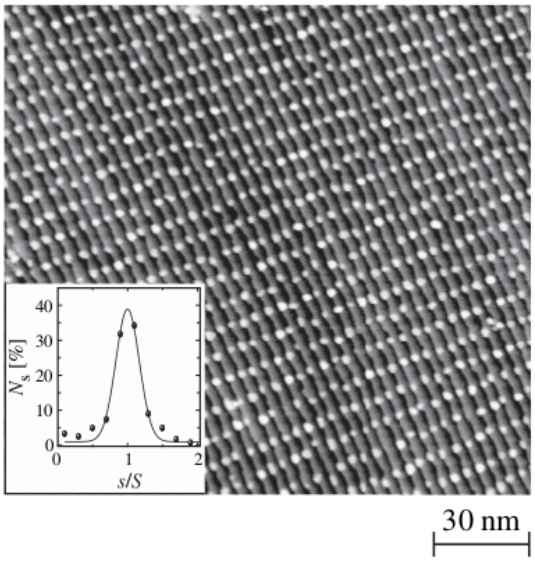

Figure 1.5: From Ref. [Weiss *et al.* , 2005], STM picture after annealing of Co deposited on Au(788), with a coverage of 0.2 monolayer. The inset show the size distribution normalized with the mean size of the islands.

480 K, resulted in a random growth and in a capping of the particles by a gold monolayer. The intermixing of the substrate with the nanoparticles can change their properties, in particular the magnetization, thus it should be prevented.

Another example is the FeO/Pt(111) surface. There is a mismatch of approximately 10 %, resulting in a moiré structure with a 2.6 nm periodicity that can be observed in STM or diffraction. Various metals can be deposited to form nanoparticles on this template, such as gold [Lemire *et al.* , 2004] or paladium [Shaikhutdinov *et al.* , 2003]. The smaller periodicity of the superlattice leads to smaller nanoparticles and its triangular symmetry to an isotropic 2D distribution in contrasts to the Au(111). In the case of gold nanoparticles, the atomic deposition is done at low temperature (120 K) and is observed to decorate substrate steps as well as the terraces. However, after annealing, small particles of one to three atomic layers form due to a stronger interaction between gold atoms than with the oxide, unlike paladium that can form large monolayers [Shaikhutdinov *et al.* , 2003]. These nanoparticles can be used for CO catalysis for example [Lemire *et al.* , 2004].

These questions highlight the issues of nanoparticles interacting with their substrate, *via* defects for example, that can hinder the growth of well ordered arrays. Graphene is known to be impermeable, if defect-free, and therefore is of high interest to prevent such effects. Furthermore, epitaxial graphene, with the moiré superlattice, has proven to be a template to grow arrays of monodisperse self-organised nanoparticles. *h*-BN on metals is a similar system of great interest that also presents a superlattice but due to a high atomic diffusion on its surface has not proven as useful as epitaxial graphene [Yazyev & Pasquarello, 2010].

1.3.3 Nanoparticles on epitaxial graphene

With the rise of 2D materials and epitaxial graphene especially, a new kind of surface has emerged to grow or deposit nanoparticles. As we will discuss in details in the next chapter, it is possible to grow large area of high quality graphene, without rotational variants, on transition metal substrates in UHV conditions. The graphene on metal forms a structure similar to a surface reconstruction, a superlattice which may be described with the analogy of the moiré effect, due to the mismatch between the two lattice parameters. Potentially large array of self-organised nanoparticles of controlled size can be grown on such a patterned surface. Hybrid systems of graphene/nanoparticles have been studied that could have applications as catalysts in fuel cells [Xu *et al.* , 2008]. On epitaxial graphene, carbon monoxide has been observed to adsorb on platinum nanoparticles on top for example [Gerber *et al.* , 2013]. It can be noted that other 2D materials have been observed to grow nanoparticles epitaxially, like MoS_2 with various metals nanoparticles [Huang *et al.* , 2013], however in this case the nanoparticles are grown in a liquid phase.

It was first reported that iridium nanoparticles could be grown and self-organised on the moiré pattern of epitaxial graphene grown on Ir(111) [N'Diaye *et al.* , 2006] as shown in Fig. 1.6. The growth can be described step by step : first deposited adatoms diffuse on the surface and have a higher probability to adsorb on the hcp-site of the moiré cell. As more adatoms are deposited, they can form stable

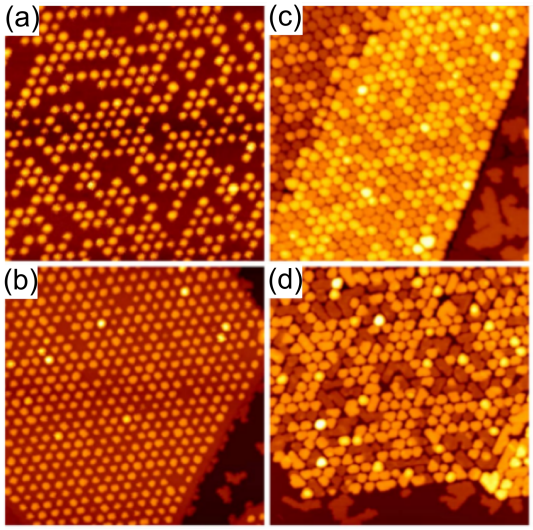

Figure 1.6: From Ref. [N'Diaye *et al.* , 2006], STM pictures of iridium nanoparticles grown on graphene on Ir(111) organised on the moiré superlattice; with (a) 0.03, (b) 0.10, (c) 1.5 and (d) 2 monolayers amount deposited.

di- and trimers that will form the seed of the nanoparticles. This nucleation phase ends as most of the hcp sites are seeded by a few atoms. Then, as deposition continues, the nanoparticles keep growing and have a second atomic layer when around 25 atoms per site are deposited. The number of layers per particles can be up to five or six, as shown in Fig. 1.7 but there will be coalescence of some of the particles before that [N'Diaye *et al.* , 2009]. Coalescence begins to occur around 1.5 monolayer of iridium deposited.

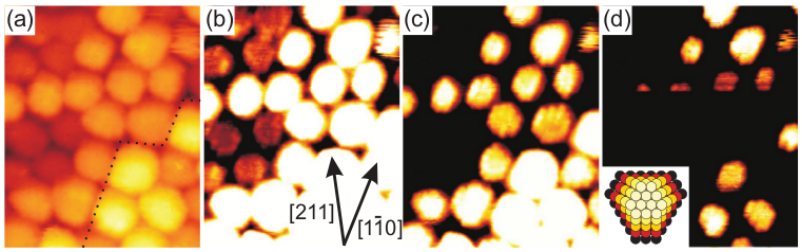

Figure 1.7: From Ref. [N'Diaye *et al.* , 2009], STM pictures of Ir nanoparticles grown on graphene on Ir(111), (a) is a topograph of the studied area. (b), (c) and (d) show the same area with various contrasts to highlight the structure of the nanoparticles atomic layers (with the corresponding structure sketched in the inset of (d)).

Graphene on Ir(111) can be used to grow other metallic and bimetallic nanoparticles on the same principle [N'Diaye *et al.* , 2009]. The nature of the element deposited influences strongly the nucleation and the organisation of the particules. Platinum and tungsten behave mostly similar to iridium, yielding areas of a few tens of nanometers of organised nanoparticles of the same size. However, metals like gold and iron alone do not show self-organisation behaviour in the explored deposition temperature range (100-300 K). They form large clusters that span over few moiré cells and are randomly dispersed on the surface. Rhenium deposition is an intermediate case : with small amount deposited, it is possible to partially obtain monodisperse nanoparticles of the same size on the moiré lattice. At higher coverages, the energy barrier for adatom diffusion between the different moiré sites is too low to prevent the atoms to move from one moiré cell to another. A possibility to avoid coalescence and mobility of atoms between cells to keep a monodisperse array is to seed the moiré sites with a few atoms of a metal that self-organise, like Ir or Pt, and then deposit the other, in this case Au or Fe. In the case of Fe, with a seeding deposition of 0.1 monolayer of Ir, it is possible to keep monodisperse nanoparticles of the same size up to a deposition of iron of 2 monolayers.

These various behaviours raise the question of the interaction of the nanoparticles with the graphene : is it physisorption, or rather chemisorption ? DFT calculations on single layer Ir particles on graphene on Ir(111) predicted that there is a rehybridization of the carbon atoms below to sp^3, which points to chemisorption [Feibelman, 2008]. Measurements of the distance between graphene and iridium nanoparticles seems to support this scenario [Franz *et al.* , 2013]. A reasonable assumption, based on the observed absence of organisation with Au or Fe for instance, is that not all types of atoms allow for local chemisorption between graphene/Ir(111) and the nanoparticle, though.

Graphene on Ir(111) is not the only epitaxial graphene used as a template to grow nanoparticles. Graphene on Ru(0001) is also used in several studies, as it presents a moiré lattice slightly larger than graphene on Ir(111), providing

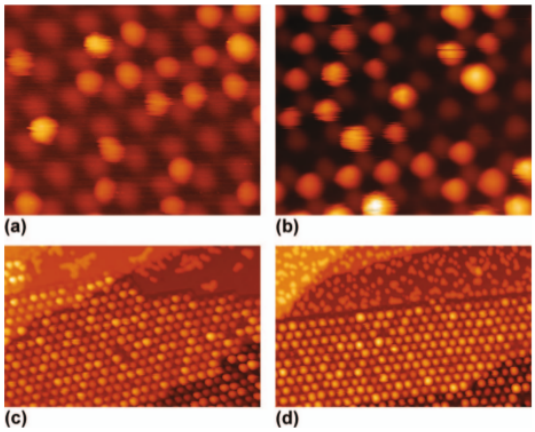

Figure 1.8: From Ref. [Donner & Jakob, 2009], STM pictures of platinum nanoparticles grown at low temperature (145-180 K) on graphene flakes on Ru(0001) with several coverages, (a) 0.06, (b) 0.12, (c) 0.18 and (d) O.24 monolayer. Platinum on bare Ru(0001) can be observed on the upper part of (c) and (d), showing no organisation there.

larger spacing between the nanoparticles and thus highlighting the potential of epitaxial graphene to create various arrays depending on the moiré. Platinum nanoparticles have been the focus of most studies [Donner & Jakob, 2009, Pan *et al.* , 2009, Zhang *et al.* , 2009] and like on graphene on Ir(111) it self-organises on a specific site of the moiré as shown in Fig. 1.8. Moreover in this case, the coalescence occurrs less than on graphene on Ir(111), as the nanoparticles more readily grow in the direction perpendicular to the surface. This is explained by a larger energy barrier for adatom diffusion between moiré sites in this system, that might be linked to the strongest variation of the graphene-substrate interaction in case of a Ru(0001) substrate [Pan *et al.* , 2009]. In another study [Liao *et al.* , 2011], cobalt was deposited on graphene on Ru(0001) and similarly to iron and gold graphene on Ir(111), no self-organization could be observed, as shown in Fig. 1.9. The atoms deposited are not trapped in a specific site on the surface and thus form clusters with a large size distribution, even exceeding the size of a moiré lattice with higher coverages. It can be noted that they are stable up to 500-650 K, from which clusters partially coalesce and get intercalated between graphene and Ru(0001).

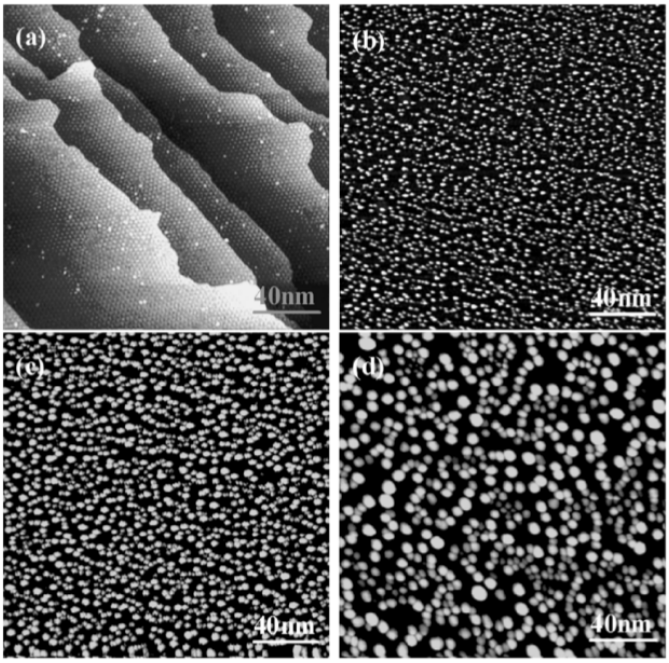

Figure 1.9: From Ref. [Liao *et al.* , 2011], STM pictures of Co deposited on graphene on Ru(0001) with several coverage, (a) 0.01 monolayer, (b) 0.13 monolayer, (c) 0.7 monolayer and (d) 2.5 monolayers.

1.4 Conclusion

Arrays of monodisperse nanoparticles will be used more and more in various applications, and one way to optimize their use is to prepare them by bottom-up techniques, for instance onto patterned surfaces yielding highly ordered and narrow size distribution assemblies. A promising such surface is that of graphene grown onto metal surfaces, which forms moiré-like patterns. As graphene can be grown on various metallic substrates, patterns with various pitch and symmetries can be achieved. Systems could be designed to exploit, besides the natural self-organization onto such surfaces, the unique properties of graphene, for instance in view of optics or electronics. Precise understanding of the growth and structure of nanoparticle assemblies onto graphene calls for high resolution investigation of the structure (order, coincidence sites, strains) of graphene and of the moiré-like pattern as a function of preparation conditions.

Chapter 2

Epitaxial graphene on metals

2.1 Introduction

Epitaxial growth is a process that has been used for years to elaborate and engineer thin films or heterostructures of metals or semiconductors. Perfect epitaxy occurs when all the atomic rows continue from one material to the other without any defect, with, in some cases, the atoms at the interface making covalent bonds. However, since most materials do not have the same lattice parameter or the same crystalline symmetry, the most common occurances to reach the highest density of atomic coincidence at the interface is by having rotations, strain and deformation in the interface atomic layers, dislocations or a combination of all. However, this is different in the case of graphene grown on a substrate, as it is an hybrid interface with a large mismatch. In fact, epitaxial graphene is part of another class of epitaxy, the van der Waals epitaxy, and thus similar to other systems with a large mismatch of periodicity [Koma, 1992].

Epitaxial graphene defines a broad range of systems. We will focus here on the various growth processes on the clean surface of a metallic substrate in ultra

high vacuum (UHV). The epitaxial relation with the substrate can lead to strain, various rotational domains or different interactions. Epitaxial growth on other substrates has been achieved, such as silicon carbide [Forbeaux *et al.* , 1998, Charrier *et al.* , 2002], Ge(110) and Ge(111) [Lee *et al.* , 2014] or sapphire [Fanton *et al.* , 2011, Song *et al.* , 2012, Saito & Ogino, 2014], but these systems will not be addressed here. Several reviews have already been written on the subject over the years [Wintterlin & Bocquet, 2009, Batzill, 2012, Tetlow *et al.* , 2014], as this research domain is still growing and the systems, their structures, interactions are still under close investigation. Moreover, one of the main attractiveness is to understand these systems under highly controlled conditions, thus helping to grasp the various problems arising in producing large area of high quality graphene for various applications, like in industry for new electronic devices.

This Chapter deals with epitaxial graphene on metallic substrates. Firstly, the various growth processes will be presented, with examples on several substrates. In a second part, the issues and variations arising from the nature of the substrate will be discussed. Then, we will focus on the specific system of epitaxial graphene on Ir(111). Finally, we will expose how this specific system is used as a basis for more complex processes, such as intercalation of various materials between the substrate and graphene.

2.2 Growth on metals

Generally, the growth of epitaxial graphene can be described in a few simple steps. On a clean metallic surface at high temperature in a vacuum environment, carbon is supplied and diffuses on it. Nuclei will then form preferably at defects sites such as atomic steps and will grow into graphene islands. The growth will continue until the carbon supply is stopped or a full graphene layer is achieved depending on the substrate. The possibility of multilayer graphene is also function of the substrate as we will see. The structure and quality (defects, domains...) of the resulting graphene depend heavily on the growth parameters,

such as the temperature and precursor gas pressure.

Epitaxial graphene on metal has been studied in detail since it is the easiest way to achieve high-quality graphene on large area, systems and growth methods transposable in industry in recent years. Although the number of studies on these systems has grown exponentially over the last decade, the existence and observation of epitaxial graphene has been known and achieved since the 70s. It was then dubbed monolayer graphite and observed on Ni(111) [Shelton *et al.* , 1974] and Ni(100) [Isett & Blakely, 1976] with LEED and Auger electron spectroscopy, with a segregation growth process at high temperature. This was also achieved on Ir(111) with the decomposition of carbonaceous gas at high temperature [Nieuwenhuys *et al.* , 1976]. These are the two main methods to grow epitaxial graphene that are still used nowadays.

The nature of the substrate defines which growth method can be usually used. Generally, the carbon feed-stock is brought as a carbonaceous gas on the substrate. The solubility of carbon in the metallic substrate [Arnoult & McLellan, 1972] is crucial and is function of the temperature, as it will determine the growth process, either segregation growth or a growth process confined at the surface with the carbon atoms unable to dissolved into the substrate. For example, at 1200°C, the maximum solubility of carbon in ruthenium is around one carbon atom for 10 ruthenium ones and for iridium it is one for sixty. The segregation method can be done for most substrates but for some will need really high temperature, difficult to achieve in most setups, thus making the CVD growth simpler for substrates like iridium silver. However, the CVD growth process can be difficult if the carbon on the surface dissolves in the bulk instead of fuelling the growth process.

2.2.1 Segregation

The segregation of carbon species to metallic surfaces has been known and studied for a long time. In metallurgy, the formation of carbides or graphitic layers was considered as surface that was detrimental, *e.g.*, in the view of

catalysis applications. The segregation growth method has been observed on various substrates such as nickel [Shelton *et al.* , 1974, Isett & Blakely, 1976, Zhang *et al.* , 2010], ruthenium [Marchini *et al.* , 2007, Sutter *et al.* , 2008], iron [Vinogradov *et al.* , 2012], rhenium [Tonnoir *et al.* , 2013] and even iridium [Loginova *et al.* , 2009b] among others. We will take the first two systems as examples in this section. On these metals at high temperatures, in UHV, the carbon atoms are located inside the substrate bulk than on the surface due to the carbon solubility. However, as the solubility varies strongly with the temperature [Arnoult & McLellan, 1972], the cooling rate plays a major role, a slow cooling allows carbon atoms to exit the substrate, as it becomes energetically more stable for them to be on the surface, instead of quenching them inside the bulk with a fast cooling rate. It is possible to grow mono-, multi-layer graphene or a carbide [Yu *et al.* , 2008, Dong *et al.* , 2012].

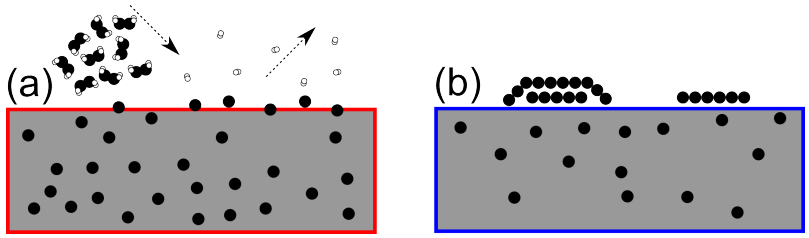

Figure 2.1: (a) Sketch of the first step of the segregation growth, at high temperature. The carbon source can be either the carbon already in the bulk of the substrate or can be added using carbonaceous gases. (b) Cooling the substrate leads to the segregation of the carbon on the surface, forming graphene flakes, monolayer or more.

There are two possibilities as a source of carbon atoms in this cases. Firstly, one can use an external source, such as hydrocarbon gases [Sutter *et al.* , 2008, Zhang *et al.* , 2010], to add carbon atoms in the substrate. Secondly, the carbon atoms already dissolved in the bulk can be also used for the growth [Shelton *et al.* , 1974, Marchini *et al.* , 2007]. In either case, the growth proceeds in two steps, as shown in Fig. 2.2.1, by first annealing the sample at high temperature to achieve the high carbon solubility and mobility inside the substrate, thus bringing atoms from the bulk towards the surface if it was previously depleted. Cooling it over

a few hundred degrees then decreases the carbon solubility, precipitating carbon on top of the substrate surface.

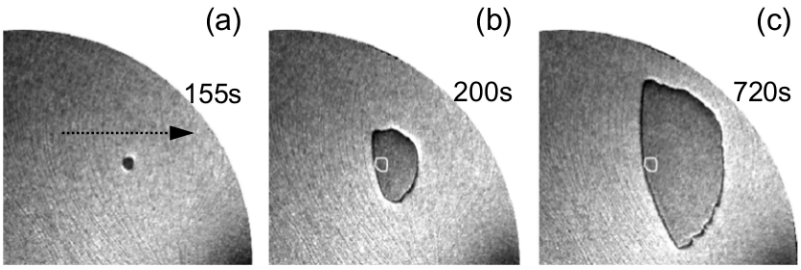

Figure 2.2: (a), (b) and (c) LEEM images from Ref. [Loginova *et al.* , 2009a], showing the growth of a graphene island on Ru(0001) over time down the atomic steps of the substrate.

The nucleation of graphene islands happens preferentially at defects zones such as step edges and grow from there. This has been observed in real-time with low-energy electron microscopy (LEEM) on Ru(0001) [Sutter *et al.* , 2008], showing the islands at the atomic steps of the substrate expand along and below it but not above. This is caused by the graphene edge bonding with the substrate step, preventing carbon adatoms to attach themselves there and thus explaining the growth above the step. The growth behaviour on Ru(0001) has been described by McCarty *et al*. [McCarty *et al.* , 2009] as carbon adatoms diffuses on the substrate surface around the graphene islands and attaching themselves on the sides instead of directly attaching themselves on the graphene from the bulk substrate. This adatom mobility on the surface is similar to the others processes with no carbon dissolution in the substrate. Finally, it is possible to grow bilayer graphene on Ru(0001) with this method [Sutter *et al.* , 2008, Sutter *et al.* , 2009].

With nickel, a low density of nucleation sites on single crystals Ni(111) can be achieved with a slow cooling rate, thus allowing the formation of large domains [Odahara *et al.* , 2011]. Bi- and tri-layers have been observed on Ni(111) [Zhang *et al.* , 2010, Odahara *et al.* , 2011], this is a step by step process however, first growing one full monolayer, then cooling it to grow a second layer

below the first one and then the third one below the second before its completion. This happens also at the grain boundaries of nickel polycrystalline films for example [Zhang *et al.* , 2010], where the nucleation occurs as carbon accumulate more easily during the segregation. It is possible to grow even more layers, more than 10, thus obtaining a thin graphite layer that is slightly thicker than multilayer graphene [Kim *et al.* , 2009].

2.2.2 Chemical vapour deposition and temperature programmed growth

Growing graphene in a large quantity for use in industry is already a reality [Bae *et al.* , 2010]. The process used is the chemical vapour deposition (CVD) on copper foils, using the catalytic properties of copper. This process is part of a larger family of growth on various substrates that differs slightly from the previously discussed method, segregation. Overall, a graphene growth confined on the surface, thus without carbon dissolution into the bulk, is always possible as long as the metal does not form a carbide. To achieve this confined growth, several ways are possible, either by adsorbing carbonaceous gases on the substrate surface and then heating it to decompose it or directly by exposing the hot surface of the substrate to the gases. These two methods are called temperature programmed growth (TPG) and CVD. The temperature ranges where this can be achieved are dependent on the nature of the substrate, the higher limit set by the solubility of the carbon [Arnoult & McLellan, 1972], the lower set by the mobility of the carbon adatoms and the possible carbide formation. This can be used on various metallic substrates, single or polycrystals, such as Pt(111) between 500 and 1000°C [Land *et al.* , 1992], Rh(111) between 500 and 800°C [Dong *et al.* , 2012] or Ir(111) between 600 and 1200°C [Coraux *et al.* , 2009] among others.

On most substrates, the growth process is usually done in UHV conditions on single crystals at high temperature as previously mentioned, but can also be done at ambient pressure (AP-CVD) [Gao *et al.* , 2012] and at low tempera-

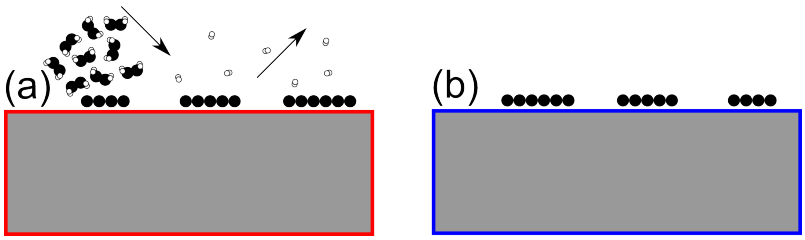

Figure 2.3: (a) Sketch of the first step of the CVD process, the substrate is at high temperature and the carbonaceous gas decomposed on the surface, leaving carbon adatoms and graphene flakes growing. (b) At the end of the CVD, the sample is cooled down to room temperature with the graphene flakes on top.

ture, as low as 300°C [Li *et al.* , 2011b]. The sample surfaces are prepared and cleaned beforehand by cycling ion bombardment, annealing at high temperature to reconstruct the surface and annealing under oxygen to remove any trace of carbon on the surface, leaving a clean surface with well defined atomic steps to grow the graphene. The sample is first brought to high temperature, then the carbon source can be introduced in the chamber, it can be simple gases such as methane [Li *et al.* , 2009] or ethylene [Coraux *et al.* , 2008] or more complex molecules such as benzene [Li *et al.* , 2011b] or even C_{60} fullerenes [Otero *et al.* , 2010], showing a broad range of usable sources.

One of the main advantage of using a CVD process without segregation is the self-limitation of the growth to a monolayer or submonolayer on single crystal substrates. During the CVD, a modified Langmuir adsorption model is often used to describe the process [Coraux *et al.* , 2009]. Incoming gas molecules towards the surface have two possibilities, either to arrive on a bare substrate part, and therefore contact with the hot metal and decomposition occurs, or they arrive on top of an already graphene covered surface, and they do not decompose on the inert surface and desorb immediately. The molecules arriving on the hot surface sample decompose themselves into carbon adatoms or small carbon chains with mobility on the surface, the free decomposition products such as hydrogen atoms and unused molecules are evacuated by the pumps.

Like the segregation process, the nucleation happens mainly at defects, such

as atomic steps [Coraux *et al.* , 2009] but can sometimes occur in the middle of one step. Unlike on Ru(0001), the graphene flakes can grow over the step edges on some substrates, like Ir(111) during the CVD process [Coraux *et al.* , 2009]. With segregation, the density of nucleation is mostly dependant on the cooling rate applied to the substrate, where with CVD it is deeply temperature dependant. The temperature affects directly the mobility of the carbon adatoms on the surface and thus the density of nucleation. Moreover, the concentration of carbon adatoms on the surface is also an important parameter, that is mostly a function of the pressure of the gas inside the chamber. A rapid coalescence, and thus a large number of small graphene islands, is caused by low temperature or a high concentration of carbon adatoms, as they cannot have a high mobility. On the contrary, with higher temperature or low concentration of adatoms, their mobility increases, resulting in a low nucleation density and larger graphene islands. A broad range of sizes can thus be achieved, from nanometric islands [Coraux *et al.* , 2009] to few hundred microns single crystals [Li *et al.* , 2011a]. This highlights the strength of the growth method for a vast range of applications, as small islands could be used as quantum dots and large nearly millemetric size graphene single crystal of high quality is providing a substitute to exfoliating graphite.

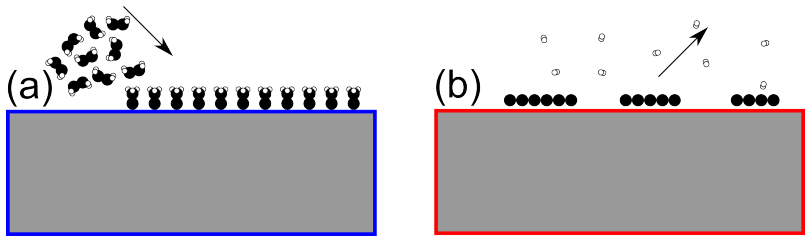

Figure 2.4: (a) Sketch of the adsorption of ethylene molecules on the substrate surface at room temperature, decomposing partially into ethylidine. (b) Flash at thigh temperature, resulting in cracking the molecules, free hydrogens and the growth of graphene flakes on the surface.

The control of all the growth parameters can be difficult, in particular the concentration of carbon adatoms. TPG allows to control artificially this param-

eter, by having a high concentration. It emanates from the catalytic power of the metallic substrate even at room temperature. This has been observed on different substrates such as Ni(111) and Pt(111) [Felter & Weinberg, 1981] or Ir(111) [Marinova & Kostov, 1987]. At room temperature, ethylene for example will be adsorbed on the metal surface, where it will partially dehydrogenate to form ethylidine, loosing one hydrogen atom, breaking the double bond and having the three remaining hydrogen atoms on the top carbon. Using this property of the metallic surface is the first step of the TPG, as the single crystal surface is exposed to ethylene in UHV condition, covering it completely with adsorbed molecules. The next step is a flash at high temperature for a few seconds, typically between 600 and 1200°C for Ir(111) [Coraux *et al.* , 2008], thus continuing the dehydrogenation of the molecules on the surface to obtain a high concentration of carbon adatoms. The density and size of the resulting graphene flakes depends strongly on the annealing temperature. Below 950°C, it forms small graphene island scattered over the atomic terraces of the substrate. Over 1050°C, the islands are larger, over 100 nm, and are mostly located at the atomic steps of the substrate but there are always a few that remain away from the step, in the middle of the terraces. This highlights again the effect of temperature on the mobility of the adatoms. At lower temperature the carbon atoms cannot move over a large distance, thus clustering in small flakes or even amorphous clusters. Meanwhile, at higher temperature, the mobility increases allowing the growth of fewer, larger graphene flakes nucleating mostly on the lower part of an atomic step. This results in a partial coverage of the substrate surface, $22 \pm 2\%$, with graphene islands having the same orientation with the substrate. In addition, this process can be used to bypass the dissolution of carbon atoms in the bulk with metals having a high solubility such as Rh(111) [Dong *et al.* , 2012].

The two processes, CVD and TPG, can be combined to obtain a full coverage of graphene [van Gastel *et al.* , 2009]. This takes advantage of the few nucleation sites and highly orientated resulting graphene flakes of the TPG at

high temperature to continue their growth with a CVD process, thus achieving fewer large graphene domains with a lower orientation dispersion than with CVD growth. This lower misorientation of the domains with the substrate and the structural issues generally will be discussed in a later paragraph of this chapter.

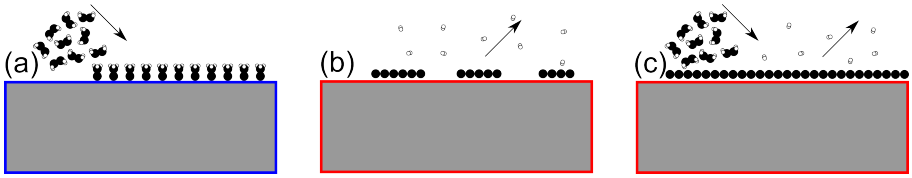

Figure 2.5: (a) and (b) are the same two TPG steps described in Fig. 2.4. (c) Completion of the graphene layer with CVD, ethylene is brought into the chamber and reacts on the substrate surface.

To conclude this part about the various growth processes, one can see the emergence of a few main issues. First, the nature of the substrate influences decisively which growth process will be used, despite not totally restricting it. The carbon source is not as crucial, simple molecules such as methane and ethylene are used for convenience with the various set-ups and pressure conditions. The growth temperature has however a large effect on the resulting graphene, either because of the carbon solubility, dehydrogenation reactions or carbon adatoms mobility, thus affecting the size of the graphene islands or a growth resulting in a carbide or amorphous carbon instead of graphene. We will see in the next paragraph and in chapter 4 that the growth temperature has also an effect on the graphene itself.

2.3 Structure and interaction of graphene with its substrate

The structure of epitaxial graphene depends on several parameters, such as growth conditions and the type of substrate. Thus graphene can be strained, compared to theoretically isolated graphene, or the graphene/substrate interac-

tion varies depending on the nature of the latter. These changes from the ideal flat sheet of graphene modify the graphene properties in various ways, opening a vast field of possibilities to tailor them for various uses or requirements. Moreover, the structure can differ if there are rotational domains, and depends on the mismatch with the substrate surface.

2.3.1 Epitaxial relationship

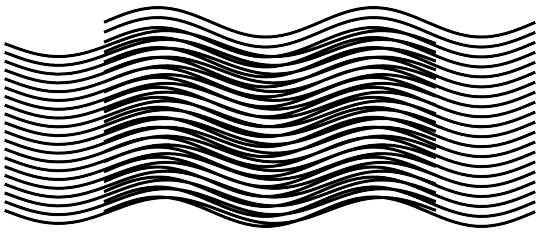

Figure 2.6: Sketch of a moiré effect with two superimposed periodicities.

Epitaxial graphene and its substrate surface have typically a lattice parameter mismatch around 10% on most metals, 2.46 Å for isolated graphene [Zakharchenko *et al.* , 2009] compared to a range of lattices parameters from 2.49 Å for Ni(111) up to 2.88 Å for Au(111). This mismatch leads to the observation of a superlattice effect with various techniques, STM or diffraction among others. This effect has been compared to the moiré optical effect, like the optical beat of two superimposed grids or veils, like the sketch in Fig. 2.6. It is referred in epitaxial systems as moiré superstructure [Ritter *et al.* , 1998]. The lattice parameter of the moiré $\frac{1}{a_{moiré}}$ is defined as

$$\frac{1}{a_{moiré}} = \frac{1}{a_{Gr}} - \frac{1}{a_{substrate}} \tag{2.1}$$

with a_{Gr} the lattice parameter of the graphene and $a_{substrate}$ the lattice parameter of the substrate surface. With a mismatch around 10%, $a_{moiré}$ is of the order of a few nanometers, 2.53 nm on Ir(111)[N'Diaye *et al.* , 2006] or 2.2 nm on Pt(111) [Land *et al.* , 1992].

This mismatch and analogous moiré effect leads to the issue of commensurability of the epitaxial graphene with the substrate. Such systems are commensurate when an integer lattice units of graphene matches another number of surface units in two dimensions, thus allowing rotations, that can be defined as $(n \times m)_{Gr}$ matching $(p \times q)_{surface}$. Nonetheless, not all systems are commensurate and incommensurate ones have been observed and studied [Zi-Pu *et al.* , 1987, Blanc *et al.* , 2012] and this issue will be discussed further in a latter paragraph in this chapter on graphene on Ir(111). Local probe techniques such as STM or AFM often do not have at the same time the field of view and the precision to assess such problems on a large scale, while diffraction techniques are more adapted to study incommensurability. Various moiré have been reported and debated on several substrates.

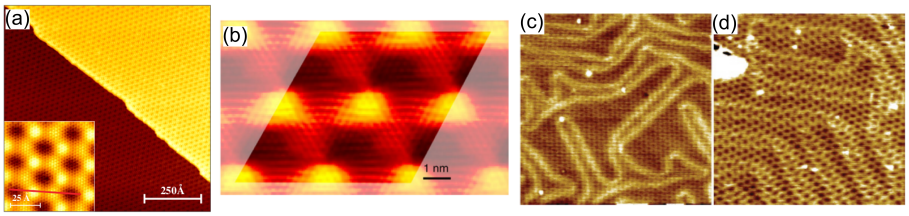

Figure 2.7: (a) STM topograph of the moiré of graphene on Ir(111) on two atomic steps from Ref. [N'Diaye *et al.* , 2008] (b) STM topograph of the moiré of graphene on Ru(0001), with the supercell highlighted from Ref. [Martoccia *et al.* , 2008] (c) and (d) STM topographs of the moiré of graphene on Au(111), showing reconstruction due to the herringbone variation from Ref. [Nie *et al.* , 2012]

For example, graphene on Ru(0001) was first reported with a moiré of $(12\times12)_{Gr}$ matching $(11\times11)_{Ru}$ [Marchini *et al.* , 2007] or $(11\times11)_{Gr}$ matching $(10\times10)_{Ru}$ [Vazquez de Parga *et al.* , 2008], but later reported to be $(25\times25)_{Gr}$ matching $(23\times23)_{Ru}$ with high resolution x-ray diffraction [Martoccia *et al.* , 2008]. However, it can be pointed out that it is possible that all these different structures coexist. The samples in these three studies were prepared differently, with segregation or TPG at 1000 K [Vazquez de Parga *et al.* , 2008], segregation at 1400 K [Marchini *et al.* , 2007] or CVD at 1115 K followed by segre-

gation at a slow cooling rate [Martoccia *et al.* , 2008]. This broad range of temperatures used during the various growth processed should have an effect on the resulting graphene, as the graphene and the metallic substrate do not have the same thermal expansion coefficient (TEC), this is illustrated in Fig. 2.8. Isolated graphene over this temperature range is predicted to have a small TEC [Mounet & Marzari, 2005, Zakharchenko *et al.* , 2009], unlike the ruthenium [Hall & Crangle, 1957]. Thus, one could expect a variation of the possible coincidence effect depending on the temperature during the growth.

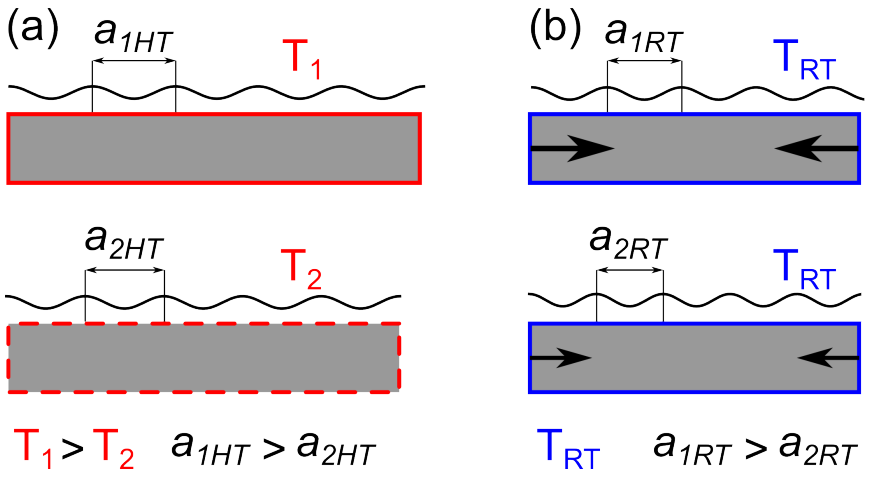

Figure 2.8: (a) Sketch of graphene grown on the same substrate at two different temperatures, T_1 and T_2, having two different moiré periodicity at high temperature highlighted by the buckling, a_1HT and a_2HT. (b) Sketch of the two samples at room temperature, the two substrates have now contracted down to the same size during the cooling and the two moiré periodicity are still different, with a_1RT larger than a_2RT.

The effect of the growth temperature have been observed on other systems, resulting in two different cases, either small misorientation among domains, or large angle variations, the rotational variants, often referred to as R*angle*. The small misorientations of the order of a degree maximum and their distribution depends on the growth temperature, a higher temperature results in a better crystallisation due to a higher adatom mobility and lower defects density [Coraux *et al.* , 2009, Hattab *et al.* , 2011]. It is thus possible to limit this rotational spreading by growing graphene at higher temperature if the goal is

to obtain high quality graphene. The rotational variants however are not totally dependant on the growth temperature. For example, several rotational domains have been observed on Pt(111) [Gao *et al.* , 2011], from 2° to a maximum of 30° rotations, each one having a different moiré superlattice, that are temperature dependant. The growth temperature will favour a certain variant but the others can also be present. However, decreasing the nucleation density has a determinant effect to limit their apparition [Gao *et al.* , 2011, Hattab *et al.* , 2011]. Various graphene rotational variants have also been reported on Au(111) [Nie *et al.* , 2012], Pd(111) [Murata *et al.* , 2010] or Ir(111) [Loginova *et al.* , 2009b]. All the growth processes in these studies have been done under 1000°C, highlighting again that growth under this temperature leads to the formation of rotated domains.

2.3.2 Strong/weak interaction

The interaction of the graphene with the various substrates it has been grown on has been investigated widely and the general issues associated have been reviewed in several publications [Batzill, 2012, Voloshina & Dedkov, 2012]. A major point is the possible hybridisation of the graphene electronic structure with its substrate, directly affecting the specific electronic transport and properties of the graphene in addition to its structure. Two structural parameters are greatly modified by the graphene/substrate interaction, the mean distance between the two and the buckling of the graphene. This graphene/metal separation distance ranges from 2.1 Å for Ni(111) or Ru(0001) up to 3.3 Å for Pt(111) or Cu(111) [Batzill, 2012], which is usually compared to the interlayer distance in HOPG, 3.35 Å. This broad range of separation shows that the interaction can be chemisorption or physisorption, *i.e.* covalent or van der Walls, or something between the two. This variation of interaction also leads to the buckling of the graphene over the moiré superlattice, as the separation distance is modulated by the coincidence of carbon atoms with the substrate.

Graphene buckling is of the order of one angstrom. That depends on several

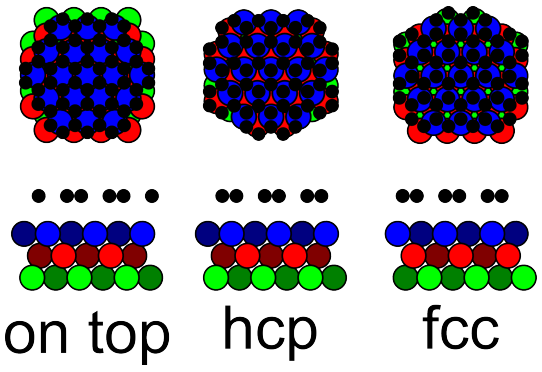

Figure 2.9: Sketches of the three possible coincidences of the graphene atoms, in black discs, with the substrate atoms of a fcc (111) surface, the top three layers atoms in blue, red and green, from a top view and side view. The first one on the left is the "on top" structure, where the graphene rings are centered on the atoms of the top substrate layer. The second is the "hcp", where one carbon atom of the unit cell is on top of the first substrate layer and the second one is on top of the third layer. The third one is the "fcc", carbon atoms are on top of the ones of the first two top layers of the substrate.

parameters, the main one being the type of substrate. This buckling is linked with the coincidence of the carbon atoms in the graphene with the atoms of the top layers of the substrate surface. The specific aspects of coincidence of carbon atoms with the substrate, with the questions and issues that come with it, will be developed in the next paragraph. In the specific case of fcc(111) and hcp(0001) surfaces, three different coincidences structure are present on the epitaxial graphene : on top, hcp and fcc, shown in Fig. 2.9. More complex moiré can be observed on surfaces with a different symmetry such as on Fe(110) [Vinogradov *et al.* , 2012], but this will not be discussed here. The height of the separation varies on these sites and the amplitude of the modulation has been a long standing debate on different systems, we will discuss further this issue in chapter 5.

2.4 Graphene on iridium

As we have discussed generally about epitaxial graphene on substrates in the previous paragraphs, we will now review in more detail the various studies about

graphene on Ir(111). Graphene grown on Ir(111) has been studied starting in 2006 by the group of T. Michely [N'Diaye *et al.* , 2006] and later by other groups [Loginova *et al.* , 2009b].

2.4.1 Growth conditions

The growth is done with CVD, TPG or the combination of the two in UHV conditions [Coraux *et al.* , 2009], this study showing the preferential nucleation sites at the step edges. The segregation growth process is also possible [Nie *et al.* , 2011], however the carbon solubility in iridium is low and the second layer begins to grow before the completion of the first one, thus preventing a layer by layer controlled growth. The carbon source mainly used is ethylene, but other molecules like coronene have also been used. The growth temperature range is between 600 and 1200°C for both CVD and TPG, with the effect on islands density and size that has been discussed previously, this is presented in Table 5.2. Partial pressure of ethylene as low as 5.10^{-10} mbar during CVD is able to yield graphene islands, where the maximum pressure is limited by the setup.

2.4.2 Structural parameters

One of the main attraction to study graphene on iridium is the possibility to grow graphene of high quality, with a low defect density and large domains. It has been observed that the domains keep a structural coherency over the steps of the iridium substrate, thus it is possible to achieve micrometer scale coherency [Coraux *et al.* , 2008]. This study also showed the presence of defects at the grain boundaries between two domains in the form of pentagon/heptagon pairs. A typical topographic feature of graphene on iridium also come from the growth, in particular the high temperatures involved. The graphene shows a network of wrinkles after cooling to room temperature post-growth, this has been observed with STM and low energy electron microscopy (LEEM)[N'Diaye *et al.* , 2009, Loginova *et al.* , 2009b] as shown in Fig. 2.10

and they have been observed to disappear also when bringing back the samples at high temperature. They are typically between 1 and 3 nm high and a few nanometers wide. Hattab *et al*. linked the growing and flattening of the wrinkles with the temperature evolution, showing a hysteresis of the graphene lattice parameter with temperature [Hattab *et al.* , 2012]. As the TEC of iridium and graphene are different, strains build up in the graphene during the cool down and is released by nucleating and growing wrinkles. The opposite process happens while heating by flattening them. However, we detail further the hysteretic behaviour of the lattice parameter in chapter 4, linking it with a shift between commensurate phases.

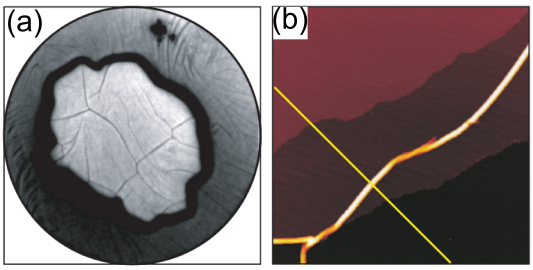

Figure 2.10: From Ref. [N'Diaye *et al.* , 2009] (a) LEEM image with a field of view of 10μm of a graphene island on Ir(111), showing a network of wrinkles. (b) STM topograph (240×240nm^2) of graphene on Ir(111) showing a wrinkle running across an atomic step, 3 nm high and a few nanometers wide.

The wrinkles represent a large change of topography, however, changes of topography can be more difficult to assess. Various structures and topography of graphene on Ir(111) have been observed and debated over the years, some are presented in Table 5.2. It is possible for example to grow rotational variants by changing the growth conditions [Loginova *et al.* , 2009b, Hattab *et al.* , 2011]. As discussed previously for epitaxial graphene in general, the growth temperature has a large influence on the growth of variants and this is highlighted in Table 5.2, in particular, the CVD process below 1000°C yields a large variety of variants in addition to the R0°. This table raises another issue : to observe and study epitaxial graphene, several techniques can be used, each with

their own strengths and weaknesses. STM is a standard technique to study surfaces, however, the tip, its reactivity in particular can affect enormously the observation [Dedkov & Voloshina, 2014]. A recent alternative for local probing is to use a tip with a carbon monoxide molecule [Hämäläinen *et al.* , 2013, Dedkov & Voloshina, 2014]. Another way to study this system is non-local probing, like diffraction techniques, such as LEED or SXRD, or x-ray standing wave (XSW). These allow to obtain topographic information that is not otherwise possible to assess experimentally. In particular, the mean separation distance with the substrate, evaluated around 3.39 Å, is close to the interlayer distance in graphite. On the opposite, the value of the corrugation of graphene do not have a consensus among the various studies, values from 0.31 Å to 1 Å have been reported [Voloshina *et al.* , 2013, Busse *et al.* , 2011]. This is linked closely with the interaction and electrons exchange with the substrate that will be discussed latter. Our SXRD results for the R0° variant will be presented in chapter 5. In addition to the ones observed experimentally, other possible rotations, with smaller corrugation than the observed R0°, have been tabulated in Ref. [Meng *et al.* , 2012]. However, this study is limited in scope by a fixed lattice parameter for the graphene while high resolution x-ray diffraction showed a smaller value and variations of the lattice parameter [Blanc *et al.* , 2012].

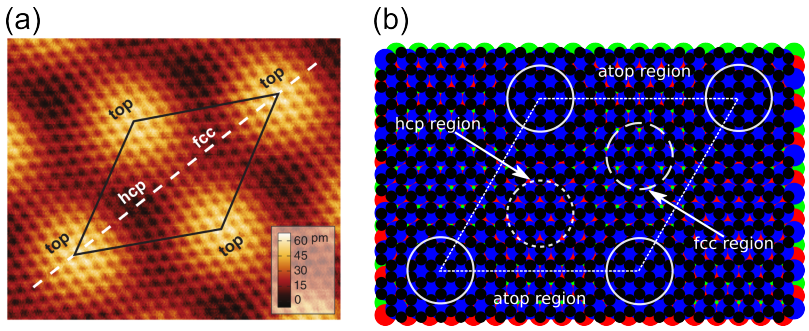

Figure 2.11: (a) SFM topograph from Ref. [Hämäläinen *et al.* , 2013], showing the moiré superstructure of graphene on Ir(111). (b) Sketch of the moiré superstructure, with the three regions, on top, hcp and fcc highlighted in white.

In addition to the topography, the type of commensurability of graphene on

structure	separation	corrugation	technique	growth method	Ref.
R0° incom. R0° incom.			STM, LEED	TPG 1200°C CVD 1050°C	[N'Diaye *et al.* , 2008] [N'Diaye *et al.* , 2008]
R0° R14° incom. R18.5° incom. R30°			STM, LEED	CVD CVD 830°C CVD 930°C CVD 830°C	[Loginova *et al.* , 2009b]
R0° incom. R0° $(10 \times 10)_{Gr}$	3.38 ± 0.4 Å 3.41 ± 0.4 Å	1 ± 0.2 Å 0.35 Å	XSW DFT	TPG 1250°C	[Busse *et al.* , 2011]
R0° $(10 \times 10)_{Gr}$ R14° $(4 \times 4)_{Gr}$ R19° $(3 \times 3)_{Gr}$ R23° $(\sqrt{19} \times \sqrt{19})_{Gr}$ R26° $(\sqrt{37} \times \sqrt{37})_{Gr}$ R30° $(2 \times 2)_{Gr}$		0.423 Å 0.101 Å 0.051 Å 0.022 Å 0.015 Å 0.012 Å	STM, LEED, DFT	CVD 850°C	[Meng *et al.* , 2012]
R0° $(21 \times 21)_{Gr}$ + incom.			SXRD, STM	TPG 1200°C + CVD 1000°C	[Blanc *et al.* , 2012] [Blanc *et al.* , 2012]
R0° incom. R0° $(10 \times 10)_{Gr}$	3.39 ± 0.03 Å	0.47 ± 0.5 Å 0.43 ± 0.09 Å	AFM LEED	CVD 1050°C	[Hämäläinen *et al.* , 2013]
R0° $(10 \times 10)_{Gr}$		0.31 Å	DFT,AFM	CVD 1100°C	[Voloshina *et al.* , 2013]
R0° $(10 \times 10)_{Gr}$	3.41 ± 0.4 Å	$0.4 - 1$ Å	SWX, DFT	TPG 1050-1200°C	[Runte *et al.* , 2014] [Runte *et al.* , 2014]

Table 2.1: Comparative table of the various structures and topographic parameters of graphene on Ir(111) reported in the literature.

iridium has been discussed over the years, much like graphene on Ru(0001). In the case of the graphene with no rotation, it was first reported with a STM study that it is incommensurate, despite being close to a $(10 \times 10)_{Gr}$ matching $(9 \times 9)_{Ir}$ [N'Diaye *et al.* , 2006], with a moiré supercell lattice of 25.3±0.5 Å. Later, with additional LEED measurements, which gave a moiré lattice of 25.8±2Å [N'Diaye *et al.* , 2008], the incommensurate structure was confirmed. Moreover,the analysis showed that graphene lattice parameter was slightly smaller by 0.4%, compared to graphite, indicating a permanent strain of the graphene. The possibility to have commensurability of graphene on Ir(111) was raised with the determination of more complex structures in Ref. [Meng *et al.* , 2012], despite the criticism raised before at the beginning of this section. Moreover, the graphene lattice parameter at room temperature was found to vary with the growth temperature and also, at the same growth tem-

perature [Blanc *et al.* , 2012]. For slightly differing preparation conditions the measured values pointing at several incommensurabilities. In addition, the moiré lattice was found to be smaller than 25.6±0.2 Å. The explanation for the variation of the lattice parameter is that the epitaxial graphene is more complex than being incommensurate. In fact, commensurate domains tens of nanometers large, $(10 \times 10)_{Gr}$ matching $(9 \times 9)_{Ir}$ and $(21 \times 21)_{Gr}$ matching $(19 \times 19)_{Ir}$, would coexist with incommensurate domain walls of the order of 100 nm. The domains sizes mentioned are also the typical size of atomic terraces on iridium single crystals. The domains size is thus presumably limited by the presence of steps. This shows the limits of the idea of "perfect" epitaxial graphene on Ir(111). Even the R0° variant has defects, wrinkles, a distribution of small rotations, domains with slightly different lattice parameters, thus commensurate and incommensurate domains. We will discuss further this issue in later chapters 4. During our studies, we observed various commensurate structures during the CVD growth and with a full layer during temperature scans, pointing towards a tendency of the graphene on Ir(111) to commensurability.

2.4.3 Electronic structure

The electronic structure and electronic exchange of graphene on Ir(111) was determined using angle resolved photo-electron spectroscopy (ARPES) [Pletikosić *et al.* , 2009], x-ray photoelectron spectroscopy (XPS) and $ab-initio$ calculations [Busse *et al.* , 2011]. The electronic exchange and thus binding with the substrate is also modulated over the moiré superlattice, the average binding per carbon atom being -50 meV but the binding is stronger in the fcc and hcp regions, where there is an hybridization between the carbon atoms located above iridium atoms. Globally the graphene is physisorbed but locally chemisorbed. The ARPES study was done on graphene with no rotation with the substrate and shows the presence of a Dirac cone. Moreover, the estimated position of the Dirac point above the Fermi level indicates that the graphene is slightly p-doped, which is confirmed by DFT [Busse *et al.* , 2011] evaluating a loss of 0.01 electron per carbon atom,

i.e. 2 electrons per moiré lattice. Additional features have been observed too, with surface states coming from the iridium. More importantly, the graphene Dirac cone is replicated by the moiré reciprocal vectors close to the original one. Their intersection results in minigaps on the Dirac cone, of the order of 0.1-0.2 eV. These results shows that there is no hybridization of the graphene electronic bands with the substrate over a large energy range, but there is probably an hybridation with the surface states of the metal around the Fermi level, overall suggesting a weak interaction between the two. This was confirmed by another study [Starodub *et al.* , 2011], but for graphene domains with a 30° rotation. No minigap was found due to the change in the reciprocal space with the rotation. These rotated domains are more doped than the non-rotated ones and thus show a stronger interaction with the substrate, contrarily to what was suggested with the topographic parameters, in particular the smaller buckling. This would point towards a stronger interaction than presumed, similar to that of the earliest nucleation stage of the growth [Lacovig *et al.* , 2009]. Moreover, another minigap at lower energy was also observed, coming from the intersection of the Dirac cone with the mini Brillouin zones. Finally, graphene could be used to preserve and protect surface effects from the iridium, such as the Rashba effect [Varykhalov *et al.* , 2012, Sánchez-Barriga *et al.* , 2013]. This is a typical surface effect that cannot be observed when the iridium is exposed to atmospheric pressure. However, graphene grown on top protects it and this could lead to other surface effects to be protected and used in atmospheric conditions, thus opening new possible applications.

2.4.4 Graphene on Ir(111), a basis for more complex systems

We have discussed the growth, structure and characteristics of epitaxial graphene on metals during the previous paragraphs of this chapter. These systems are also the basis for more complex studies, as various materials can be intercalated at the interface between graphene and the metal, changing their

structures and properties or adding new ones. In addition, the moiré superstructure can be used to grow self-organized nanoparticles, for various potential uses as we have discussed previously in chapter 1. We are going to briefly review some of these systems that use graphene on Ir(111) as a starting point. The intercalation of various species below the graphene to add or induce new properties has been investigated for potential applications in several fields, spintronics in particular.

The intercalation processes can be achieved on either full-grown graphene layers or graphene islands. In the first case, the element is deposited first on top of graphene and the intercalation happens during annealing, between 200 and 300°C for cobalt for example [Rougemaille *et al.* , 2012]. However, graphene is know to be impermeable to any species, even helium. The elements must pass below through defects in the graphene, but the origin of these defects has been debated. On intentionally defective graphene on Ir(111), intercalation processes are observed at relatively low temperature, around 200°C for cobalt [Coraux *et al.* , 2012]. By comparison, cobalt intercalation on high quality graphene happens at higher temperature, more than 700°C. This reveals the effect of the density of defect over the intercalation. When the density is low, higher temperatures gives to the cobalt atom the needed mobility to travel over the graphene to a defective area. The intercalation of cobalt is motivated to study the influence of graphene on the magnetic anisotropy. In fact, cobalt atoms hybridize with graphene, showing a magnetisation mainly out-plane with at maximum 11 monolayers intercalated. This is not observed on cobalt deposited on Ir(111) alone; the change to in-plane magnetisation occurring around 6 deposited monolayers.

Another intercalation mechanism at the edge of the graphene has been observed with not only metals but also with molecular gases. This is observed when the graphene coverage is partial, either on disconnected graphene islands or on graphene with patches of substrate still exposed. Intercalation of cobalt has been observed to differ depending on the orientation relationship between graphene

and the iridium substrate [Vlaic *et al.* , 2014]. Cobalt intercalation happens preferentially around wrinkles on rotated domains, unlike domains with no rotations where cobalt is found in the area of the substrate step edges. This shows that the intercalation processes depend on the structure of the graphene/metal system, as the energy barrier due to graphene bonding defines where the intercalation can happen. In the case of gas intercalation, two different motivations can be noted, the first is to decouple graphene from the substrate and the second is to understand how the samples are altered with time when removed from the growth chamber. The evolution of oxygen intercalation on graphene on Ir(111) has been studied by Kimouche *et al.* [Kimouche *et al.* , 2014]. The oxygen was observed to enter through graphene-free regions. The oxide expands preferentially following graphene wrinkles, as they facilitates the diffusion of oxygen as opposed to the flatter regions where graphene is bonded with the substrate, similarly to cobalt intercalation. The time evolution is observed over a week, where the oxide width is self-limited around 100 nm, highlighting the difficulty for atoms to diffuse in area away from the wrinkles and graphene edges. The energy barrier limiting the intercalation processes is well depicted in Ref. [Granas *et al.* , 2012], where Pt nanoparticles were grown first on the moiré of graphene on Ir(111). The nanoparticles prevent oxygen from intercalating between the substrate and graphene where they are located. The full decoration of graphene edges by Pt agglomerates prevents intercalation in areas with only bare graphene. In addition, graphene islands situated in the middle of an iridium terrace are found to be resistant to intercalation, while those located at an atomic step do not. The chemical bond of the graphene with the substrate at its edges is thus too strong for the oxygen to pass through, making it another example of the energy barrier stopping intercalation.

The intercalation of a layer below graphene could be a way to isolate it from its substrate without transfer on another substrate, a $Si0_2$ wafer for example. The possibility to make devices onto high quality graphene without transfer, thus limiting pollution and defects due to the transfer method, would

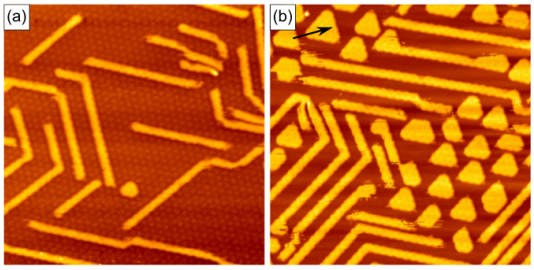

Figure 2.12: From Ref. [Schumacher *et al.* , 2013] Eu intercalation observed with STM (80×80 nm) (a) 18% Eu monolayer intercalated (b)39% Eu monolayer intercalated

be interesting in various domains. This method of using a gas to isolate the graphene has also been used with carbon monoxide [Granas *et al.* , 2013] on graphene on iridium. This intercalation results in a structure observed in STM and LEED similar to graphene domains with a 30° rotation with the substrate. However, the intercalation is not complete, areas and stripes of non-intercalated graphene can be observed, and corresponds in majority to moiré sites where the graphene is slightly chemisorbed. In addition, graphene cannot be considered completely isolated and equivalent to free-standing graphene as it is *p*-doped. The opposite would be to intercalate an element to modify further the electronic structure of graphene. For example, copper intercalation in graphene on Ir(111) [Vita *et al.* , 2014] has shown a stronger hybridisation of the graphene after intercalation, resulting in a gap opening at the Dirac point.

2.5 Conclusion

In this chapter we have discuss the structure and topography of epitaxial graphene on metals, showing the various growth methods and their specificity and impact on the graphene. The final structure is deeply influence by the nature of the substrate, as the interaction between the graphene and the substrate varies continuously between chemisorption and physisorption. Moreover, the mismatch between the two lattice parameters yielding a superlattice similar to

a moiré effect adds a modulation to the graphene/metal interaction. Several defects have been observed too, rotational domains or wrinkles for example. This influences the graphene properties, as variation in the atomic structure can modify the graphene properties, for example its electronic structure, thus motivating a deeper understanding of their origins. It is then possible to modify the interaction with the substrate and the graphene structure by using the intercalation processes. Thus, it is possible to tailor the strain and structure of epitaxial graphene and this could be used to build upon to create more complex systems with new or specific properties. These issues and challenges have been one of the motivation to better understand the structure variation and strain during growth and post-growth due to cooling of graphene on Ir(111), shown in chapters 4 and 5, as it is the basis system to organize nanoparticles on top.

Chapter 3

Diffraction and Experimental Considerations

3.1 Introduction

This chapter is dedicated to explain the techniques, methods and experimental considerations used to obtain the results presented in latter chapters. This includes firstly, the interaction of x-rays with matter in a general case, addressing some key aspects of diffraction by a crystal. Then the case of surface diffraction will be discussed, in particular in the specific system of epitaxial graphene on Ir(111). The experimental set-up will also be presented. This chapter will be concluded with considerations concerning measurements with a 2D detector and processing the corresponding data.

X-rays have been used since the beginning of the XX$^{\text{th}}$ century in a wide range of scientific domains to study all kinds of materials, from biology to determine the complex structure of proteins, to archaeology to probe artefacts without damaging them and to physics and chemistry to study the structure of

matter and reactions at the atomic level. Since the middle of the 1980s, large facilities have been dedicated to generate more intense and less divergent x-ray beams. These facilities are called synchrotron radiation sources and are now at the third generation, such as the ESRF, with a brilliance 13 orders of magnitude larger than the first x-ray tubes. They provide beams that can be focused into submicron size.

New techniques of characterizations have been developed in parallel to the exponential development of materials ordered at the nanoscale since the 1980s. At variance with bulk materials, many properties of low dimensional system are governed by structural changes at the boundaries (surfaces, interfaces), which represent a large fraction of the atoms in the system. New experimental set-ups have been developed with new techniques to study specifically surfaces, for instance combining ultra-high vacuum environments for in situ sample preparation, limiting surface pollutions, and specific diffractometers designed for surface x-ray diffraction and scattering [Brennan & Eisenberger, 1984, Fuoss & Robinson, 1984].

3.2 X-ray penetration in matter

X-rays are electromagnetic waves, that can be refracted at an interface between vacuum and a material. This phenomenon is described by the Snell-Descartes law

$$\cos\alpha = n\cos\alpha' \tag{3.1}$$

with α the incident angle on the interface, n the optical index of the material and α' the refracted angle. For x-ray photon in matter, the Snell-Descartes law may be employed as well, provided that a complex optical index is used:

$$n = 1 - \delta + i\beta \tag{3.2}$$

with

$$\delta = \frac{e^2}{2\pi mc^2} N_a \frac{\sum_j (f_j - f'_j)}{\sum_j A_j} \rho\lambda^2 \text{ and } \beta = \frac{e^2}{2\pi mc^2} N_a \frac{\sum_j (f''_j)}{\sum_j A_j} \rho\lambda^2 \tag{3.3}$$

N_a is the Avogadro's number, A_j, f_j, f'_j and f''_j are respectively the atomic mass, the scattering, dispersion and absorption factors of the j the atomic species, ρ its density and λ the wavelength. Typically, δ has a value around 10^{-5} and β around 10^{-6} in solids. The real part of n being small than one accounts for the total external reflection phenomena, which occurs when x-rays imping the surface under a critical angle defined as

$$\alpha_c \approx \sqrt{2\delta} \tag{3.4}$$

This critical angle varies depending on the material between 0.1 and 0.5° and is equal to 0.419° for iridium with a 1.12 Å wavelength. However, even below the critical angle, an evanescent wave enters the material over a certain depth defined as

$$\Lambda = \frac{\lambda}{4\pi Im(\alpha')} \tag{3.5}$$

This penetration length is typically of the order of tens of Å, in iridium it is 13.9 Å with a 1.12 Å wavelength and a 0.2° incident angle for example.

3.3 Diffraction in a bulk crystal

The diffraction of x-rays by a bulk crystal will be described here step by step, starting with two electrons, as the electromagnetic waves interact with the atomic electronic cloud, and gradually adding complexity to obtain the full crystal. This has been explained in details in various books and courses such as Elements of Modern X-Ray Physics [Als-Nielsen & McMorrow, 2001].

We consider first the interaction of the incident and scattered photons with two electrons, separated by a vector $\mathbf{r}$. The photons can be seen as waves,

associated with wavevectors $\mathbf{k}_i$ and $\mathbf{k}_f$ respectively for the incident and exiting waves. Only elastic scattering is considered here, thus the two wavenumbers moduli are equal, $|\mathbf{k}_i| = |\mathbf{k}_f| = 2\pi/\lambda$. Incident and exiting waves both have a phase, $\mathbf{k}_{i,f} \cdot \mathbf{r}$, thus the phase difference between the two defines the momentum transfer $\mathbf{q}$, $\phi = (\mathbf{k}_f - \mathbf{k}_i) \cdot \mathbf{r} = \mathbf{q} \cdot \mathbf{r}$. The amplitude of the momentum transfer is also linked to the scattering angle θ :

$$|\mathbf{q}| = (4\pi/\lambda) \sin\theta \tag{3.6}$$

From a classical point of view, atoms can be described as a cloud of electrons orbiting around the nucleus. Instead of the previous two electrons, here a certain number of electrons, depending on the type of atom or ion, are distributed with a density $\rho(\mathbf{r})$ around the nucleus. The atomic form factor can thus be written as

$$f_j(q) = \int \rho(\mathbf{r}) e^{i\mathbf{qr}} d\mathbf{r} \tag{3.7}$$

This gives the scattering amplitude of a single atom j, equal to 0 when $\mathbf{q}$ tends to infinity and equal to Z, the number of electrons in the atom, when $\mathbf{q}$ is equal to 0. Moreover, this highlights the fact that light atoms such as carbon will have a form factor smaller than heavier ones such as iridium, thus in our case, effectively limiting the size of reciprocal space where graphene has a measurable signal as shown in Fig. 3.1.

Crystals are composed of atoms arranged periodically along the three directions in a bulk crystal. Among the possible repeat patterns (unit cells) which may be defined to map the crystal, the smallest one is known as the primitive unit cell A 3D lattice can be expressed as a set of vectors written as

$$\mathbf{R} = n_1\mathbf{a} + n_2\mathbf{b} + n_3\mathbf{c} \ , (n_1, n_2, n_3) \in \mathbb{Z} \tag{3.8}$$

$\mathbf{a}, \mathbf{b}$ and $\mathbf{c}$ are the primitive vectors of the primitive unit cell. However, this primitive cell is not always the most convenient to describe a crystal, especially

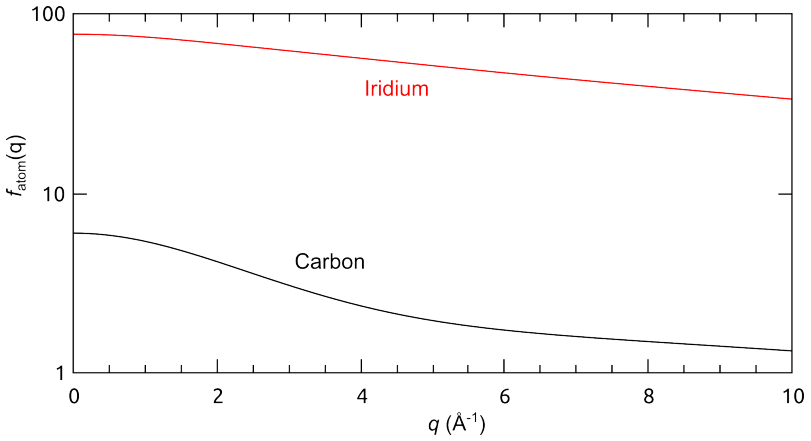

Figure 3.1: Comparison of the evolution between the atomic from factor $f_{atom}(q)$ of carbon in black and iridium in red as a function of q.

when considering a crystal surface. The (111) surface of iridium is the basis for the samples studied in this manuscript, iridium is a face-centred cubic crystal as shown in Fig. 3.2. New vectors, linear combinations of the three vectors of the bulk unit cell, are chosen to describe the unit cell of the surface lattice, the first two vectors, $\mathbf{a}_s$ and $\mathbf{b}_s$ being in the (111) plane, and the third vector perpendicular to it :

$$\begin{aligned} \mathbf{a}_s &= \frac{1}{2}(-\mathbf{a}_{bulk} + \mathbf{b}_{bulk}) \\ \mathbf{b}_s &= \frac{1}{2}(\mathbf{c}_{bulk} - \mathbf{b}_{bulk}) \\ \mathbf{c}_s &= \mathbf{a}_{bulk} + \mathbf{b}_{bulk} + \mathbf{c}_{bulk} \end{aligned} \tag{3.9}$$

Since the unit cell is defined, one can assess its scattering amplitude by combining the atomic factor and the unit cell. The structure factor $F_{unit\ cell}(\mathbf{q})$ is the sum over the n atoms in the unit cell :

$$F_{unit\ cell}(\mathbf{q}) = \sum_{j}^{n} f_j(\mathbf{q}) \cdot e^{i\mathbf{q}\mathbf{r}_j} \tag{3.10}$$

with an atom j being in a position $\mathbf{r}_j$ in the unit cell.

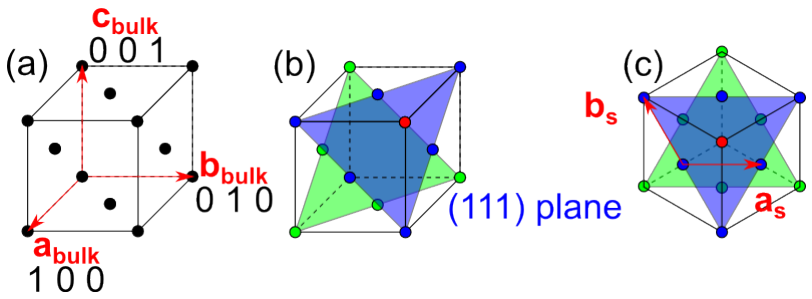

Figure 3.2: (a) Crystal unit cell of a face-centred cubic lattice, with the three vectors $\mathbf{a}_{bulk}, \mathbf{b}_{bulk}$ and $\mathbf{c}_{bulk}$ in red with their coordinates in black. (b) Same unit cell with the (111) planes and lattice points in them highlighted in green, blue and red. (c) Top view of the surface unit cell with the new vectors $\mathbf{a}_s$ and $\mathbf{b}_s$ in red.

From the structure factor of a unit cell, the structure factor of the full crystal can be determined. To achieve this, one has to take all the atomic structure factors of the crystal by summing over the unit cell and crystal lattice $\mathbf{R}_k$

$$F_{crystal}(\mathbf{q}) = \sum_k \sum_j f_j(\mathbf{q}) \cdot e^{i\mathbf{q}(\mathbf{r}_j+\mathbf{R}_k)} = \underbrace{\sum_j f_j(\mathbf{q}) \cdot e^{i\mathbf{q}\mathbf{r}_j}}_{F_{unit\ cell}(\mathbf{q})} \cdot \underbrace{\sum_k e^{i\mathbf{q}\mathbf{R}_k}}_{S(\mathbf{q})} \tag{3.11}$$

The lattice sum $S(\mathbf{q})$ can be separated along the three directions 1, 2 and 3. In a crystal of $n_1 \times n_2 \times n_3$ atoms, this sum is expressed as :

$$\begin{aligned} S(\mathbf{q}) = \sum_{k=1}^{m} e^{i\mathbf{q}\mathbf{R}_k} &= \sum_{n_1,n_2,n_3} e^{i(h\mathbf{a}^*+k\mathbf{b}^*+l\mathbf{c}^*)\cdot(n_1\mathbf{a}+n_2\mathbf{b}+n_3\mathbf{c})} \\ &= S_{n_1}(\mathbf{q})S_{n_2}(\mathbf{q})S_{n_3}(\mathbf{q}) = \sum_{n_1} e^{ihn_1} \sum_{n_2} e^{ikn_2} \sum_{n_3} e^{iln_3} \end{aligned} \tag{3.12}$$

All the terms in the lattice sum are complex numbers, each with a modulus equal to 1 and a phase. That sum is made over a large number, of the order of Avogadro's number, 10^{21}, in a macroscopic sample. This sum can equal to a very large number, *i.e.* in the case where all the phases are equal to a multiple of 2π. These cases correspond to the condition

$$\mathbf{q} \cdot \mathbf{R_k} = 2\pi \times integer \tag{3.13}$$

These conditions defines a new lattice, the reciprocal lattice, which can be constructed from the crystal lattice in real space This lattice is constructed with vectors fulfilling the previous condition and thus defined as

$$\mathbf{x}_i \cdot \mathbf{x}_j^* = 2\pi\delta_{ij} \tag{3.14}$$

with $\mathbf{x}_i$ being $\mathbf{a}$, $\mathbf{b}$ or $\mathbf{c}$ and δ_{ij} a delta function, equal to 1 when $i = j$ and 0 otherwise. The reciprocal lattice is expressed as a set of vectors, written

$$\mathbf{G} = h\mathbf{a}^* + k\mathbf{b}^* + l\mathbf{c}^* \tag{3.15}$$

where h, k, l integers and are called the Miller indices. When $\mathbf{q}$ is not equal to a reciprocal lattice vector, the amplitude scattered by the bulk crystal will be close to zero. The condition to observe x-ray diffraction, $\mathbf{q} = \mathbf{G}$, is known as the Laue condition, when all scattered waves interfere constructively.

In experiments, detectors are sensitive to the squared scattered amplitude, i.e. the square of the structure factor:

$$I_{crystal}(\mathbf{q}) = CF^2_{unit\,cell}(\mathbf{q})S^2_{n_1}(\mathbf{q})S^2_{n_2}(\mathbf{q})S^2_{n_3}(\mathbf{q}) \tag{3.16}$$

where C is a constant. Information about the scattering phase, hence about the individual atomic positions, is thus not directly accessible. The positions where there are local maxima in intensity are called Bragg peaks and they are indexed using the (integer) Miller indices h, k and l.

The Laue condition can be expressed geometrically. The so-called Ewald sphere, whose radius in the norm of the wavevectors $2\pi/\lambda$, is the trace of the end of incoming and scattered wavevectors in an elastic scattering experiment (Fig.3.3). The possible scattering vectors $\mathbf{q}$ are define arcs on this sphere. Ful-

filling one Laue's conditions thus is equivalent to rotating the reciprocal lattice of the crystal so that the center of the reciprocal lattice and a another reciprocal lattice point define an arc on the Ewald's sphere, which allows to infer the possible scattering vector (Fig. 3.3).

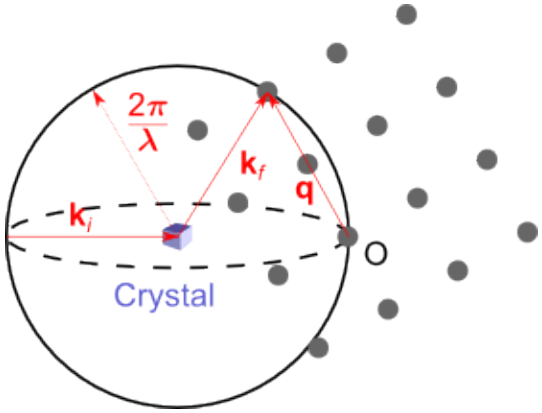

Figure 3.3: Sketch of the Ewald sphere in black, the Bragg peaks are in grey, the wavevectors $\mathbf{k}_i$, and $\mathbf{k}_f$ and the momentum transfer $\mathbf{q}$ as red arrows and the crystal in blue.

We have seen the diffraction of x-ray by a bulk crystal, resulting in maxima of the scattered intensity located at certain positions in space. These maxima are associated with Dirac functions as the crystal is considered infinite in all directions. However, in reality a crystal is not infinite and we will see next how this affects the scattered intensity, in particular for a flat surface.

3.4 Surface diffraction

3.4.1 Crystal truncation rods

In Ref. [Robinson, 1986], I. K. Robinson described in details what happens when a crystal is no longer infinite, but has sharp boundaries, as shown in Fig. 3.4.1. The change of shape, the new well defined surface, influences directly the scattering, as it is no longer isotropic. This results in streaks instead of Bragg peaks along the axis perpendicular to the surface. These streaks are known as

crystal truncation rods (CTRs).

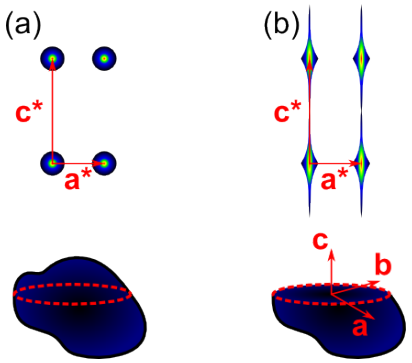

Figure 3.4: (a) In the top part, a 2D representation of the reciprocal lattice with Bragg peaks is sketched, showing the ideal case of x-rays scattering by a bulk crystal shown in the bottom part. (b) As the crystal in the bottom is cleaved perpendicular to the **c** axis, leaving a sharp boundary, it results in the reciprocal space streaks along the $\mathbf{c}^*$ axis instead of peaks known as crystal truncation rods, with maxima at the same positions as the Bragg peaks.

A crystal surface can be seen as the convolution of the previous infinite ideal crystal with a step function for the electron density $\rho(\mathbf{r})$. The CTRs have a modulation along their axis, with a maximum at the position of the Bragg peaks of an infinite 3D crystal and a non-zero value otherwise. The shape and modulation of the CTRs are modified by the state of the crystal surface in various ways. For example, the surface roughness decreases the scattered intensity away from the maxima along the rods, or a miscut of crystal surface leads to a misalignment of the CTRs with their axis. To express the scattered intensity and the structure factor of the CTRs, we will assume that the crystal is still infinite in the **a** and **b** directions and that the cleaved surface is perpendicular to the **c** axis. By using these conventions, the sums $S_{n_1}(\mathbf{q})$ and $S_{n_2}(\mathbf{q})$ still yield Dirac functions. For a simple unit cell (comprising only one atomic plane), one can then express the cleaved crystal as a stack of atomic layers, with the scattered amplitude of one layer $F_{layer}(\mathbf{q})$ and $e^{-\beta}$ the absorption per plane, the

scattered amplitude of the stack is expressed as :

$$F_{CTR}(\mathbf{q}) = F_{layer}(\mathbf{q}) \sum_{j=0}^{\infty} e^{iq_z cj} e^{-j\beta} = \frac{F_{layer}(\mathbf{q})}{1 - e^{i2\pi l} e^{-\beta}} \tag{3.17}$$

as the momentum transfer along the perpendicular axis to the surface is $q_z = 2\pi l/c$. The scattered intensity along the CTR is then (with $\beta \to 0$)

$$I_{CTR} = |F_{CTR}(\mathbf{q})|^2 = \frac{|F_{layer}(\mathbf{q})|^2}{4\sin^2(\pi l)} \tag{3.18}$$

This is obviously only true when l is not an integer, because it diverges when $\sin(\pi l)$ is equal to zero, i.e. for a Bragg condition.

We can now apply this to our iridium single crystal, using the surface lattice vectors to determine where are the maxima of the CTRs in this specific case. Three (111) planes are in a ABC stacking along one $\mathbf{c}_s$ lattice vector, the relation between A and B, and B and C is a translation $\mathbf{t}$ (1/3, 2/3, 1/3) along the unit cell vectors directions defined previously. $F_{CTR}(\mathbf{q})$ can thus be dissociated using this translation as

$$F_{CTR}(\mathbf{q}) = F_{111}(\mathbf{q})(1 + e^{-i\mathbf{q}\cdot\mathbf{t}} + e^{-i2\mathbf{q}\cdot\mathbf{t}}) \tag{3.19}$$

Thus depending of the position (hk) in the $\mathbf{a}_s^*\mathbf{b}_s^*$ plane, the position of the maxima will shift along the $\mathbf{c}_s^*$ direction. This is shown in a cut of the reciprocal space in Fig. 3.4.1.

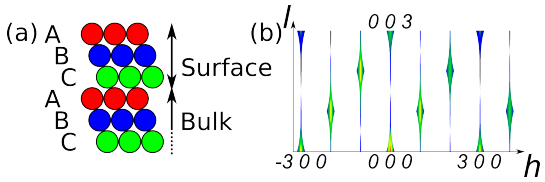

Figure 3.5: (a) Sketch of the ABC stacking of the (111) planes of iridium. (b) Cut of the reciprocal space along the h and l axes, highlighting the position of the maxima along the CTRs for an Ir(111) surface.

3.4.2 Diffraction by a monoatomic layer

As we have seen previously, the scattered intensity from the surface of a crystal gives rods with a modulation along the l-direction. But graphene is a monoatomic layer and one has only to consider the scattering amplitude $F_{layer}(\mathbf{q})$ in this case. A perfectly flat atomic layer only yield rods without modulation in the reciprocal space along l, positioned at integer values of h and k. In Fig. 3.4.2, the Fourier transform of an infinite flat sheet of graphene is sketched, the result is a set of rods. It has been shown for monolayer graphene on SiC by Charrier *et al.* [Charrier *et al.* , 2002] that the scattered intensity decreases slowly along the l-direction. This is caused by the atomic structure factor as we have discussed previously, as the scattered intensity decreases when $\mathbf{q}$ increases all the more in the case of graphene, as carbon is a light atom with few electrons.

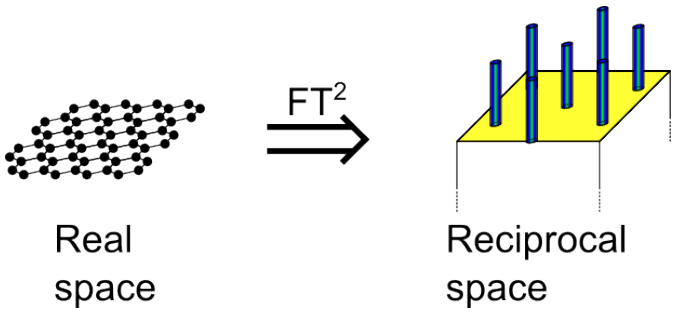

Figure 3.6: A flat graphene sheet and the resulting rods in the reciprocal space.

However, a perfectly flat graphene sheet is not possible in the case of epitaxial graphene. We have discussed in chapter 2, and will see latter in chapter 5, that the graphene is corrugated, so that the scattered intensity along the rods becomes modulated. This is also the case when nanoparticles are grown on top of the graphene as we will see in chapter 6.

3.4.3 Surface diffraction and moiré effect

As we have seen previously in chapter 2, epitaxial graphene and its various substrates do not have the same lattice parameters. This gives rise to a coincidence effect, analogue to a moiré effect and referred as such as we have seen previously. This leads to an additional lattice in the system. The period of the moiré is defined by the lattices composing it :

$$\frac{1}{a_{moiré}} = \frac{1}{a_{Gr}} - \frac{1}{a_{Ir}} \tag{3.20}$$

In the reciprocal space, this translates to

$$\mathbf{a}^*_{moiré} = \mathbf{a}^*_{Gr} - \mathbf{a}^*_{Ir} \tag{3.21}$$

This results in an additional smaller lattice in reciprocal space, made of rods emerging at each node of it. These are also called satellites reflections. Such a system results in a complex pattern in reciprocal space, as shown in Fig.3.4.3, with the iridium CTRs, the graphene rods and the moiré rods. The satellites rods are displaced from the CTRs and graphene rods by a multiple of $a^*_{moiré}$ and accordingly to the symmetry of the moiré along the h and k directions. Moreover, the scattered intensity in these rods decreases the further away they are from the CTRs or graphene rods, meaning that during a measurement, the first order can usually be measured but higher orders cannot be observed on all systems. This depends on the modulation in the moiré itself and will be discussed in chapter 5.

3.5 Experimental set-up

The results presented in the next Sections have been acquired during campaigns of experiments at the European Synchrotron Radiation Facility (ESRF), at the BM32 and ID03 beamlines. Both beamlines have a similar set-up, a z-axis diffractometer coupled with a ultra-high vacuum chamber (UHV). More-

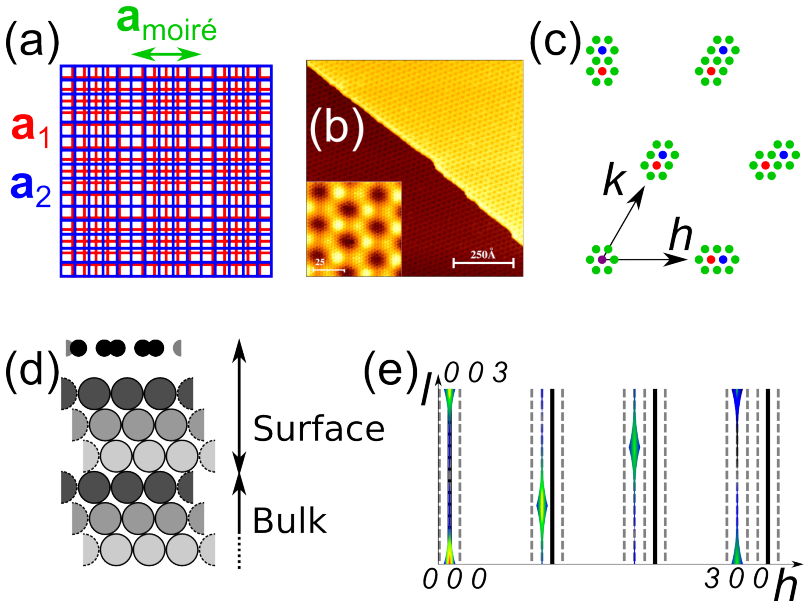

Figure 3.7: (a) Sketch of a 2D square moiré effect with two different red and blue lattices, with periods a_1 and a_2, superimposed on each other resulting in a moiré with a lattice parameter $a_{moiré}$ shown in green. (b) STM picture from Ref. [N'Diaye *et al.* , 2008] showing the moiré effect of graphene on Ir(111). (c) Sketch of the reciprocal lattice of graphene on Ir(111) in the hk-plane, both direction shown by black arrows. Positions of the Ir CTRs are shown in red, graphene rods in blue, first order of moiré rods in green (only the first order is shown here for clarity) and the origin of the reciprocal plane is shown in purple as a CTR and a rod are superimposed here. (d) Sketch of the ABC stacking of the (111) planes of iridium, with a graphene sheet on top. (e) Cut of the reciprocal space along the h axis, with the Ir CTRs in a colour gradient with the maxima at the Bragg peaks, the graphene rods in black and several moiré rods in dashed grey lines, only the closest to the CTRs and graphene rods are shown for clarity.

over, they both have the same kind of 2D x-ray detector, called the Maxipix. We will focus on the BM32 set-up in particular, which has been described in details in Ref. [Renaud *et al.* , 2009].

3.5.1 The synchrotron x-ray source

The ESRF is a third generation synchrotron radition source, with the storage ring composed of straight parts, undulators, and bent parts, the bending magnets. The production of x-rays is done in several steps using relativistic

electrons and radial acceleration. The starting point is the emission of packets of electrons by a thermoionic triode electrostatic gun, the emitted electrons have an energy of 100 keV. They are injected in a linear accelerator (LINAC) and accelerated to 200 MeV. Then they enter a 300 m of circumference, booster ring where they are accelerated to 6 GeV. Finally, the electron packets are injected in the storage ring, which has a circumference of 844 m, where they are kept at a constant energy. Here, they produce the synchrotron radiation as they are subjected to a radial acceleration either in the undulators or by the bending magnets. The electron packets are always kept under ultra-high vacuum (UHV) conditions to limit the losses, however, there is a constant decrease of the stored current over time, thus a decrease of the radiation flux. The storage ring is thus refilled every 12 hours and this variation has to be taken into account during measurements, the data has to be normalized to correct this effect. The undulators are composed of a series of dipole magnets that make the electrons packets oscillate thus increasing the number of emitted x-ray photons. The ID03 beamline uses three undulators to produce the x-ray beam used for the diffraction. The undulators can be modified and adapted to enhance the number of photon of a range of energy depending on the range used on the beamline; hard x-ray for diffraction or soft x-rays for magnetic studies for example. BM32 receives its x-rays from a bending magnet section, the part of the storage ring used to curve the path of the electrons. The energy spectrum of the bending magnet source is broader than that from an undulator source, and continuous. When emitted from the various sections of the storage ring, the x-ray beam enters the various beamlines through theirs optics.

3.5.2 The beamline optics

The x-ray beam entering a beamline is divergent and is not monochromatic. Before it can be used for experiments, it has to be shaped, focussed and monochromatized. The optics are positioned 30 m after the source and the sample 30 m away after it inside the UHV chamber, thus it makes an image of

the source on the sample. The first part of the BM32 optics is a silicon mirror coated with iridium, which is used to collimate the beam onto the monochromator. The monochromator is composed of two Si(111) crystals, the first one allows to choose the energy, *i.e.* the wavelength, of the beam and the second one is used to focus the beam horizontally. The energy range accessible on BM32 is between 7 and 30 keV, the flux of the beam is maximum at 20 keV with 5.10^{11} ph.s^{-1}. The last part is a second mirror that focusses the beam vertically. When exiting the optics, the beam has a size of 250 μm horizontally and 180 μm vertically, and has a divergence of 1 mrad horizontally and 0.13 mrad vertically.

3.5.3 The UHV chamber

The UHV set-up is composed of several parts as shown in Fig. 3.5.3 and has been described in Ref. [Santis *et al.* , 1999, Renaud *et al.* , 2009]. Firstly, there is the modutrack, where the samples can be loaded and stored on a cart moved mechanically between its different sections. The first one is the load-lock module, it can be closed off the rest of the modutrack to allow removal or entry of samples under an nitrogen atmosphere without breaking the vacuum in the whole modutrack, thus limiting the pollution in the whole set-up. The second section has a long rod to transfer the samples into the main chamber. In the third one, there is an oven to degas the samples before transferring them into the main chamber, again to limit the possible pollution in it. The rest of the modutrack is used for various purposes and can be adapted accordingly, like connecting a UHV transfer device to transfer samples between different set-ups in UHV conditions for example. Secondly, there is the main chamber, where the samples are prepared and characterized by various means. The vacuum in the chamber is between the low 10^{-10} and 10^{-11} mbar, compared to the low 10^{-9} mbar inside the modutrack. This is achieved by having a smaller volume to pump with a two-stage turbo pump, an ionic pump and a titanium sublimation pump. Inside, the sample mounted on a molybdenum sample holder can be

heated with an oven that can bring it above 700°C by radiation and above 1400°C by electron bombardment. A pyrometer is placed outside the chamber to measure the temperature of the sample through a sapphire window. An ion gun and a leak valve to introduce the argon gas used by the gun or other species like oxygen to remove carbon from a sample at high temperature are also mounted on the chamber. To follow the preparation of a sample and characterize it while there is no x-ray beam, the chamber possesses a RHEED setup (reflection high energy electron diffraction), used to assess the quality of the sample surface for example, and an Auger spectrometer used to determine what species are on the surface of the sample. Finally, various sources can be mounted on the chamber depending on the experiment, like electron bombardment cells for refractory metals such as platinum or crucible cells for gold for example. They can be calibrated using a quartz balance that can be positioned in place of the sample.

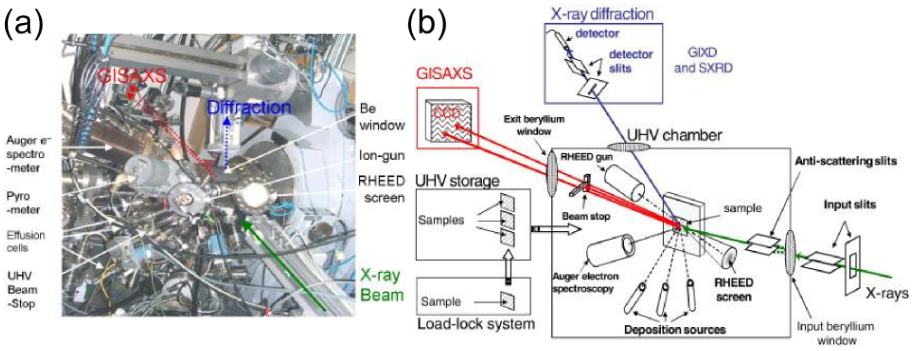

Figure 3.8: (a) Picture of the BM32 UHV chamber, showing the different parts mounted on it and the path of the x-ray beam in green, in red the path of the scattered beam observed in GISAXS and in blue the path of the beam observed in SXRD. (b) Sketch of the BM32 set-up, with the same colour code as (a) for the beam paths.

One specificity of this chamber compared to standard ones is that it possesses two beryllium windows to let the x-rays enter and exit the chamber, Being a very light material with few electrons and UHV compatible, Be allows x-rays to pass with minimum scattering and absorption, thus limiting the background noise during measurements. To further reduce the noise from the Be windows anti-

scattering slits are positioned in UHV after the entry Be window. In addition, a tungsten beam-stop is also placed in UHV after the sample to trap the direct and specular beam insides, thus preventing background from the exit Be window.

3.5.4 The z-axis diffractometer

The UHV chamber is coupled to a z-axis diffractometer[Brennan & Eisenberger, 1984, Fuoss & Robinson, 1984, Bloch, 1985] for the x-ray diffraction measurements, sketched in Fig. 3.5.4. The sample is mounted on it and can be moved on a xyz table to adjust its position with the incoming beam and place it in the homocentre of all the rotations. In addition, two cradles, χ_1 and χ_2, are used to adjust the surface and make it perpendicular with the z-axis. The sample can be rotated around the z-axis thanks to the ω-rotation, which is a complete 360° one. Moreover, the detector can be moved around the sample with two rotations, δ around the z-axis defining the projection of the Bragg angle 2θ and β is the exiting angle of the scattered beam. Finally, α is the rotation of the whole set-up around the x-axis, thus being the angle of the incident beam.

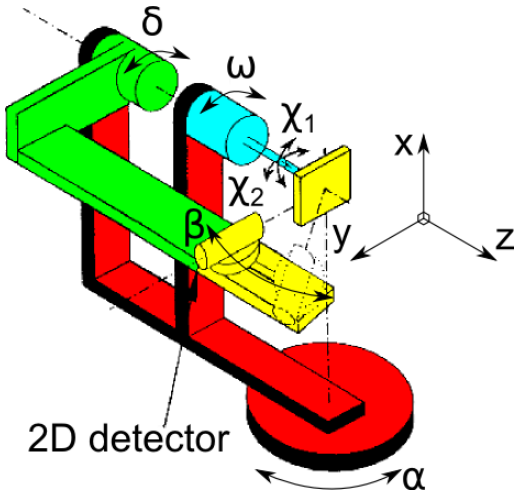

Figure 3.9: Sketch of the z-axis diffractometer of BM32. The sample is placed on the yellow xyz table which has the two cradles χ_1 and χ_2 behind it. The rotation of the sample around the z-axis, ω, is shown in cyan and the rotation of the detector around it, δ, in light green. The detector, at the end of the arm in yellow, has a rotation β. Everything is mounted on the α rotation, in red.

3.5.5 The 2D detector

A new generation of fast 2D detectors have been developed in recent years, with the detection part is composed of several chips. The measurement methods with a 2D detector and the processing of the data has been developed first at the Swiss Light Source [Hu¨lsen, 2004, Schlepütz *et al.* , 2005, Leake *et al.* , 2014] and has been used on various studies, including epitaxial graphene on Ru(0001) [Martoccia *et al.* , 2010] during D. Martoccia thesis in P.R. Willmott group.

The detection system is the 2D detector called Maxipix, developed at the ESRF, shown in Fig. 3.5.5 (a). Each chip has 256×256 photon-counting pixels and the pixel size is 55 μm. The BM32 Maxipix has 5×1 chip, making it a 1296×256 pixel detector, a few pixels are added between the chips to prevent any loss of information, and thus making the detection surface 7.04×1.408 cm^2. Having a 2D detector means that a 2D cut of the reciprocal space is measured at once, which allows better measurements but also adds complexity as we will see in a later paragraph. A typical measurement of a Bragg peak, here an iridium one, is shown in (b) of Fig. 3.5.5.

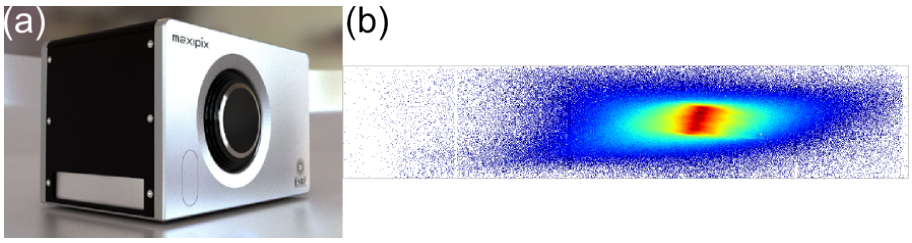

Figure 3.10: (a) Picture of the Maxipix detector. (b) An iridium Bragg peak measured with the 5×1 Maxipix.

3.6 2D detector, reciprocal space and measurements

As we have seen previously, a 2D detector is used to measure the CTRs and rods. A new method of measurement and treatment of the data has been

developed alongside the new detection system and is explained in details in Ref. [Drnec *et al.* , 2014]. The main aspects will be presented here.

3.6.1 Measurements with a 2D detector

When using a 1D detector, measuring the intensity of a CTR or a rod is done by a succession of rocking scans along it at different l-values. The use of a 2D detector can replace the rocking scans, as the 2D detector measures the whole intensity of a cut in the rod at a given l, thus a whole rod can be measured by one scan along l instead of several rocking scans. Measuring a rod then takes less time.

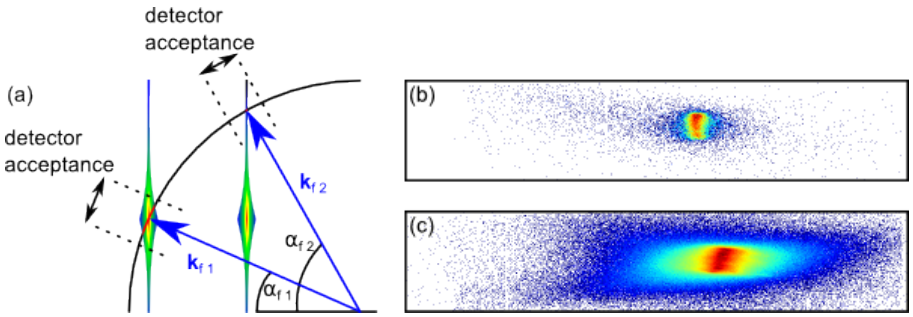

Figure 3.11: (a) Sketch of the geometry of measurement during a stationary scan, at two different l-values, showing the interception of the CTR with the Ewald sphere in black and what is observed with the detector and its acceptance. (b) Ir CTR on the detector far from the Bragg peak. (c) Ir CTR on the detector at the Bragg peak.

Measuring an iridium CTR takes less time than measuring a graphene rod for example. This is due to the combination of the atomic factor and the quantity involved, only a monolayer of light atoms, carbon, compared to a substrate of heavy atoms, iridium. Typically on BM32, a counting time of 1 second is amply sufficient to observe a well-defined cut of an Ir(111) CTR, like (b) or (c) of Fig. 3.6.1, but a counting time of 5 seconds is barely sufficient (50 seconds would be better) to get a graphene rod above the background measured by the detector far away from the origin of the reciprocal space, out of the hk-plane. Consequently, the moiré rods are also difficult to measure out of the plane. However, when the

moiré pattern is decorated by nanoparticles, it enhances the number of photons scattered by it in addition to modulating the rod along l.

3.6.2 Treatment and correction of the 2D data

The intensity of the rod has to be extracted from the 2D peak measured by the Maxipix. PyRod, a specifically developed Python program, has been written by Tao Zhou, another PhD student working on BM32. It has been inspired and takes features from the ROD program developed by E. Vlieg to refine surface structures from x-ray data [Vlieg, 2000]. It is able to read the 2D data and correlate each pixel of the detector with its coordinates in the reciprocal space.

Before proceeding to the extraction of the integrated intensity, one has to correct errors coming from the detector. Various corrections have to be applied on the images themselves due to others effects seen on the detector, as shown in Fig. 3.6.2. Several pixels of the detector are not functioning properly and record a very high non-real intensity, thus they are called hot pixels. There are two types, the first are static and their signal removed easily as their positions are known on the detector. However the seconds are dynamic, meaning that they send a wrong signal only when a photon hit them or an adjacent pixel. They can be corrected by removing all pixels beyond a user defined threshold, this is typically done on a measurement of a low intensity rod such as a moiré one. Occasional effects can also render one or several pictures during a scan difficult to process. As shown in Fig. 3.6.2, high-energy cosmic rays passing through the detector leave a trace, that can be troublesome if it happens in the middle of the region where the peak is located, in particular if it is a cut of a graphene or moiré rod. The various slits before and after the sample ensure that only the sample is illuminated by the beam, however a scratch on the surface or a pollution in the path of the beam can generate a powder diffraction signal or peaks on the detector. When this happens, only the images where these contaminations are far away from the peak studied can be kept.

The extraction of the data is then proceeded with a routine. First a rect-

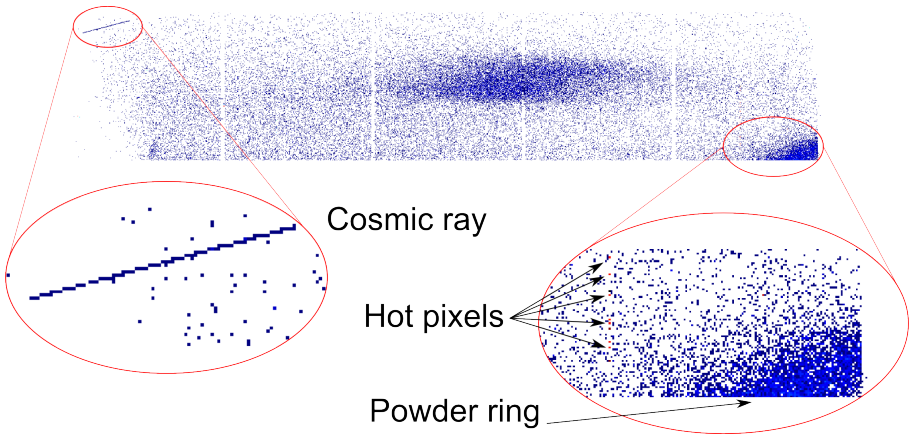

Figure 3.12: Cut of a graphene rod in the middle of the 2D detector at a low l value. Highlighted from the top left is the trace of a cosmic ray passing through the detector. On the bottom right, hot pixels are shown with black arrows and part of a powder ring is in the corner.

angular region of interest (ROI) has to be defined by the user on the image encompassing the measured peak. Then an algorithm is run to search the peak position and boundaries, as shown in Fig. 3.6.2, and evaluates the background around the peak and remove it from it, so that it can determine the integrated intensity at this position. Moreover it also calculates the statistical error on this point. This operation has to be repeated for each image of the scan, corresponding to an l-value of the rod.

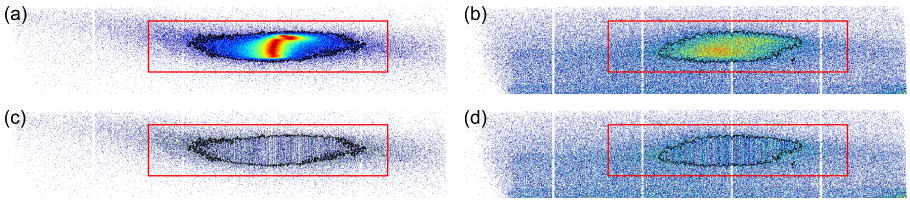

Figure 3.13: In the 2D detector pictures shown here, the ROIs are highlighted in red and the boundaries of the peak in black. (a) Cut of an iridium CTR away from a Bragg peak, after the peak has been determined. (b) Cut of a graphene rod at $l = 1.5$, after the peak search. (c) Same data than (a), showing how the background under the peak is evaluated before being subtracted. (d) Idem as (c) with the graphene rod shown in (b).

Then the structure factors are calculated by taking into account corrections

that are discussed in Ref. [Vlieg, 1997]. However, the integrated intensity measured in a stationary scan $I_{int,stat}$ has to be corrected by various experimental factors to obtain the structure factors $|F_{hkl}|$, as the expression linking the two for stationary scans is :

$$I_{int,stat} = (\Phi_0 T r_e^2 A_0 \lambda^2 / A_u^2)|F_{hkl}|^2 P L_s C_{area} C_{det,s} C_{beam} \tag{3.22}$$

with Φ_0 the incident flux in photons.s^{-1}.mm^{-2}, T the counting time, r_e the classical electron radius, $A_0 C_{area}$ the active area defined on the sample by the slits before and after the sample and the angle of the exiting beam, λ the wavelength, A_u the area of the unit cell, P the polarization factor, L_s the Lorentz factor which depends on the in-plane scattering angle δ and on the exiting angle, $C_{det,s}$ the correction factor of the detector acceptance in a stationary scan and C_{beam} the beam footprint correction factor.

This highlights a few issues that have to be assessed during the experiments. The active area, $A_{active} = A_0 C_{area}$, is defined on the sample as the illuminated area and changes depending on the detector angle δ, with $A_0 = s_1 s_2$ and $C_{area} = 1/\sin\delta$. However, this is false under a certain value of δ, as the area becomes limited by the sample size and not the slits. In our case, with a circular surface of 10 mm, an entry slits opening of 300 μm and detector slits opening of 3.5mm, the critical value of δ is 14.6°. No measurements were performed below $\delta = 27°$ during our studies but this could be an issue in other systems or at smaller wavelengths when the reciprocal space is contracted by comparison. In addition, the shape of the sample can also have an effect, as the illuminated area of a non-circular sample changes with its orientation ω. Another issue is the angular acceptance of the detector, as a too small acceptance with a broad rod would lead to partial measurement of the rod. This is a problem at low l-values, shown in Fig. 3.6.2, as the intersection with the rod is wide is these regions. Regular rocking scans can be performed at low l-values to obtain the information in the lower part of the rods. Thus, in the stationary scan configuration, the detector

slits are set with a large opening, 3.5 mm typically, and the width of the various rods and CTRs is measured in the hk at l=0 prior to the stationary scans to assess the feasibility of the measurements.

Moreover, others corrections have to be applied on the data before it can be used. There is refraction effect, occurring as the beam enters inside the sample even in the condition of total reflection as seen at the beginning of this Section. This has to be corrected as it leads to a shift in the l-value, thus changing the shape of the rods. This is discussed in details in Ref. [Vlieg, 2012] and the conclusion is that the real l value is defined as

$$l = \frac{c}{\lambda}(\sin\alpha_i^{'} + \sin\alpha_f^{'}) \tag{3.23}$$

with c the norm of the unit cell vector perpendicular to the surface, $\alpha_i^{'}$ and $\alpha_f^{'}$ the corrected incident and outgoing angles of the refracted beam, according to :

$$|\alpha_j^{'}|^2 = \sqrt{(\alpha_j^2 - \alpha_c^2)^2 - 4\beta^2} \tag{3.24}$$

with $j \in [i, f]$, α_c the critical angle below which the total reflection occurs, 0.21° for iridium with $\lambda = 1.12$Å, and β the absorption coefficient depending of the wavelength and material. Typically for iridium CTRs with a wavelength of 1.127 Å (11 keV), it modifies l between 0.013 to 0.016 between $l = 0.4$ and $l = 3$. This is the correction due to the refraction inside the iridium, but the beam also passes through the graphene, however the refraction effect from a carbon monolayer at this energy is negligible.

Once the structure factors are extracted from the 2D data, the uncertainty associated with each point has to be evaluated. The total uncertainty $\sigma_{j,tot}$ at a j point of the measurement can be separated in two different errors as discussed in Ref. [Drnec *et al.* , 2014], the statistical error and agreement factor ε :

$$\sigma_{j,tot} = (\sigma_{stat}^2 + \varepsilon^2\langle F_j\rangle^2)^{1/2} \tag{3.25}$$

The statistical error σ_{stat}, which comes from both the peak and the background, is defined as

$$\sigma_{stat} = \sqrt{I_{i,S} + \frac{N_{i,S}}{N_{i,B}} I_{i,B}} \tag{3.26}$$

with $I_{i,S}$ the integrated intensity in the peak, $N_{i,S}$ the area of the peak in pixels, $N_{i,B}$ the area used to estimate the background and $I_{i,B}$ the integrated intensity of the background in its specific area. The agreement factor is defined as

$$\varepsilon = \frac{1}{N} \sum_{F_j} \frac{\sigma_{j,var}}{\langle F_j \rangle} \tag{3.27}$$

and is calculated from strong equivalent reflections, such as a (1 0 l) and a (-1 1 l) CTRs, with $\sigma_{j,var}$ the relative variance of the two equivalent reflections and $\langle F_j \rangle$ the weighted average value of the structures factors, and is propagated over the whole set of data with $\sigma_{j,tot}$.

3.6.3 Modelling the system and fitting the extracted data

Once a full set of CTRs and rods has been measured, extracted and corrected, a kinematic model has to be defined to quantitatively characterize the structure studied during the experiment. The model is made of the crystallographic unit cell of the studied system, with its lengths and angles. Examples will be shown in latter Sections as the corrugation of the graphene on iridium and the structure of nanoparticles grown on top will be discussed. In general, a model is composed of a list of the atoms including their nature, their x, y, z position inside the unit cell and respective displacements along these directions. In addition, the occupancy of each atom, when considering a non complete atomic layer at the top for example, and the Debye-Waller displacements in-plane and out-of-plane. The model is separated in two parts defined by the z position of the atoms. The atoms in the bulk have no displacements and a full occupancy. The variables applied to the surface atoms can then be adjusted so that the simulated signal from the kinematic model fits the measured data. A few variables are common

for every model, a scaling factor or Debye-Waller displacements for example. The roughness of the sample surface is also simulated and is determined using a parameter named β, between 0 and 1, 1 being a full layer [Robinson, 1986]. This parameter describes the occupancy of possible non complete layers on top of the surface, the first one having an occupancy of β, the second one β^2 and so on. Displacements along the different directions are also a variable, however they have to respect the symmetry of the lattice. A displacement can be defined simply as the same linear movement for every atoms in an atomic layer, like a relaxation of the surface layers along z, or can be as complex as a function of the atomic position as long as the function respect the symmetry. This will be discussed later in chapter 5. The refinement of the parameters of the model is achieved with the help of a least squares fit of the simulation to the data.

3.7 Conclusion

To conclude, this chapter has introduced several elements about diffraction and experimental considerations. Some parts will be detailed in later chapters with examples, such as the corrugation of the graphene on Ir(111). To go further into details about surface diffraction, the existing bibliography is very rich and diverse such as books like Elements of Modern X-Ray Physics[Als-Nielsen & McMorrow, 2001], book chapters Nanostructures Observed by Surface Sensitive X-Ray Scattering and Highly Focused Beams [Agostini & Lamberti, 2011] and X-ray diffraction from surfaces and interfaces [Vlieg, 2012] or review papers[Robinson & Tweet, 1992] to highlight a few examples.

Chapter 4

Structural variation and strain in epitaxial graphene on Ir(111)

4.1 Introduction

We have touched on the debate of the commensurability of the graphene grown on Ru(0001) and that in fact it could be possible for multiple structures to be observed due to different growth conditions, in particular the various growth temperatures. Moreover, we have discussed that graphene on Ir(111) was reported to be incommensurate but a high resolution study showed that the structure is more complex, a combination of commensurate domains with incommensurate ones [Blanc *et al.* , 2012]. By varying the growth parameters, in particular the temperature, on can wonder if it is possible to obtain one specific commensurability in particular. In this chapter, some results already published in Ref. [Blanc *et al.* , 2013] and [Jean *et al.* , 2013] will be presented. First, the *in operando* study using electron diffraction of graphene structure evolution during the CVD process will be presented. Then, the results of an x-

ray diffraction study of the structure of graphene on Ir(111) under a temperature sweep will be discussed.

4.2 Experimental methods and environment

Both experiments were performed in ultra-high vacuum (UHV) chambers, which are coupled with Z-axis diffractometers. The reflection high-energy electron diffraction (RHEED) with a grazing incidence was performed exclusively in the BM32 UHV chamber and the synchrotron X-ray diffraction measurements were performed in the UHV chambers of the ID03 and BM32 beam-lines. The base pressure of the chambers was below 10^{-9} mbar. The RHEED patterns were recorded with a CCD camera in front of the fluorescent screen, the electron energy was 10 keV, corresponding to a wavelength of 7.51 Å. The grazing incidence X-ray diffraction (GIXD) measurements were conducted with monochromatic photon beams of 11 and 21 keV, or wavelength of 1.127 and 0.59 Å, with the incident angles, 0.21° and 0.19°, respectively well below the critical angle for total external reflection, in order to keep the bulk background scattering as small as possible. The beam was focused to a size of 35 × 80 μm^2 (full width at half maximum in horizontal and vertical directions, respectively) at ID03 and 300 × 200 μm^2 at BM32. In both cases, a 2D pixel detector (Maxipix) was positioned 570 mm (ID03) and 640 mm (BM32) away from the sample, and detector slits were placed before the detector, 200 mm away from the sample, and opened at 0.5 mm parallel to the sample surface. The reciprocal space scans of the scattered intensity presented below are all normalized to the intensity measured with a monitor placed before the sample.

For both studies, the same Ir single-crystal was used. It was cut and polished on a (111) surface termination to within 0.1° and was bought from "Surface Preparation Laboratory". It was cleaned by cycling ion bombardment and high temperature annealing (1573 K). The bombardments were performed at room temperature with 1.3 kV Ar^+ ions for about 1 hour. Oxygen at a partial pressure

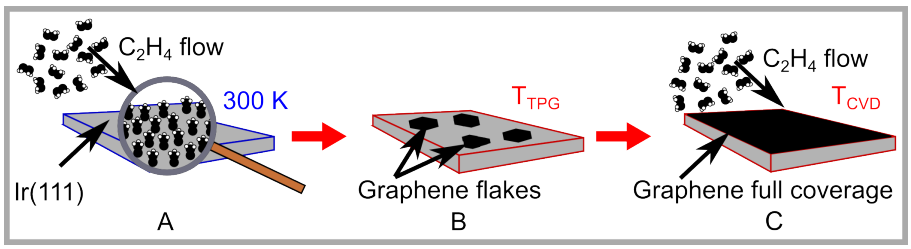

Figure 4.1: Sketch of the different steps of the TPG (A and B) + CVD (C) growth. The first step (A) is the adsorption of ethylene on the Ir(111) surface and its dehydrogenation as ethylidyne (-C_2H_3) at room temperature. The second (B) is a flash at T_{TPG} without ethylene flow inside the chamber resulting in the growth of graphene flakes. The graphene coverage at the end of this stage is 20/25%. The last step of the growth (C) is the completion of the graphene monolayer by CVD, with an ethylene flow and the sample at T_{CVD}. The coverage at the end is $>$ 99%.

of 5×10^{-7} mbar was introduced in the chamber for several 10 minutes at 1273-1373 K in order to deplete the bulk crystal from residual carbon and to achieve a clean surface. Between 450 and 750 K, the sample temperature was measured with a pyrometer with an uncertainty of 50 K. A second pyrometer was used between 750 and 1600 K, with the same uncertainty.

Between 10 and 300 K, the temperature was measured with a platinum thermocouple welded on a helium-cooled copper finger in contact with the sample holder. The sample was heated by electron bombardment on its backside. Ten minutes were needed in order to achieve thermal stabilization after each temperature change for the second study.

The growth processes were performed with ethylene as the carbon precursor in the UHV chambers. The two CVD growth of the RHEED study were done at two different temperatures, 1123 and 1223 K. For the x-ray diffraction study, the graphene growths were done in two steps, using a temperature programmed growth step followed by CVD to complete the graphene layer, more details on the parameters are given in the dedicated section as they are varied and relevant to the results.

As a reminder from the previous chapter, the length of the Ir surface lattice parameter at room temperature is $a^S_{Ir} = b^S_{Ir} = 2.7147$ Å [Arblaster, 2010] and

will be referred to as a_{Ir}. In addition, the unit cell vectors of graphene, $\mathbf{a_{Gr}}$ and $\mathbf{b_{Gr}}$, have a room temperature modulus, calculated for an isolated layer, of a_{Gr} = b_{Gr} = 2.456 Å [Zakharchenko *et al.* , 2009]. The moiré-like superstructure typical of the graphene on iridium system also has distinctive peaks in RHEED and GIXD, however they are not presented here because they are not relevant to the focus of this section. As discussed previously, commensurate phase between graphene and Ir(111) can be indexed by one vector of the unit cell of its coincidence lattice, *i.e.* by two pairs of integers $(m,n)_{Ir}$ and $(p,q)_{Gr}$, such that $m \times \mathbf{a^S_{Ir}} + n \times \mathbf{b^S_{Ir}} = p \times \mathbf{a_{Gr}} + q \times \mathbf{b_{Gr}}$. This relationship may be fulfilled at the expense of strains in graphene.

4.3 *Operando* study of graphene grown by CVD

A typical RHEED pattern taken on the fluorescent screen is shown in Fig. 4.2 (b). The streaks are the iridium CTRs and graphene and moiré rods, coming from the surface. Two groups of streaks are visible on each side of the specularly reflected beam, as the reciprocal space screened is on each side of its origin, the specular reflection is in the middle.

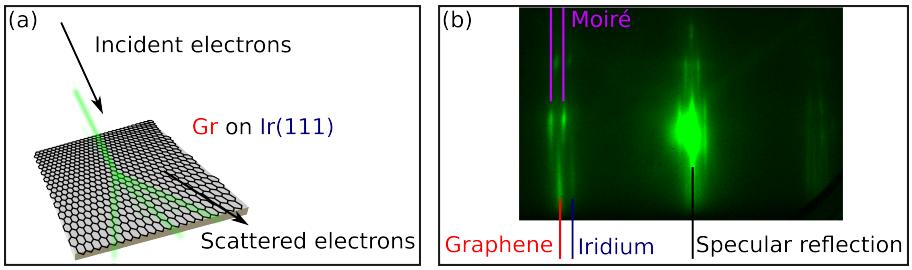

Figure 4.2: (a) Sketch of the graphene on Ir(111) with the incident and scattered electron beams. (b) RHEED pattern of a full graphene layer on Ir(111) at room temperature, with the specular reflection in the middle and marked in black, on the left, the graphene streak in red, the iridium one in blue and two of the moiré in purple.

The density of nucleation was determined using *ex situ* atomic force microscopy (AFM) under ambient conditions, one of the several topographs is

shown in Fig. 4.3. The density for the 1123 K growth was determined to be 9×10^{-2} μm^{-2}. The determination of graphene coverage based on a set of AFM images allowed one to calibrate the ethylene dose, the coverage increases with dose following a modified Langmuir model without any free parameter [Coraux *et al.* , 2009]. In Fig. 4.3(d), the average determined coverage of the sample, 24% $\pm$ 5%, allows to deduce the ethylene dose by using this model. From the average graphene island density, the average island radius is estimated to be 1 μm for the sample grown at 1123 K, assuming evenly sized, diskshaped islands.

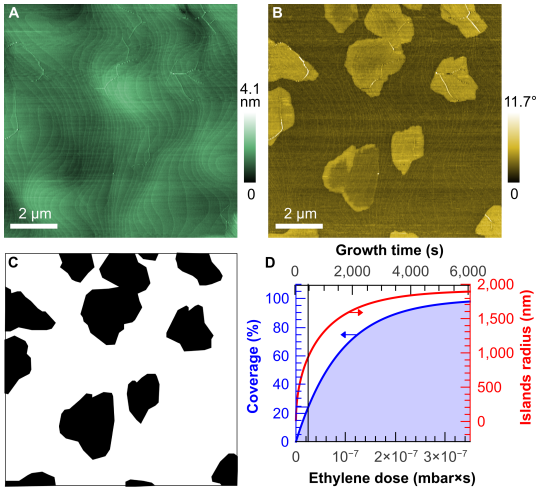

Figure 4.3: (a) AFM topograph of graphene islands grown by CVD at 1123 K, done *ex situ* in atmospheric conditions. (b) Phase image of (a), highlighting the graphene islands. (c) Representation of the graphene islands in black and iridium surface in white to assess the graphene coverage. (d) Graphene coverage (left) and average island radius (right) as a function of ethylene dose (bottom) as it is only a CVD process, there is no TPG here, and growth duration (top), the vertical dashed line corresponds to the AFM topograph.

The distance between Ir and graphene peaks was measured as a function of ethylene dose. The distance between the Ir streaks served as a calibration to determine the lattice parameters, as it remains constant during the growth. The evolution of the iridium lattice parameter with temperature has been tabulated in Ref. [Arblaster, 2010]. Figure 4.4 shows an overall decrease of about 1.6% of graphene lattice parameter, a_{Gr} , during the full growth, the graph here only

shows their evolution to their final stable values reached around 50% coverage. For both CVD growths, a_{Gr} starts around 2.51 Å at coverages of 15% for the 1123 K growth and 20% for the 1223 K one. Graphene streaks are difficult to set apart from the background due to the low signal/noise ratio caused by the high temperatures and low quantity of materials on the surface. The final values of a_{Gr} are 2.4705 ± 0.0020 Å at 1123 K and 2.4723 ± 0.0020 Å at 1223 K, they are reached for graphene coverages above 50%. By comparison with the calculated values for freestanding graphene, its shows that the graphene on Ir(111) is extensively strained by 0.6%–0.7% [Zakharchenko *et al.* , 2009].

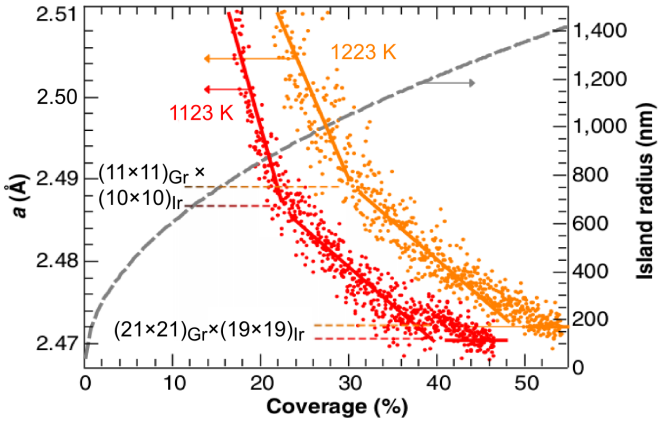

Figure 4.4: Evolution of the graphene lattice parameter, a_{Gr}, during both CVD growth (left), 1123 K in red and 1223 K in orange, and graphene island radius in dashed grey (right) as a function of the graphene coverage. Both a_{Gr} evolution show two changes of slope, highlighted with dashed lines, corresponding to different commensurabilities, $(11 \times 11)_{Gr} = (10 \times 10)_{Ir}$ then $(21 \times 21)_{Gr} = (19 \times 19)_{Ir}$.

The decrease of a_{Gr} for both growths is not constant, two salient points can be observed on both evolutions, the first one at 23% and 31% coverage for 1123 K and 1223 K, respectively, and the second one at 40% and 49%, respectively. These points can be attributed to surface phase transitions. Indeed, the first salient point, at $a_{Gr} = 2.487$ and 2.489 Å respectively, corresponds to a commensurate phase where 11 a_{Gr} are equal to 10 a_{Ir}, $(11 \times 11)_{Gr} = (10 \times 10)_{Ir}$, which is a first-order commensurability. The second salient point,

where a_{Gr} become constant for the rest of the growth, corresponds to 21 a_{Gr} equal to 19 a_{Ir}, $(21 \times 21)_{Gr} = (19 \times 19)_{Ir}$, a second order commensurability, similar to that $(25 \times 25)_{Gr} = (23 \times 23)_{Ru}$ observed for graphene on Ru(0001) [Martoccia *et al.* , 2008]. The changes of the slope of a_{Gr} shows a tendency for the graphene to adapt to a commensurate phase, to possibly maximize the interaction with the iridium substrate. It is energetically more stable.

Several mechanisms could be responsible for the decrease of a_{Gr} with graphene coverage. Small graphene islands have proven to be strained by their edges interacting with the substrate, this interaction decreasing with the growing islands [Lacovig *et al.* , 2009]. However, due to the large size of the islands ($>$ 100 nm), no significant increase in a_{Gr} can be expected from stress relief at the island edges [Massies & Grandjean, 1993]. Another solution could come from the coalescence of neighboring islands, with different coincidences on Ir(111), but that would result in accommodating one substrate interatomic distance over the distance between island nucleation centers 1 μm, *i.e.*, a negligible 0.03% strain.

The solution resides with the numerous vacancies of various sizes that are trapped inside graphene at the growth front. At a 30% coverage, their density is several 0.1 nm^{-2} [Coraux *et al.* , 2009], and a_{Gr} is several 0.1% larger than the value at the end of growth. DFT calculations, presented in the supplementary materials of Ref. [Blanc *et al.* , 2013], for a defect density of 0.2 nm^{-2} reveal that single, di-, and tetravacancies in graphene/Ir(111) are surrounded by a tensile strain field, from a few to several 0.1% depending on the configuration, usually longer ranged for larger vacancies (unless their location allows a close-to-perfect match between the positions of C dangling bonds and Ir atoms). These values are different from those expected in freestanding graphene [Krasheninnikov & Nieminen, 2011] due to the strong interaction between C and metal atoms at vacancy edges [Ugeda *et al.* , 2011]. Even though this interaction reduces the formation energies of vacancies [Wang *et al.* , 2013], their migration barriers are high (3–8 eV, depending on the position in the moire pattern and the size of the vacancy), so that the agglomeration of vacancies,

a situation reported to be energetically favourable for other types of defects in graphene [Nguyen *et al.* , 2012], is hindered, especially for large defects like tetravacancies.

Therefore, the slopes of a_{Gr} with the coverage change with temperature is a tradeoff between vacancy diffusion, healing, and incorporation at edges. The progressive filling of vacancies during growth and the thermally activated diffusion of small vacancies that are annihilated upon reaching the edges of graphene are expected to decrease tensile strains and thus to account for the decrease of a_{Gr}. Because of the short lifetime of ethylene on graphene at the growth temperature, the filling of the vacancies must be less and less efficient as their size decreases, which agrees with the slower decrease in a_{Gr} at larger doses. Moreover, the first salient point corresponds also to the start of coalescence for graphene islands [Coraux *et al.* , 2009], thus decreasing the free-edges length where defects can diffuse to and be healed, thus decreasing the rate of that process.

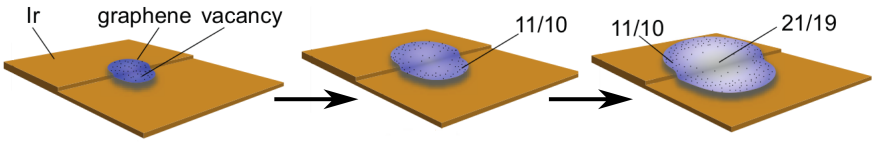

Figure 4.5: Sketch of the evolution of a graphene island with time during the growth, with the graphene in shades of blue to highlight the evolution of a_{Gr}, defect as black points and the iridium substrate in orange. The apparition of the two commensurabilities are indicated.

This implies, before the salient points, the coexistence of commensurate and incommensurate phases, as sketched in Fig. 4.5. At the beginning of the growth, the small graphene island is totally incommensurate. However, at the first salient point corresponding to the second sketch of Fig. 4.5, the $(11 \times 11)_{Gr}$ $= (10 \times 10)_{Ir}$ commensurate phase emerges as the density of defects decreases. The growth continues and then leads to the last sketch, corresponding to the second salient point, where the $(11 \times 11)_{Gr} = (10 \times 10)_{Ir}$ phase shifts to an incommensurate one and then to the $(21 \times 21)_{Gr} \times = (19 \times 19)_{Ir}$ one as the

islands grows and defects are removed during the growth process.

This *operando* study of the CVD process indicates that graphene on Ir(111) has a tendency to form commensurate phases and even to shift between them, confirming the possible coexistence of commensurate and incommensurate domains as stated in Ref. [Blanc *et al.* , 2012]. One can wonder if it is possible to play with the strain inside a full grown graphene layer, either to match a commensurate phase or to shift to another. Scanning the temperature and accommodating others defects, *i.e.* the wrinkles, is a possible way to achieve this.

4.4 Switching between commensurabilities with temperature

The effects of temperature on graphite has been known for a long time, in particular its negative thermal expansion coefficient (TEC) below 500 K [Nelson & Riley, 1945, Mounet & Marzari, 2005]. Graphene, a single layer of graphite, has been predicted to exhibit negative TEC as well, below 300 K, with a unique dependence of its lattice parameter with temperature due to the out-of-plane vibration modes which its membrane-like topography allows [Mounet & Marzari, 2005, Zakharchenko *et al.* , 2009]. This prediction was tested on both suspended graphene, in electromechanical resonators [Singh *et al.* , 2010], and on supported graphene, for graphene exfoliated from graphite and transferred to SiO_2/Si [Yoon *et al.* , 2011]. The loose contact between graphene and SiO_2 [Geringer *et al.* , 2009] presumably explains why graphene does not follow the TEC of the support. Which TEC graphene exhibits under the influence of a support with which it forms a good contact is of fundamental interest and an open question in any future application operating at variable temperature. The answer to this question is indeed, as we shall see, related to the formation of defects and strain, which are both known to modify the properties of graphene [Neto *et al.* , 2009].

Graphene grown on a metallic substrate is well-suited to address this is-

sue. Depending on the strength of the graphene-metal interaction, various situations have been reported as we have discussed in a previous chapter. In graphene on Ru(0001), a prototypical system for a strong interaction (characterized by hybridizations between the metal and graphene electronic bands and charge transfers of the order of 1 eV), the TEC of graphene remains unknown. However a compressive strain larger than 1% was found at room temperature [Martoccia *et al.* , 2008], presumably resulting from the compression of the carbon lattice when cooling down from the growth temperature at which graphene locks in a commensurate phase on the Ru(0001) lattice. Graphene on Ir(111) exhibits contrasting properties, which can be traced back to the weak interaction between graphene and iridium (marginal hybridization of electronic bands between the two materials and typically 100 meV charge transfer [Pletikosić *et al.* , 2009]) : its structure has low strain at room temperature [Blanc *et al.* , 2012], which is ascribed to the partial relief of compressive strain by delaminating graphene, in the form of so-called wrinkles [N'Diaye *et al.* , 2008, Hattab *et al.* , 2012]. We note that this stress relief pathway is forbidden in graphene on Ru(0001) due to the strong C-Ru bonds [Sutter & Albrecht, 2013].

Here, we show that besides forming wrinkles, graphene can develop small rotations allowing it, or part of it in the form of domains, to lock in commensurate phases on Ir, during cool down from the growth temperature. These in-plane rotations about the crystallographic orientation corresponding to zigzag carbon rows aligned to the dense-packed rows of Ir (referred to as R0° in the following) are much smaller than those observed recently [Loginova *et al.* , 2009b, Meng *et al.* , 2012]. We also show that the R0° orientation can be strained to a large extent, thus exploring a broad range of graphene-Ir(111) epitaxy between two different commensurate phases, which are stabilized over wide temperature ranges. We establish that the growth conditions influence the structure of graphene. Finally whatever the preparation procedure, graphene is found to adopt a positive TEC on Ir(111) over the whole range of temperature between 10 and 1300 K.

4.4.1 Specific experimental methods and parameters

Different preparations of graphene were performed following a well-establish method, consisting in a temperature programmed growth (TPG) step followed by chemical vapor deposition (CVD) [N'Diaye *et al.* , 2006], but with different growth temperature in view of unveiling the role of this parameter. The different sample preparation conditions are summarized in Table 4.1. For the two preparations, P1 and P2, graphene was prepared by exposing the surface to ethylene at 10^{-7} mbar at room temperature for 5 minutes, then flashing the temperature (T_{TPG}) for 20 seconds, which is known to yield graphene islands. Then the sample was cooled down by 200 K to T_{CVD} and exposed to an ethylene partial pressure of 10^{-8} mbar for more than 10 minutes (10 minutes of ethylene exposure is known to yield $> 99\%$ coverage of graphene) and kept at the same temperature without ethylene for another 10 minutes.

On both samples, the lattice parameter and relative crystallographic orientation of graphene and Ir(111) were studied by analyzing the scattered intensity in an in-plane cut of the reciprocal space with radial scans along the in-plane component $\mathbf{Q}_r$ of the momentum transfer, and with azimuthal scans along the angle ω, respectively. The intensity is maximal were the crystal truncation rods of Ir(111) and the diffraction rods of graphene intersect the plane (parallel to the sample surface) of reciprocal space under investigation.

4.4.2 Hysteretic behaviour of the graphene lattice parameter with temperature

Figure 4.4.2 shows a_{Gr} as a function of the sample temperature, measured through several experiments on different samples grown under the same condition (P1, to within 50 K of uncertainty on temperature measurements). For these measurements, the samples were cooled down to 10 K step-by-step. They were then heated back up to 1300 K and cooled down again to 10 K before being finally heated back to room temperature. At each temperature, the Ir

lattice parameter was deduced from the (110) and (020) Bragg reflections and is in accordance with the bulk thermal behaviour [Arblaster, 2010]. The first observation is that graphene on Ir has a positive TEC over the whole temperature range, whatever the sample's history. The room temperature lattice parameter of graphene is found to be $a_{Gr} = 2.4535 \pm 0.0008$ Å. The lattice parameter, measured from 10 to 1100 K, displays a hysteresis, very similar to that reported by Hattab *etal.* [Hattab *et al.* , 2012] above room temperature, and characteristic of the formation/removal of wrinkles in graphene. At the end of the growth, at about 1273 K (point A), graphene lies on its substrate without wrinkles. As the temperature is decreased, the graphene lattice parameter first follows the contraction of the Ir lattice (points B to C), leading to the build-up of compressive strain in graphene (relative to free-standing graphene at the same temperature). Wrinkles appear when further straining cost more energy than wrinkling, below 800 K (point C). From 800 K down to room temperature, a_{Gr} remains constant as the wrinkles keep on growing (points C to D). Between 300 and 4 K (points D to E), the variation of the graphene lattice parameter follows that of Ir again, without new wrinkle formation. Graphene and Ir then follow the same behaviour from liquid helium temperature up to 600 K (points E to F). This implies that the wrinkles do not change and graphene expands as much as its substrate. Above 600 K (points F to B), a_{Gr} remains constant while the Ir substrate expands. At that point, the wrinkles begin to flatten and the hysteresis loop closes when the growth temperature is reached. The transitions temperatures of 800 K (decreasing T) and 600 K (increasing T) are close to those (960 K and 650 K) reported in Ref. [Hattab *et al.* , 2012], for samples prepared in similar conditions.

Let us now follow the lattice parameter variations with temperature (Fig. 4.4.2) for the second sample preparation (P2). After preparation at 1373 K (point 1), the system has been cooled down to 300 K (point 2), where $a_{Gr} = 2.4507 \pm 0.0008$ Å. Measurements were first performed during cooling down to 10 K, and next heating back to 300 K (points 2 to 3 and back to 2). The

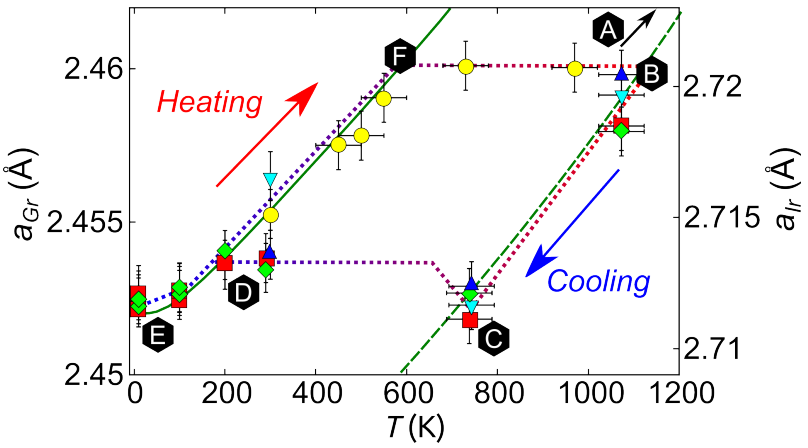

Figure 4.6: Evolution of the graphene lattice parameter a_{Gr} (left axis) of different samples prepared under the same conditions (P1), as a function of temperature (T). Each colour and shape correspond to a different sample (blue upward-pointing triangles, cyan downward-pointing triangles, red squares, light green diamonds and yellow circles). The doted black line shows the shape of the hysteresis observed in Ref. [Hattab *et al.* , 2012]. The solid green curve is the evolution of the bulk Ir lattice parameter (right axis) with temperature. The dashed green curve is the Ir green solid curve reported, as a guide for the eyes, to match the evolution of graphene lattice parameter at high temperature. The arrows and letters in the black hexagons marks specific steps of the thermal history of the samples. The growth is referred as point A and measurements began at lower temperature on point B at 1073 K.

temperature was next increased up to 1350 K (2 to 5) and cooled down back to 10 K (5 to 7). As for P1, the graphene is found to have a positive TEC over the whole temperature range. Most importantly, as for P1, it has the same TEC as the Ir substrate between 3 and 4 and between 5 and 6, during heating and cooling, respectively. In addition, the graphene lattice parameter displays a hysteresis, but which unlike for P1 is not fully closed : the lattice parameter is smaller after the sample has been heated to high temperatures. Indeed, the graphene lattice parameter at room temperature has decreased by 0.13% to a_{Gr} = 2.4474 ± 0.0008 Å. Moreover, the superposition of the hysteresis from Fig. 4.4.2 in doted gray in Fig. 4.4.2 shows that P1 and P2 have different wrinkles nucleation temperatures.

Azimuthal scans close to the (020) reflection, as shown in Fig. 4.4.2, give

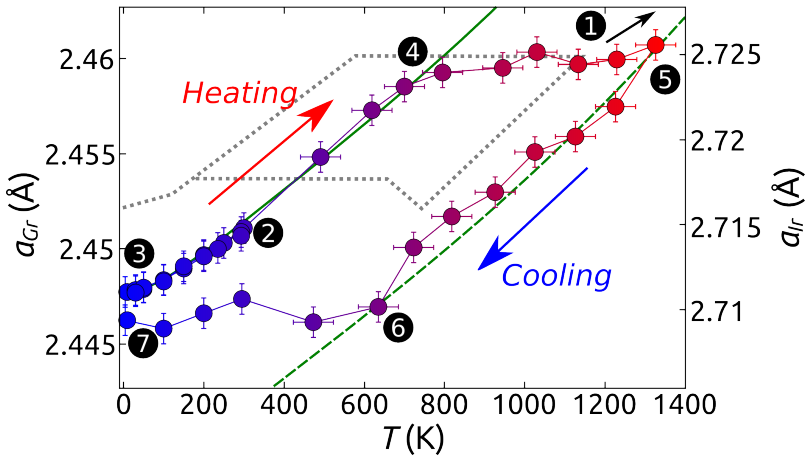

Figure 4.7: Evolution of the graphene lattice parameter a_{Gr} (left axis) for the second sample preparation (P2) as a function of the temperature (T), as deduced from the radial location of the (110) reflection (blue and red circles). The solid green curve is the evolution of the bulk Ir lattice parameter (right axis) with temperature. The dashed green curve is the Ir green solid curve reported as a guide for the eyes to match the evolution of the graphene lattice parameter at high temperature. The arrows and numbers in the black circles marks specific steps of the thermal history of the sample. The growth is referred as point A and measurements began at lower temperature on point B at 300 K. The doted gray lines shows the shape of the hysteresis observed in Ref. [Hattab *et al.* , 2012].

more details about the epitaxial relationship of graphene with its substrate. Besides the peak at 0° corresponding to the contribution of the well-known R0° phase, there are two narrower peaks, distant respectively of -2.42 ± 0.01° and +2.31 ± 0.01° from the central one (at 200 K on the first cool-down, in blue triangles). The fact that these peaks are not equally rotated from 0° is an artifact. The measured intensity is the integration of the scattered signal across the gap of the detector slits, which are inclined with respect to the scattering vector. The measured azimuthal angles are thus the result of a projection, along this inclined direction, of the actual contribution, which corresponds to an azimuthal angle of $\pm(2.42 + 2.31)/2 = \pm 2.365°$. However, we will discuss in the next paragraph that the angle is most probably 2.36°, as it corresponds to a commensurability and the corresponding phase is referred to by the average orientation, as R2.36° hereafter. Radial scans in the inset of Fig. 4.4.2 show

that the R2.36° and R0° phases do not have a maximum at the same $\mathbf{Q}_r$ (here at 200 K), and thus have different lattice parameters. For R2.36° $a_{Gr} = 2.4521 \pm 0.0008$ Å at 200 K, which is 0.08% larger than the lattice parameter of the R0° domain at the same temperature. Moreover, the R2.36° value does not vary with temperature. When heating from 300 K, the intensity of the side peak decrease significantly to become smaller than that of the R0° peak above 795 K, as shown in Fig. 4.4.2. After cooling down to 200 K (cyan downward-pointing triangles), the side peaks have almost vanished, and the intensity of the central peak has decreased by half. Moreover, the full width at half maximum (FWHM) of the side peaks have increased markedly after the heating and cooling cycle, from 0.21 to 0.48°. By contrast, the FWHM of the R0° peak is constant at 0.8° across the whole temperature loop. The intensity corresponding to the rotated domains has almost fully vanished at high temperature, where the first plateau of the hysteresis of the evolution of the graphene lattice parameter with temperature begins.

4.4.3 Shift between different commensurabilities with temperature

As seen in Ref. [Hattab *et al.* , 2012] and for the sample preparation P1, the variation of a_{Gr} with temperature for the R0° phase describes a hysteresis loop. Figure 4.4.3, in which a_{Gr} is normalized to a_{Ir}, shows that, in addition, between the B and C points, and between D and E, when graphene and iridium have the same behavior with temperature, non-rotated, commensurate phases are stabilized. To a very good approximation, a $(10\times10)_{Gr} = (9\times9)_{Ir}$ commensurate phase is found at high temperature between B and C and a $(21\times21)_{Gr} = (19\times19)_{Ir}$ one at low temperature between D and E. The slight deviations from the a_{Gr}/a_{Ir} expected for these phases can be explained as due to the coexistence of a small fraction of incommensurate phases. In Ref. [Blanc *et al.* , 2012], the incommensurate phases were found to dominate over commensurate ones. We interpret this difference as the consequence of different preparation conditions

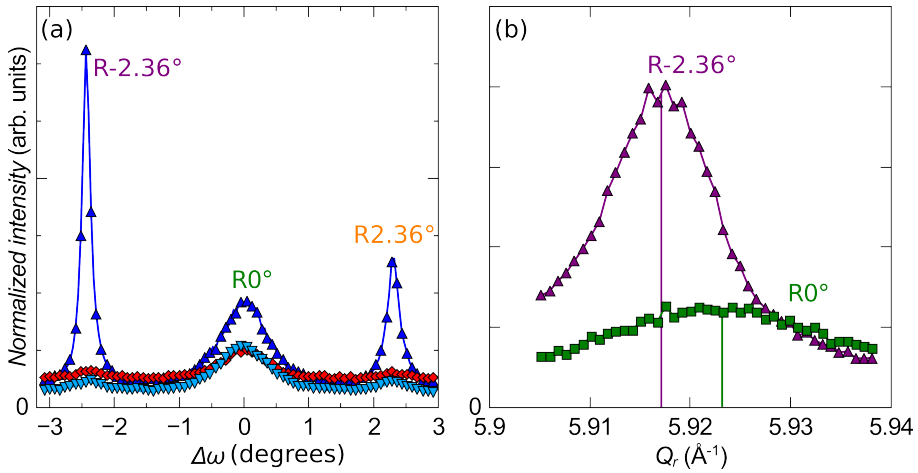

Figure 4.8: Rocking scan of the graphene peaks on the (020) reflection of the first sample at 200 K before (blue upward-pointing triangles) and after (cyan downward-pointing triangles) high temperature annealing, and at 945 K (red diamonds). The left (R-2.36° in purple) and right (R2.36° in orange) peaks on the curves are distant of -2.42° and 2.31° respectively from the central peak (R0° in green) at all temperature (T). Inset: in-plane longitudinal scan of the left peak (R-2.36°) in purple and central peak (R0°) in green from the blue curve in (a) at 200 K. Two lines show the position of the maximum of each peak. The intensities are normalized by the monitor and in linear scale.

: for minimizing its elastic energy, graphene adopts different epitaxial relationships with its substrate at different growth temperatures, and the relief of elastic energy upon cool-down, by wrinkles formation, is only partial, in other words, graphene partly inherits its room temperature lattice from that at growth temperature.

For the sample preparation P2, two rotated phases with small rotations, 2.36° and -2.36°, are present in addition to the non-rotated one. The influence of the growth temperature over the appearance of rotated phases on Ir(111) is a well-known phenomenon [Loginova *et al.* , 2009b, Hattab *et al.* , 2011]. These two rotated phases appear at the highest growth temperature, and are quenched by the relatively fast cool-down to room temperature. However, their disappearance during the heating back to high temperatures shows that they are metastable. The observed irreversible loss of intensity of the R2.36° phase coincides with the temperature range in which wrinkles disappear. This corresponds

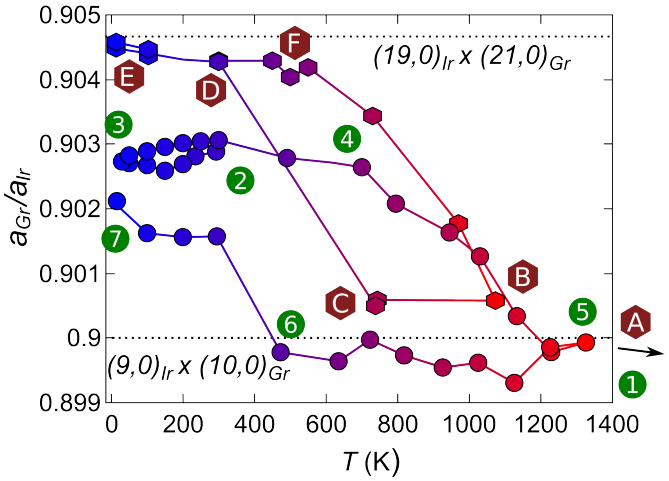

Figure 4.9: Ratio of the graphene and Ir lattice parameters a_{Gr}/a_{Ir} as a function of the temperature (T). The P1 preparation is represented with red and blue diamonds and the P2 one with green and yellow circles. Black doted lines signal commensurate ratios. The letters inside the brown hexagons (P1) and numbers inside the green circles (P2) denote specific steps of the thermal history of the samples.

to a regime where graphene is stretched by its substrate, which could result in the partial conversion of the R2.37° phase into other phases, either characterized by rather small size domains (well below the coherence length of the X-ray beam), having smaller in-plane rotations with respect to the Ir lattice, or the main R0° phase.

The R2.36° phase is a commensurate one. Indeed, Fig. 4.4.3 shows that the R2.36° has a structure which matches a $(11 \times 4)_{Gr} = (10 \times 4)_{Ir}$ commensurate phase. This rotational variant is characterized by a tensile strain (with respect to free-standing graphene) of 2.61% at 200 K, thus the P2 sample probably has incommensurate and commensurate domains in the variant to accommodate this strain. The corresponding moiré has a 2.37 nm periodicity, thus slightly smaller than the usual moiré period of 2.52 ± 0.02 nm measured at the same temperature for the R0° phase. In addition, it can be noted that this commensurate phase is similar to the first one observed in the RHEED study during the growth, albeit rotated, thus making it almost typical of strained graphene

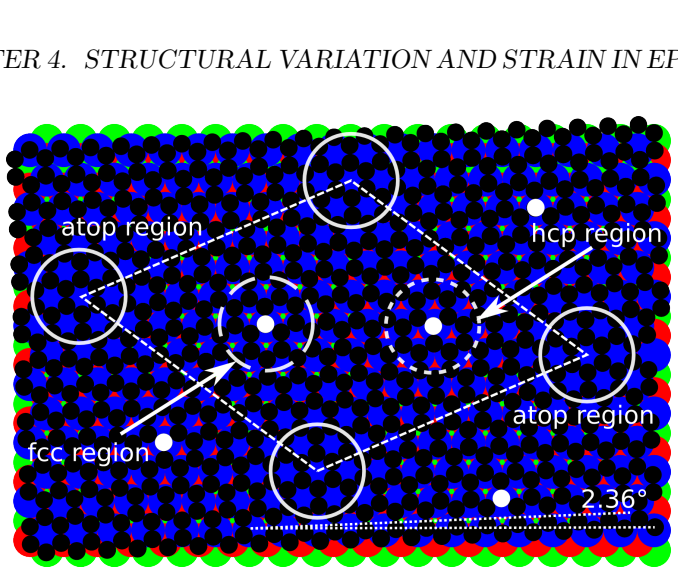

Figure 4.10: Sketch of the graphene on top of Ir(111) with a rotation of 2.36° as shown with the dotted white lines at the bottom (one is aligned with an Ir row and the other with a carbon row). Carbon atoms are shown as black disks, Ir atoms of the first, second, and third top layers are, respectively as blue, red, and green disks. Carbon atoms on top of Ir ones are shown as white disks. The new superlattice is highlighted with the dashed white frame. In the top regions (white circles in the corners of the cell), an Ir atom of the first layer is centered below a graphene hexagon. In the fcc region (dashed circle) and the hcp region (dotted circle), there are threefold-coordinated hollow sites centered under the carbon ring's center: either an fcc site (fcc region) or an hcp site (hcp region).

on Ir(111), either caused by temperature or defects. These rotational domains provide a new perspective on the reason why, for preparation P2, the graphene's TEC follows that of the Ir over a wider temperature range. The R2.36° has a higher density of carbon atoms in coincidence with Ir ones than the $(21 \times 21)_{Gr}$ = $(19 \times 19)_{Ir}$ phase of preparation P1, allowing the system to be heated at higher temperature before wrinkles start to be stretched out (after point 4). This is consistent in a first approximation with the *O*-lattice theory, which states that the phase with the highest density of coincident sites is the most stable [Bollmann & Nissen, 1968], and here despite large strains. At 1300 K, the temperature is beyond the point where all wrinkles are flattened according to Hattab et al. [Hattab *et al.* , 2012]. Like for the P1 preparation, there is in this system a competition between two states of the graphene/Ir system : a fully commensurate state at the cost of creating rotational domains and/or strains,

	T_{TPG}	T_{CVD}	Type of commensurability	Temperature range
P1	1473 K	1273 K	$(21 \times 21)_{Gr} = (19 \times 19)_{Ir}$ (heating) $(10 \times 10)_{Gr} = (9 \times 9)_{Ir}$ (cooling)	4 to 600 K 1073 to 738 K
P2	1573 K	1373 K	$(11 \times 4)_{Gr} = (10 \times 4)_{Ir}$ (heating) $(10 \times 10)_{Gr} = (9 \times 9)_{Ir}$ (cooling)	4 to 800 K 1300 to 473 K

Table 4.1: Temperature of the Temperature Programmed Growth and Chemical Vapour Deposition steps during the graphene growth, types of commensurability detected on the different samples during heating and cooling, and their corresponding temperature range, for the two preparation methods P1 and P2.

and a non-rotated state, for which the strain is better relieved by the graphene being incommensurate and forming/destroying wrinkles.

For the two sample preparations, upon cooling down, the graphene contraction as a function of temperature follows the Ir behaviour from 1300 to 650 K. In this temperature range, the interaction with the substrate, though known to be weak [Pletikosić *et al.* , 2009], is large enough to allow for increasing strain without forming wrinkles to release it. Figure 4.4.3 shows that the graphene here is close to being commensurate with its substrate, in a $(10 \times 10)_{Gr} = (9 \times 9)_{Ir}$ phase. The misfit for this commensurate phase is only 0.34%. Below 650 K, the lattice parameter stabilizes during the wrinkles formation and growth.

As summarized in Table 4.1, the structure of graphene grown on Ir(111) can vary deeply due to changes in the growth procedure. For the first sample preparation (P1), with a growth temperature of 1273 K, graphene presents a hysteresis loop with temperature, being close to commensurate with its substrate at high and low temperature, where it displays an expansion behaviour similar to the substrate over limited temperature ranges, and being incommensurate in the average in between, where wrinkles are present. For the second sample preparation (P2), with a 100 K higher growth temperature, graphene presents different commensurate phases, unrotated and rotated, with the $(10 \times 10)_{Gr} = (9 \times 9)_{Ir}$ and $(11 \times 4)_{Gr} = (10 \times 4)_{Ir}$ commensurabilities respectively. These phases are linked with the broader temperature range where the graphene and the Ir thermal expansion coefficients are identical, during expansion or contrac-

tion. This is further evidence that the commensurability of graphene on Ir can be tailored by the growth process.

4.5 Conclusion

In conclusion, we have observed various commensurate surface phases on graphene on Ir(111), either during CVD growth or on a full grown layer by scanning the temperature. Moreover, these commensurabilities are strongly linked with the presence of defects, atomic or topological. It shifts through a series of commensurate phases with its substrate as the vacancy density varies during the growth and post-growth, presents two competing tendencies with temperature changes : either tending to adopt commensurate phases with its substrate at low and high temperatures, with different commensurabilities depending on the preparation conditions, or forming wrinkles. This shows a strong tendency to commensurability for a system that had been labelled as incommensurate for a long time, and this despite the weak hybridization with the substrate. In addition, the thermal expansion coefficient of graphene grown on Ir(111) remains positive at all temperatures, regardless of the growth preparation. This is true even below room temperature, between 10 and 300 K, where the graphene TEC always follows the Ir one whatever the previous thermal history.

Chapter 5

Topography of the graphene/Ir(111) moiré studied by surface x-ray diffraction

5.1 Introduction

In a previous chapter, we have begun to discuss the interaction between the epitaxial graphene and its substrate. New properties can be induced in graphene through the interaction with the substrate, e.g. electronic bandgaps [Pletikosić *et al.* , 2009], spin-polarization [Varykhalov *et al.* , 2008] and superconductivity [Tonnoir *et al.* , 2013]. In most graphene grown on metal systems, the interaction is modulated at the nanoscale, due to lattice mismatch between graphene and the metal over the moiré superlattice. Knowledge on the topographic properties of these moirés, *i.e.* the average graphene-metal distance, and the perpendicular-to-the-surface amplitude of the graphene and metal un-

dulations across the moiré, is desirable in view of characterizing the interaction and rationalizing the other properties.

However, there are inherent difficulties to measure and quantify these parameters at such small scales. Most efforts that have relied on scanning tunnelling microscopy have faced the issue of the entanglement of the structural and local density of state which is inherent to the tunnelling effect. A striking illustration has been the debate on the amplitude [Marchini *et al.* , 2007, Vazquez de Parga *et al.* , 2008] and sign [Busse *et al.* , 2011, Sun *et al.* , 2011] of the moiré-related undulation in graphene/Ru(0001) and graphene/Ir(111), respectively. It has also been determined that the reactivity of the tip is affecting the observation, changing the local topography [Dedkov & Voloshina, 2014, Altenburg & Berndt, 2014] and this problem can be solved by attaching one molecule such as carbon monoxide to the tip [Dedkov & Voloshina, 2014, Hämäläinen *et al.* , 2013].

Another way to assess this modulation is with scattering techniques, such as low-energy electron diffraction (LEED), surface X-ray diffraction (SXRD), and X-ray standing waves (XSW), which are free of such probe-induced perturbations of the systems. These techniques allows to screen not only the top surface layer, the graphene here, but also the surface layers of the substrate. To the expense of complex calculations in the framework of the dynamical theory of diffraction, LEED was used to assess the topography of graphene/Ru(0001) [Moritz *et al.* , 2010] and graphene/Ir(111) [Hämäläinen *et al.* , 2013]. SXRD was used to analyse the topography of graphene/Ru(0001) [Martoccia *et al.* , 2008], as was done by XSW for graphene/Ir(111) [Busse *et al.* , 2011]. Confirming and refining the results obtained with these approaches is of prime importance in order to set reliable points of reference for first principle calculations. which are cumbersome in essence in such systems due to the importance of non-local (*e.g.* van der Waals) interactions [Mittendorfer *et al.* , 2011]. Density-functional theory (DFT) calculations done on the unit cell of the modulation result in the buckling of the various surface layers but also the electronic density and possible hybridisations [Busse *et al.* , 2011, Tonnoir *et al.* , 2013]. However, these

$ab-initio$ calculations are limited to commensurate moiré superlattices due to the requirement to have a periodic system.

An highlight of the difficulties to study such structural variations is the archetype of the strongest type of interaction of graphene with its substrate, graphene on Ru(0001). Various studies have reported largely different values for the graphene amplitude modulation, from 0.05 Å [Vazquez de Parga *et al.* , 2008] with STM, 0.82 Å with x-ray diffraction [Martoccia *et al.* , 2010], 1.1 Å with classical molecular dynamics (CMD) [Süle & Szendrő, 2014] to 1.53 Å [Moritz *et al.* , 2010] with LEED and DFT. In addition, these diffraction and calculation results show that a buckling is also present in the top layers of the substrate, although not as important as in the graphene on top. It has been reported that the topmost layer of Ru(0001) has a modulated amplitude between 0.19 and 0.26 Å [Martoccia *et al.* , 2010, Moritz *et al.* , 2010]. The coincidence of the buckling between the graphene and the substrate has been debated, either having the maximum amplitude of one corresponding with the minima of the other [Martoccia *et al.* , 2010] or maxima being on top of each other as well as minima [Moritz *et al.* , 2010], the latter being the correct one.

In this chapter, we address the model graphene/Ir(111) system, typical of a weak graphene-metal interaction. First, specific methods are introduced, a reminder of SXRD and indexation of the diffraction signals and the model used to describe the results. Then, we deduce the average distance between graphene and Ir(111), and determine amplitude of the graphene undulation, with the combination of the SXRD and extended x-ray reflectivity (EXRR) results, the latter not having been employed to characterize monolayer graphene on a substrate before. Besides, we are able to estimate the undulation of the Ir layers, which is usually not accessible to other techniques.

5.2 Speficic methods and model

5.2.1 Experimental setups and measurements

The measurements were performed in ultra-high vacuum chambers coupled with z axis diffractometers, the non-specular crystal truncation rods (CTRs) were measured on BM32 and the specular rod, $00L$, was measured by EXRR on ID03. The x-ray beam energy was set at 11 keV, 1.127 Å. The reciprocal space scans of the scattered intensity presented below are all normalized to the intensity measured with a monitor placed before the sample. For the SXRD measurements, the intensity along the Ir(111) crystal truncation rods (CTRs) and along the graphene rods was measured with a Maxipix two-dimensional detector in stationary mode for the upper range of the out-of-plane scattering vector component (*i.e.* large values of the out-of-plane reciprocal space coordinate L), and by performing sample rocking scans for low L-values [Drnec *et al.* , 2014]. The amplitude of the structure factors $F_{H,K}(L)$ - the square root of the measured intensity - for the different CTRs and graphene rods, corresponding each to different values of the in-plane reciprocal space parameters H and K, were extracted and processed with the PyRod program described in Ref. [Drnec *et al.* , 2014]. PyRod was also used to simulate the structure factors using the model described below, and to refine the structural parameters of this model with the help of a least squares fit of the simulation to the data. The total uncertainty on the experimental structure factors is dominated by the systematic error estimated to be 6.1%, according to Ref. [Drnec *et al.* , 2014]; the statistical error being everywhere smaller than 1 %.

The Ir single crystal was cleaned and the graphene grown following the two steps growth, TPG then CVD described in the previous chapter to obtain only the RO° variant. Two samples were prepared, one in each of the UHV chambers installed at the BM32 and ID03 beamlines where the SXRD and EXRR experiments were performed respectively. The triangular crystallographic unit cell of the iridium surface has a lattice parameter of 2.7147 Å at room temper-

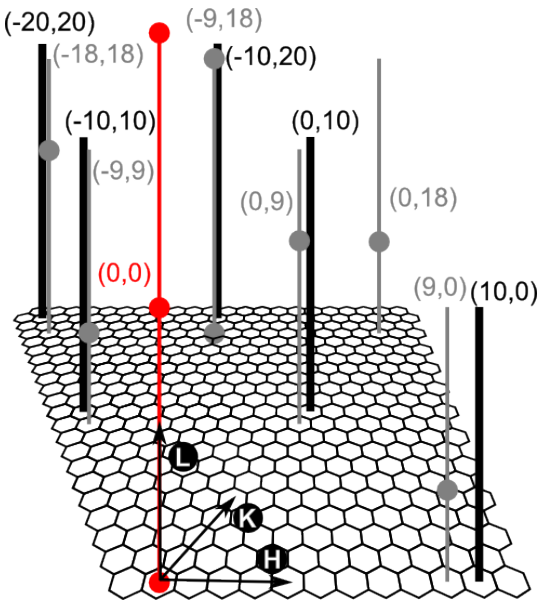

Figure 5.1: Sketch of the reciprocal space, the hexagonal grid shows the partition of its (H,K) plane according to the 10-on-9 commensurability. H, K and L are in reciprocal lattice unit of the moiré (superlattice) surface unit cell. In gray are shown the measured CTRs from the iridium, with circles to highlight the positions of the different Bragg reflections. The graphene rods are shown in black. The specular CTR (H=K=0) is shown in red. Each is labelled with its (H,K) position in the 10-on-9 moiré surface supercell.

ature. The graphene unit cell has a measured lattice parameter of 2.4530 Å. The ratio between the two lattice parameters, 0.903, is close to 0.9. Therefore, in the following we assume that the system is commensurate, with a (10×10) graphene cell coinciding with a (9×9) iridium one, $(10 \times 10)_{Gr} \times (9 \times 9)_{Ir}$. In the following, the in-plane unit cell of reciprocal space is the moiré one. This corresponds to H or K indexes multiples of 9 and 10 for Ir CTRs and graphene rods, respectively (Fig. 5.1).

Figure 5.2 shows the Ir CTRs and graphene rods. As expected for a (essentially) two-dimensional layer such as graphene, the graphene rods are basically featureless [Charrier *et al.* , 2002]. Qualitatively, because the undulations of the graphene and top substrate layers are expected to be small, the main features are *i*) the pronounced interference effect on the specular rod $F_{0,0}(L)$ related to

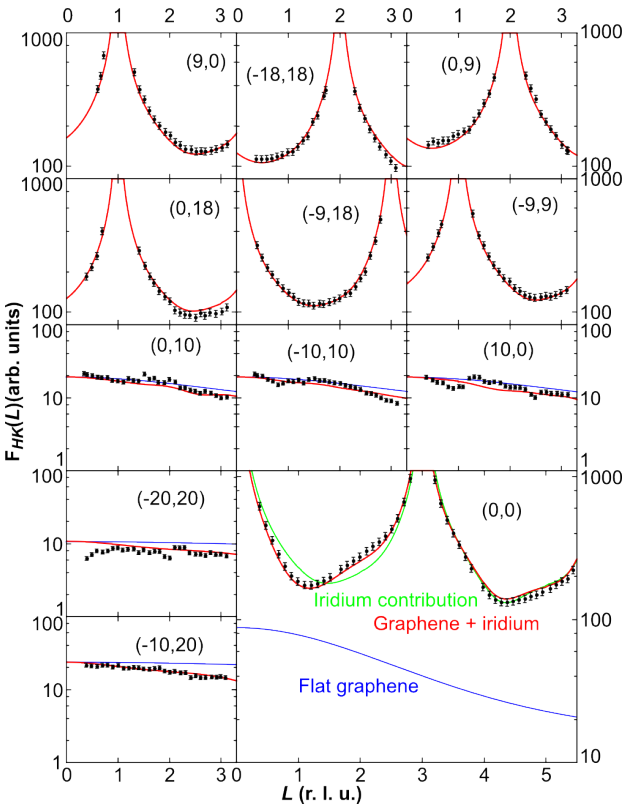

Figure 5.2: Experimental structure factors $F_{H,K}(L)$ of iridium CTRs and graphene rods from SXRD measurements of the first sample in black with the error bars. The solid red lines represent the best fit with the Fourier model. In blue with the rods is the contribution of a flat graphene layer alone, to highlight the effect of the rugosity and undulations on the rods. The specular rod (0,0) from the second sample is reported in the bottom right in black with error bars. The solid red line represents the final fit, the green one the contribution of the iridium alone and in blue the contribution of a flat graphene layer alone.

the average distance dz_{Gr} between Ir and graphene, expected to be larger than the bulk distance of 2.2 Å; *ii*) the decrease of the otherwise featureless CTRs in between Bragg peaks, related to the substrate roughness ; and *iii*) the decrease of the graphene rods with increasing L, dominated by the undulation of the graphene layer, as shown with the simulated graphene rods for a flat graphene layer alone in Fig. 5.2. This decorrelation between roughness and undulation allows these parameters to be determined with high accuracy.

5.2.2 The Fourier model

In order to achieve a quantitative characterization of the topography of the system, we introduce a simple model [1]. A limited set of parameters (see Fig. 5.3), including the average interplanar distances, the actual roughness, and the amplitude of undulation of each layer, seems to be a reasonable option for a simple modelling of the system. In order to approach this description, we introduce a lattice model based on a Fourier series, such as the one proposed for graphene/Ru(0001) [Martoccia *et al.* , 2010]. In this model, the displacement in the direction i ($i = \{x,y,z\}$) of an atom with x, y and z coordinates, with respect to the corresponding position in a flat layer, is given by

$$\mathrm{d}r^i = \sum_{s,t} A^i_{s,t} \times \sin[2\pi(sx+ty)] + B^i_{s,t} \times \cos[2\pi(sx+ty)] \tag{5.1}$$

where the sum runs over the different orders of the series. Due to the crystal symmetry of graphene and Ir(111), the displacements must respect a $p3m1$ symmetry, *i.e.* they must fulfil

$$\mathrm{R_j}^{-1}\{\mathrm{d}\mathbf{r}[\mathrm{R_j}(\mathbf{r})]\} = \mathrm{R_j}\{\mathrm{d}\mathbf{r}[\mathrm{R_j}^{-1}(\mathbf{r})]\} \tag{5.2}$$

with $j \in [0,5]$. R_0 is the identity matrix, R_1 and R_2 correspond to the $\pm$ 120° rotations and the last three to the mirror planes.

$$\begin{aligned} \mathrm{R}_0 = \begin{pmatrix} 1 & 0 \\ 0 & 1 \end{pmatrix}, \mathrm{R}_1 = \begin{pmatrix} 0 & \bar{1} \\ 1 & \bar{1} \end{pmatrix}, \mathrm{R}_2 = \begin{pmatrix} \bar{1} & 1 \\ \bar{1} & 0 \end{pmatrix}, \\ \mathrm{R}_3 = \begin{pmatrix} 0 & \bar{1} \\ \bar{1} & 0 \end{pmatrix}, \mathrm{R}_4 = \begin{pmatrix} \bar{1} & 1 \\ 0 & 1 \end{pmatrix}, \mathrm{R}_5 = \begin{pmatrix} 1 & 0 \\ 1 & \bar{1} \end{pmatrix} \end{aligned} \tag{5.3}$$

These symmetry constraints impose that not all Fourier coefficients in Eq.

[1] Independently refining the positions of each atom in a commensurate cell, comprising few 100 C and Ir atoms, obviously would provide a non reliable structural picture given that the number of free parameters would approach or even exceed the number of experimental points.

(1) are independent. Their relationships are given in Table 5.1.

$A^x_{s,t}$	$=-A^x_{t,-s-t}+A^y_{t,-s-t}$	$=-A^y_{-s-t,s}$	$=-A^y_{-t,-s}$	$=-A^x_{-s,s+t}+A^y_{-s,s+t}$	$=$	$A^x_{s+t,-t}$
$A^y_{s,t}$	$=A^x_{-s-t,s}-A^y_{-s-t,s}$	$=-A^x_{t,-s-t}$	$=-A^x_{-t,-s}$	$=-A^y_{-s,s+t}$	$=A^x_{s+t,-t}-A^y_{s+t,-t}$	
$A^z_{s,t}$	$=A^z_{t,-s-t}$	$=A^z_{-s-t,s}$	$=A^z_{-t,-s}$	$=A^z_{-s,s+t}$	$=$	$A^z_{s+t,-t}$
$B^x_{s,t}$	$=-B^x_{t,-s-t}+B^y_{t,-s-t}$	$=-B^y_{-s-t,s}$	$=-B^y_{-t,-s}$	$=-B^x_{-s,s+t}+B^y_{-s,s+t}$	$=$	$B^x_{s+t,-t}$
$B^y_{s,t}$	$=B^x_{-s-t,s}-B^y_{-s-t,s}$	$=-B^x_{t,-s-t}$	$=-B^x_{-t,-s}$	$=-B^y_{-s,s+t}$	$=B^x_{s+t,-t}-B^y_{s+t,-t}$	
$B^z_{s,t}$	$=B^z_{t,-s-t}$	$=B^z_{-s-t,s}$	$=B^z_{-t,-s}$	$=B^z_{-s,s+t}$	$=$	$B^z_{s+t,-t}$

Table 5.1: Relationships between the Fourier coefficients $A^i_{s,t}$ and $B^i_{s,t}$ ($i = \{x, y, z\}$)

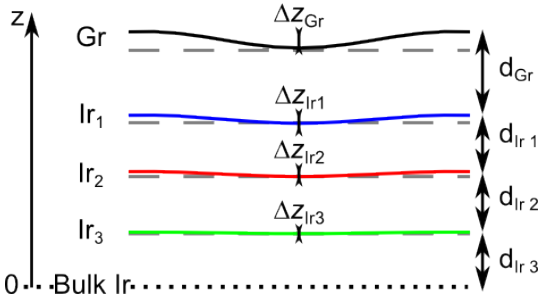

Figure 5.3: Sketch of the parameters studied. In black is the graphene and in blue, red and green are the surface layers of iridium. The amplitudes of their corrugation are shown by arrows in the middle. The start of the bulk iridium is sketched with the dotted black line. The gray dashed lines represents the expected bulk positions for the different atomic layers without corrugation. The z-axis on the left is a reference to the linear dependency of the iridium corrugation amplitude.

In the following we further simplify the model by limiting the Fourier development to first order, which is legitimate due to the fact that no significant diffraction data is measurable beyond first order (a diffraction experiment is actually a measurement of the Fourier transform of the electronic density, thus, to a good approximation, of the shape of graphene). In this framework, the x, y and z displacements simply write:

$$\begin{aligned} \mathrm{d}r^x = A^x \times (2 \times \sin(2\pi x) + \sin(2\pi y) + \sin(2\pi(x-y))) \\ +B^x \times (2 \times \cos(2\pi x) - \cos(2\pi y) - \cos(2\pi(x-y))) \end{aligned} \tag{5.4}$$

$$\begin{aligned} \mathrm{d}r^y = A^x \times (\sin(2\pi x) + 2 \times \sin(2\pi y) - \sin(2\pi(x-y))) \\ +B^x \times (\cos(2\pi x) - 2 \times \cos(2\pi y) + \cos(2\pi(x-y))) \end{aligned} \tag{5.5}$$

$$\begin{aligned} \mathrm{d}r^z = A^z \times (2 \times \sin(2\pi x) - 2 \times \sin(2\pi y) - 2 \times \sin(2\pi(x-y))) \\ +B^z \times (2 \times \cos(2\pi x) + 2 \times \cos(2\pi y) + 2 \times \cos(2\pi(x-y))) \end{aligned} \tag{5.6}$$

Thus, only two variables per atomic plane, A^x and B^x, are needed to describe the in-plane displacements. The model is applied to graphene/Ir(111), with three iridium layers and one graphene layer. Each of these layers is characterized by four Fourier coefficients (A^x, B^x, A^z and B^z), plus another parameter corresponding to an average z displacement of the layer from its equilibrium position in the bulk. In order to further reduce the number of free parameters, the A^z and B^z of the three iridium layers were constrained with a linear dependence as a function of depth, and zero undulation of the deepest Ir layer, in the bulk, as shown in Fig. 5.3. The topographic parameters of the model are listed in Table 5.2.

5.3 Results and discussion

The Fourier model was used to fit the SXRD data. The expected in-plane displacements, below 0.01 Å according to first principle calculations [Busse *et al.* , 2011], have no noticeable influence on the Ir CTRs and graphene rods, and are discarded in the simulations [2]. The best fit lead to a χ^2 value of 3.5 and the results are shown in Table 5.2. We find a 98 ± 2% graphene coverage. The graphene is found to have a mean distance of $dz_{Gr} = 3.39 \pm 0.28$ Å with its substrate and a corrugation of $\Delta z_{Gr} = 0.379 \pm 0.044$ Å. The graphene distance with its substrate is close to the interlayer spacing in graphite, 3.36 Å. As explained above, the

[2] Actually, we tested that even 0.05 Å in-plane displacements have no substantial effect.

benefit of the SXRD analysis of both graphene and Ir contributions is to provide an accurate value of the amplitude of the graphene undulation perpendicular to the surface, as compared to other techniques. The interlayer Ir spacings are found to be 2.203 ± 0.012 Å, 2.212 ± 0.007 Å and 2.223 ± 0.002 Å from top to bottom. The topmost layer of iridium has an undulation of 0.017 ± 0.002 Å, the second layer has an undulation of 0.011 ± 0.001 Å, and the last one is 0.006 ± 0.001 Å. Finally, the roughness of the iridium substrate is found to be 0.42 ± 0.20 Å. This small value may be linked with the small coherence length of the X-ray beam (corresponding to about 10 flat Ir terraces separated by atomic step edges) on the BM32 beamline.

The best fit between simulations and SXRD data is achieved for an iridium undulation in phase with the graphene one, with a smaller amplitude though. This finding is at variance with that obtained in earlier scanning probe microscopy measurements performed in specific imaging conditions [Sun *et al.* , 2011], and supports the picture progressively assembled through other reports, based on scanning probe microscopies [Dedkov & Voloshina, 2014, Boneschanscher *et al.* , 2012], XSW [Busse *et al.* , 2011], and first principle calculations [N'Diaye *et al.* , 2006, Busse *et al.* , 2011].

The main limitation of this SXRD analysis is the rather large uncertainty on the dz_{Gr} distance. This motivated complementary measurements of the specular rod on the second sample, using the ID03 setup as the extended reflectivity was not accessible in the BM32 setup. The EXRR result is shown in Fig. 5.2 together with the best fit and simulated and graphene specular rods. The best fit of the specular rod, yielding a χ^2 value of 1.064, was done with a simplified model, in which the undulations of both the iridium or graphene were fixed at the values obtained from the SXRD analysis. It yields a value of $dz_{Gr} = 3.38$ Å, very close to that determined on the other sampler by off-specular SXRD, but with a much better accuracy, $\pm$ 0.04 Å. The graphene layer of this second sample is found incomplete, with a $90 \pm 2\%$ graphene coverage. In addition, the spacings between the topmost Ir planes, found to be 2.203 ± 0.010 Å, 2.205

$\pm$ 0.008 Å and 2.225 $\pm$ 0.004 Å from top to bottom (2.217 Å in the bulk). The substrate roughness in this case is found to be 1.1 $\pm$ 0.1 Å, larger than that obtained from SXRD. This is however expected since the coherence length of the beam is two orders of magnitude larger here, *e.g.* around 1000 atomic steps of the substrate scatter the beam coherently.

	SXRD (1^{st} *sample)*	*EXRR* (2^{nd} *sample)*	*DFT calculations*	*Busse et al.*	*Hämäläinen et al.*
dz_{Gr}	3.39 ± 0.28	3.38 ± 0.04	3.43	3.38 ± 0.04	3.39 ± 0.03
Δz_{Gr}	0.379 ± 0.044		0.46	0.6 ± 0.1 1.0 ± 0.2	0.47 ± 0.05
dz_{Ir_1}	2.203 ± 0.012	2.203 ± 0.010	2.190		2.222
dz_{Ir_2}	2.212 ± 0.007	2.205 ± 0.008	2.175		2.224
dz_{Ir_3}	2.223 ± 0.002	2.225 ± 0.004	2.184		2.222
Δz_{Ir_1}	0.017 ± 0.002		0.019		0.006
Δz_{Ir_2}	0.011 ± 0.001		0.018		0.006
Δz_{Ir_3}	0.006 ± 0.001		0.010		0
ρ	0.42 ± 0.20	1.05 ± 0.08			
O_{Gr}	$98 \pm 2\%$	$90 \pm 2\%$	100%	39% 63%	*Partial*

Table 5.2: Topographic parameters for the two samples, the DFT calculations and results from Ref. [Busse et al. *, 2011] (XSW) and [Hämäläinen* et al. *, 2013] (LEED + AFM). dz_{Gr} is the mean distance between the graphene and its substrate; Δz_{Gr} is the graphene undulation amplitude; dz_{Ir_1}, dz_{Ir_2} and dz_{Ir_3} are the interlayer distances of the iridium surface layers and Δz_{Ir_1}, Δz_{Ir_1} and Δz_{Ir_1} are their undulation amplitudes; ρ is the roughness of the sample surface; O_{Gr} is the graphene coverage in percent. All the parameters are in ångströms (Å) except the coverage.*

This is the first study of a sample with a complete graphene coverage, thus the deviations from previous studies can be explained due to strains in the full layer that can relax in graphene island. This could also be explained by the difference in the growth process (temperature, methods...) and Busse *et al.* [Busse *et al.* , 2011] showed that the undulation varies depending on the graphene coverage, 0.6 Å for a coverage of 39 % and 1 Åfor 63 %. Moreover, the undulation could also be affected by the growth methods (full/partial growth, chemical vapour deposition, temperature programmed growth...) and growth temperature as it has been reported that these parameters affect the graphene lattice parameter and its commensurability with the substrate. The

iridium undulations are also found larger than those deduced from a LEED study [Hämäläinen *et al.* , 2013]. This might be due to some limitation of LEED to analyse layers below the graphene one, because of the small electron mean free path. They are also very close to those reported for clean Ir(111) surfaces without graphene [Matsumoto & Ogura, 2007].

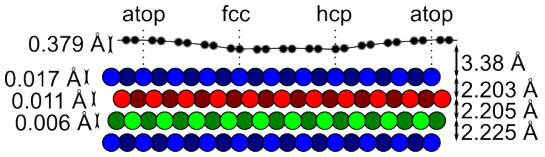

Figure 5.4: Cut of the 10-on-9 commensurability to represent the corrugations and displacements of the atomic layers. Carbon atoms of the graphene are black circles, the iridium atoms are in blue, red and green to show the ABC stacking of the different layers. The three coincidence regions of graphene with the substrate as well as the corrugations and interlayer spacing are denoted.

The graphene-metal distance which we obtain is in good agreement with values deduced by XSW, LEED, and AFM (see Table 5.2). The undulation of the graphene which we obtain is also in agreement with that found by LEED and AFM. It is however smaller than that deduced from XSW. The difference might originate from two effects. First, we recently found that the in-plane lattice parameter of graphene varies as a function of the preparation method, which is different in Refs. [Busse *et al.* , 2011, Hämäläinen *et al.* , 2013] and in the present work. Given that the strain is closely related to the graphene buckling (undulation) [Runte *et al.* , 2014], we indeed expect different undulations in each of these reports. Second, the strain (and thus buckling) of graphene was argued to depend on the fraction of edge atoms in graphene, i.e. on graphene coverage [Busse *et al.* , 2011]. Our results, unlike those in Refs. [Busse *et al.* , 2011, Hämäläinen *et al.* , 2013], address close-to-full layer graphene.

The Fourier model was also tested to fit the displacements obtained by the DFT calculations described in [Busse *et al.* , 2011]. The model was in very good accordance with the DFT calculations results, in particular the iridium top layer

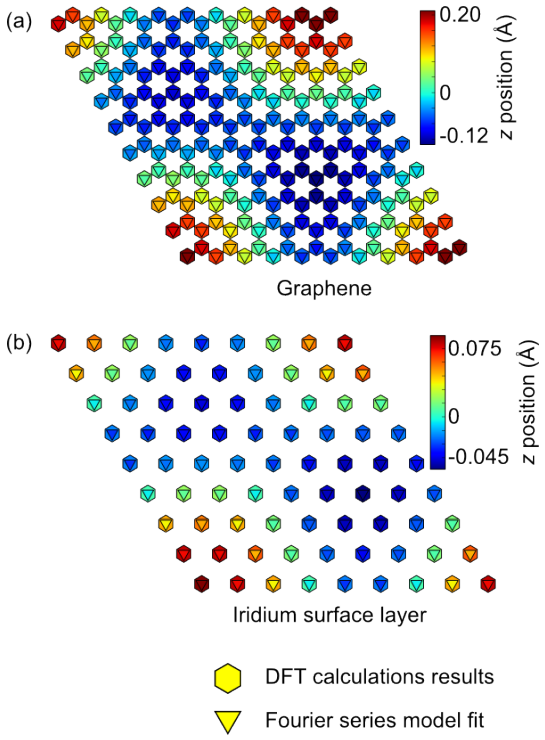

Figure 5.5: Sketches of graphene (a) and the topmost iridium layer (b) with the DFT calculations results shown in hexagons and the Fourier series fit in reverse triangle The out of plane corrugation is shown with a color gradient, with the scales in Å.

and graphene, thus confirming that the first order Fourier component is enough to describe the system, as shown in Fig 5.5. Moreover, it also confirmed that A^z and B^z of the three iridium layers have an almost linear dependence as a function of depth. From the DFT simulation, the corrugations of the iridium surface layers from top to bottom are 0.014 Å, 0.012 Å and 0.04 Å while the graphene one is 0.35 Å, which are close to the experimental results.

In fact, this method of analysis has a limit too, as our starting hypothesis on the structure of the supercell, a (10×10) graphene cell coinciding with a (9×9) iridium, may have an impact on the results. It was reported previously that this system cannot be consider fully commensurate, as it is really a composition of commensurate domains with incommensurate boundaries [Blanc *et al.* , 2012] and that the thermal history of the sample effects it as discussed in the previous

chapter. Here, the 9.03 ratio indicates that there should be a combination of $(10 \times 10)_{Gr} \times (9 \times 9)_{Ir}$, $(21 \times 21)_{Gr} \times (19 \times 19)_{Ir}$ and incommensurate domains. However, despite the complexity of the sample, the starting hypothesis of the problem allows to extract a good approximation of the actual structure.

5.4 Conclusion

To conclude, we have established that SXRD including the specular rod is a powerful method to finely describe the topography of graphene on a metal, even for very small corrugation amplitudes, as is the case for graphene on Ir(111). We were able to extract reliable values of the average interplanar distances (graphene-Ir, Ir-Ir), and of the undulation of the different layers, the latter with a high precision as compared to other techniques, so that even the weak undulation of buried layers can be inferred. This precision is allowed by the possibility to disentangle the undulation from roughness (a disordered variation of the height). The average graphene-Ir distance is found to be 3.38 ± 0.04 Å, its undulation along the moiré lattice is 0.379 ± 0.044 Å, and the corresponding undulation in the Ir topmost layer is 0.017 ± 0.002 Å. The approach that we report is also applicable to other hetero-interfaces, for instance graphene on metals, metals on metals, ultrathin oxides on metals, and should prove especially valuable to detect and characterize small deviation to the ideal case of perfectly 2D layers.

Chapter 6

Growth and structure of self-organized nanoparticles on graphene on Ir(111)

6.1 Introduction

We have discussed in a previous chapter that metallic nanoparticles have attracted a lot of interest due to their new or enhanced properties, depending strongly on their sizes and environments. Therefore, monodisperse assemblies of nanoparticles, such as can be produced by self-organization, have received special attention. Such assemblies may be useful in various field of applications such as magnetic [Weiss *et al.* , 2005, Ahniyaz *et al.* , 2007], optical [Kreibig & Vollmer, 1995, Ye *et al.* , 2010] or catalytic [Yoo *et al.* , 2009, Nesselberger *et al.* , 2013, Guo *et al.* , 2009]. For example, enhanced or new catalytic properties with metallic nanoparticles should prove very useful in industry to improve the efficiency of catalytic exhaust pipe while reducing costs. Recently, the development of epitaxial graphene on transition metals has opened new possibilities, with many types of graphene/metal moiré superlatices depend-

ing on the interaction and lattice mismatch between graphene and the metal as well as on the metal surface crystal symmetry. For example, the graphene on Ru(0001) system has been used as a template to grow a wide variety of nanoparticle of different size and made of various metals [Zhou *et al.* , 2010, Liao *et al.* , 2011, Wang *et al.* , 2012]. The moiré of graphene on Ir(111) is probably the most efficient pattern for self-organization of various kind of pure and bi-metallic nanoparticles [N'Diaye *et al.* , 2006, N'Diaye *et al.* , 2009], having sizes from 3 to about 100 atoms. by fully using the moiré pattern to obtain arrays of monodisperse nanoparticle of the same size. However, most studies have been performed with STM, thus making it difficult to determine the exact shape, size and atomic structure of the nanoparticles [N'Diaye *et al.* , 2009, Gerber *et al.* , 2013]. As previously shown with the topography of epitaxial graphene, we used surface x-ray diffraction to determine their internal structure.

Note that a first SXRD study has been recently published [Franz *et al.* , 2013] on a very similar system, self-organised iridium nanoparticles on the moiré of graphene on Ir(111). The Ir nanoparticles were larger (82 atoms) than those studied in this chapter, 20 and 40 atoms, and thus yielded more intense scattering. Moreover, in this study, the SXRD results were complemented by use of normal incidence x-ray standing wave (NIXSW). This latter synchrotron technique provides additional information using the C 1s photoemission signal, in particular on the structure of the graphene below the nanoparticles. It was concluded that the graphene sheet is deformed below the particle as a result of bonding between the particles on graphene. The graphene below the nanoparticle was suggested to rehybridize to sp^3 upon the formation of C-Ir bonds with the substrate atoms below. One noticeable result of Franz's study is that slightly more than half of the hcp moiré sites are occupied by nanoparticles. The excess matter is gathered in nanoparticles that are out of the hcp crystallographic sites (see Chapters 2 and 5 for the description of the crystallographic sites). One can wonder if another type of atoms known to self-organise on the

moiré such as platinum [N'Diaye *et al.* , 2009], a material of choice in view of nanocatalysis, has a similar degree of organisation. In addition, the motivation for smaller nanoparticles is driven by the expected enhanced catalytic properties [Gerber *et al.* , 2013]. Finally, for bimetallic nanoparticles, the question arises about what is their natural structure : random alloy, atomic ordering or layered structure ? As we have discussed previously, cobalt does not self-organise alone on epitaxial graphene. We used the small platinum nanoparticles as seeds on the lattice before the cobalt deposition.

In this chapter, after presenting the specific experimental parameters, the SXRD results of three different samples will be presented : nanoparticles of 20 and 40 platinum atoms and bimetallic nanoparticles of 20 platinum and 20 cobalt atoms. Then, these results will be discussed and compared to each others and with the study of Ref. [Franz *et al.* , 2013].

6.2 Experiments

6.2.1 Specific experimental methods

As in the previous chapters, the experiments took place at the BM32 beamline, in a UHV chamber coupled with a z-diffractometer. The graphene growth was done with the two steps growth process, TPG then CVD, to obtain a full graphene layer on Ir(111) with well-defined epitaxial relationships. Platinum and cobalt were deposited at room temperature on the sample using electron bombardment evaporation cells. The deposition rates were calibrated prior to the experiment using the quartz microbalance. They were 0.05 platinum monolayer and 0.41 cobalt monolayer per minute respectively. A deposition of one monolayer corresponds to an interlayer distance in bulk Pt(111) and Co(0001), *i.e.* 2.265 Å and 2.035 Å, respectively.

This study was done on several samples, with nanoparticles of different sizes and compositions, with an average number of atoms deposited per moiré superlattice determined from the deposition rates assuming they organise and occupy

all nucleation site. For the bimetallic nanoparticles, the previous 20 platinum atoms nanoparticles were used as the seeds, thus only two graphene samples were prepared.

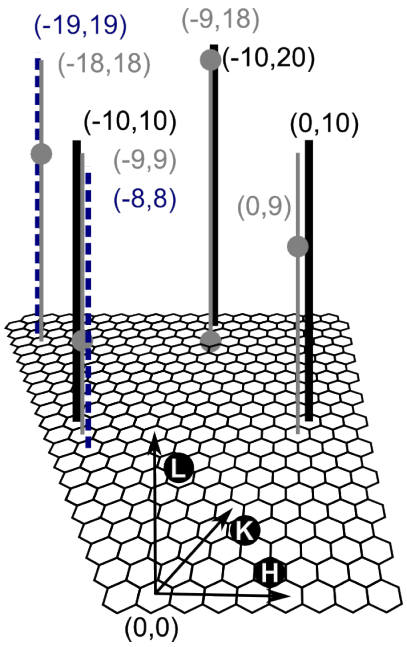

Figure 6.1: Sketch of the reciprocal space. The hexagonal grid shows the cut of its (H,K) plane according to the 10-on-9 commensurability within the triangular reciprocal lattice. H, K and L are in reciprocal lattice unit of the moiré (superlattice) surface unit cell. In gray are shown the measured CTRs from the iridium, with disks to highlight the positions of the different Bragg reflections. The graphene rods are shown in black and the moiré rods an in dashed dark blue. Each is labelled with its (H,K) position in the 10-on-9 moiré surface supercell.

The graphene was characterised first by x-ray diffraction before growing nanoparticles on top. Its lattice parameter a_{Gr} at room temperature is found to be 2.454 $\pm$ 0.001 Å for both growths. As mentioned before, this corresponds to a ratio a_{Gr}/a_{Ir} of 0.904 $\pm$ 0.001, almost a $(21 \times 21)_{Gr} \times (19 \times 19)_{Ir}$ commensurability ratio. However, for the analysis to be tractable, a $(10 \times 10)_{Gr} \times (9 \times 9)_{Ir}$ commensurability superlattice will be used to model the structure and the same indexation for the H, K and L indexes as in the previous chapter is also used. Bulk platinum has a face centred cubic structure like iridium and its (111) sur-

face lattice parameter, a_{Pt} = 2.774 Å , is slightly larger than the iridium one (2.715 Å), by 2.2%. Therefore, relaxed platinum should give distinct rods. However, because its lattice parameter is close to the iridium one, it is not possible to distinguish its rods from the Ir CTRs with a sub monolayer deposition due to their proximity and low intensity of the platinum one. Cobalt has an hexagonal close-packed structure, with a surface lattice parameter a_{Co} of 2.5071 Å, 7,9% smaller than a_{Ir}.

These experiments were performed during the same session as the previous chapter, thus the beam, setup characteristics and total uncertainty are identical. The CTRs and rods measured on the three samples are sketched in Fig. 6.1.

6.2.2 Grazing incidence x-ray diffraction

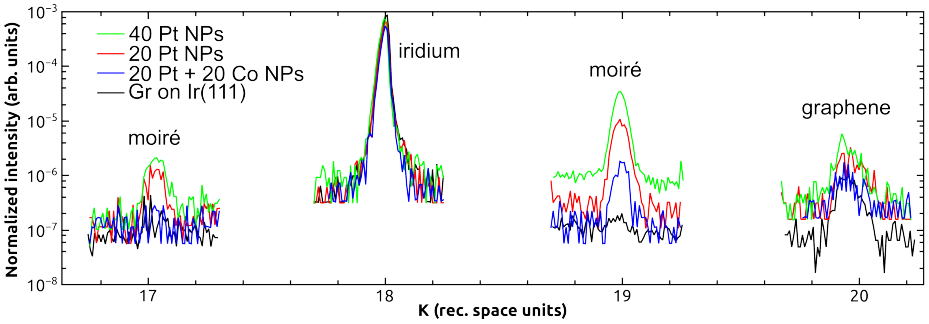

Figure 6.2: Scans of the reciprocal space in the HK plane at L=0 along the K direction around the (0,18) iridium CTR for the different samples, bare graphene on iridium in black, with nanoparticles of Pt_{20} atoms on top in red, Pt_{40} in green and $Co_{20}Pt_{20}$ in blue. The scans show peaks, their intensity normalised by the monitor, with moiré ones positioned at K=17 and 19, the iridium at 18 and graphene at 20.

As we have discussed previously, the moiré gives rods in SXRD whose intersection with the $L = 0$ plane are observed in the grazing incidence and exit configuration. With bare graphene on Ir(111), their low signal is difficult to measure, as illustrated in Fig. 6.2 with a scan along the K direction. Only the superlattice rod between the iridium CTR and the graphene rod is slightly above background. However, after platinum deposition and thus decoration of

the moiré by nanoparticles, more moiré rods become measurable. It can also be noted that the intensity measured in-plane depends on the amount of platinum deposited, with the maximum for 40 atoms deposited per unit cell. However, this is not the case for 20 cobalt atoms deposited after 20 platinum ones, as the intensity of the moiré rod in the HK plane decreases and the background increases. This would indicate that, in the $Co_{20}Pt_{20}$ case, there is less organisation on the moiré sites and probably a certain amount of coalescence of the nanoparticles. Therefore, despite the previous seeding of the sites, it seems that a small portion of the cobalt deposited forms nanoparticles of various size that are not positioned on specific moiré sites, as it has been observed on graphene on Ru(0001) [Liao *et al.* , 2011].

6.3 Analysis of surface x-ray diffraction from nanoparticle lattices

6.3.1 Comparative qualitative analysis of structural variations

To obtain further details on the structure, sets of CTRs and rods were measured on each samples. As in the previous chapter, all the amplitudes of the structure factors $|F_{H,K}(L)|$ were extracted and processed with PyRod [Drnec *et al.* , 2014] and shown in Fig. 6.3. In total, nine are presented here and were used in the analysis but several more were measured but did not show an intense enough signal from which meaningless data could be extracted. The graphene and moiré rods used here have a signal to noise ratio around 10. As in the previous chapter, the accessible reciprocal space accessible in L is restricted by the beam wavelength and the setup, thus the maximum measured values at $L \approx 3.2$

A general point for all the results is that one can already extract structural informations from the shape of the CTRs and rods. The iridium CTRs present

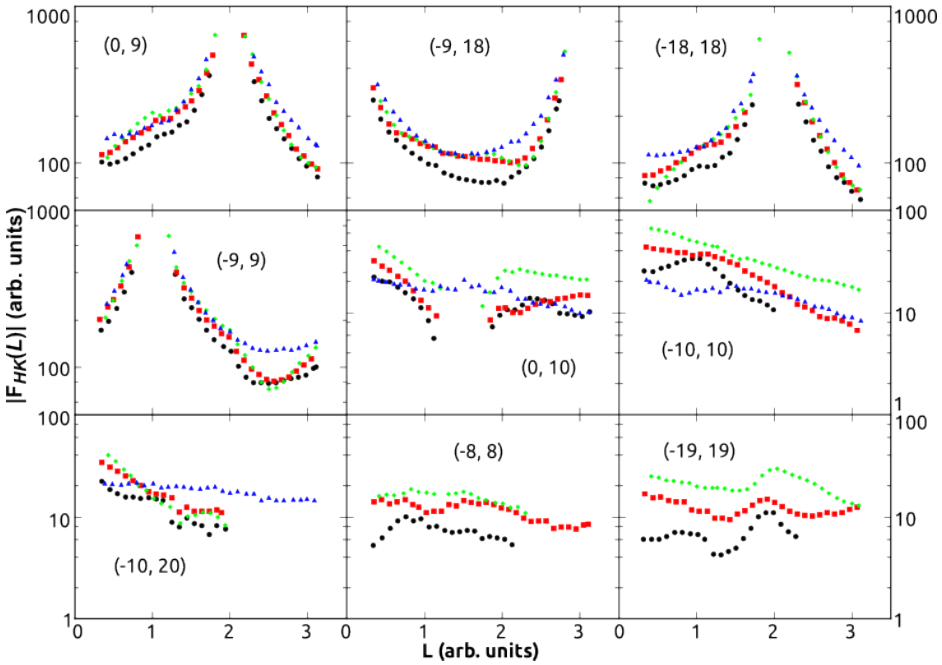

Figure 6.3: Experimental structure factors $|F_{H,K}(L)|$ of the samples measured with SXRD, including bare graphene on Ir(111) from the previous chapter in blue triangle, Pt_{40} nanoparticles grown on the graphene in green diamonds Pt_{20} nanoparticles grown on the graphene in red squares and $Co_{20}Pt_{20}$ nanoparticles grown on the graphene in black circles.

bumps away from the Bragg peaks near integer position in L that were not present with bare graphene on Ir(111). This is a signature of the nanoparticles and this indicates that their in-plane lattice parameters are close to the iridium one to be observed at these values of (H, K) in the reciprocal space. The position of the bumps away from the Bragg peaks indicates that at least some particles adopt a perpendicular stacking that differs from the substrate stacking. By comparison, the bumps near integer L-values away from the Bragg peaks in the CTRs from the Pt_{40} sample are more pronounced as expected since more material has been deposited. In addition it could indicate that the bigger organised nanoparticles now occupy possibly more moiré sites. There are also minima that are below the minima of CTRs from the previous data of graphene on Ir(111), around $L = 2.5$ on the (-9,9) for example. This effect is typical of surface roughness [Robinson, 1986] and it remains to be determined if it is only the substrate roughness or the nanoparticles having partially the same effect on the rods. Furthermore, the $Co_{20}Pt_{20}$ presents lower minima than the others CTRs, possibly indicating an increased surface roughness and/or less organisation from the nanoparticles.

Moreover, the graphene rods (0,10), (-10,10) and (-10,20) have completely different shape from those of graphene on Ir(111). They also show larger modulations with respect to graphene alone and even almost an extinction can be seen on the (0,10) rod. Finally, several moiré rods were measured. They show modulations as well, with maxima close to integer values of L. Overall, the graphene and moiré rods from the Pt_{40} are more intense than the others as one can expect from the quantity of atoms deposited. However, the rods from the $Co_{20}Pt_{20}$ sample are less intense, even by comparison with the Pt_{20} sample that served as the seeds to grow them. This would go along with a possible lesser organisation of the nanoparticles on the moiré sites.

6.3.2 Model used for quantitative structural characterization

We now introduce the general structural model that served to simulate the structure factors. We will start with an general model and then explain the different choices and restrictions applied to it that lead to the final model, shown in Fig. 6.4, used to fit the experimental data. These hypothesises are necessary to keep the number of free parameters as small as possible, because the number of experimental data points is also limited. The symmetry is first used to further reduce the number of parameters, by assuming a three fold axis in the middle of the nanoparticle which all parameter have to respect.

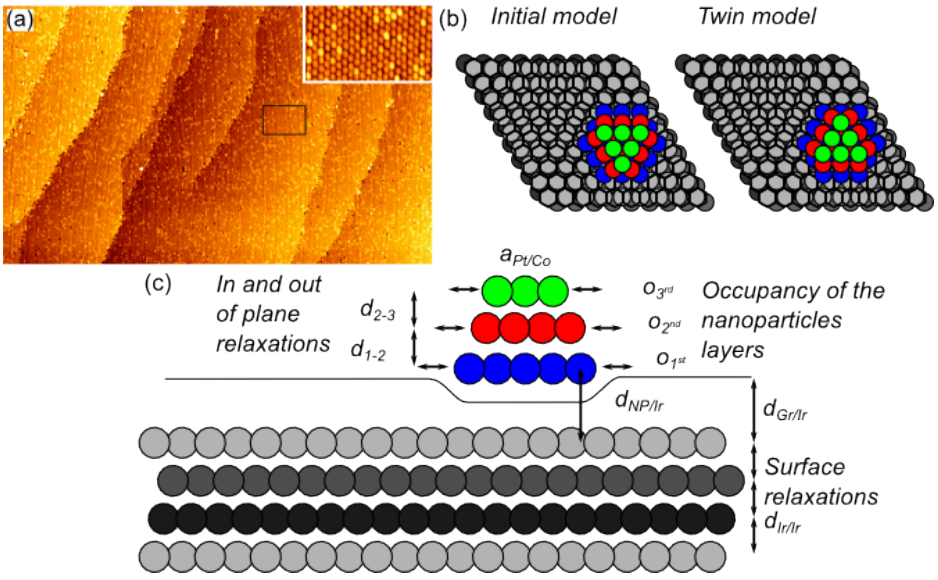

Figure 6.4: (a) STM picture of nanoparticles on top of graphene on Ir(111) with a large field of view from Ref. [N'Diaye *et al.* , 2009]. (b) and (c) Top and side view of the model used in this chapter, with the parameters shown on the side view, at the exception of the occupancies. The iridium atoms of the substrate are shown in grey, with the shades of grey highlighting the ABC stacking, the graphene is shown as black hexagones in the top view and as a black line to facilitate the reading on the side view and the platinum atoms of the nanoparticle are shown in blue for the first layer, red for the second and green for the third.

As in the previous chapter, the iridium substrate was separated in two, with

a bulk part and three surface layers, that can each be relaxed perpendicularly to the surface, corresponding to three free parameters dz_{Ir_1}, dz_{Ir_2} and dz_{Ir_3}. The surface roughness is also introduced with the substrate, following the β-model used in the previous chapter [Robinson, 1986]. The graphene sits on top of the Ir(111) surface. To limit the number of free parameters, and since the rods shape is mostly affected by the nanoparticles ($(f_{Pt}/f_C)^2 \propto (78/12)^2 \approx 42$), in the areas free of nanoparticles, the graphene is kept at same separation distance from the substrate that we found in the previous chapter with bare graphene. This choice is legitimated by the finding that the graphene-substrate distance does not influence substantially the simulations, at least when it is varied in a reasonable range. Below the nanoparticles, graphene is still kept flat but its separation distance was allowed to move perpendicularly to the surface, as in Ref. [Franz *et al.* , 2013]. However, the graphene below the nanoparticle is not displaced during the fit of the experimental data, which is a crude approximation, as such movement has been predicted [Feibelman, 2008] and observed on similar systems [Franz *et al.* , 2013], linked with the formation of sp^3 bonding of the carbon atoms with both the substrate and nanoparticle. Actually, platinum scatters approximately 42 times more than carbon, thus the scattered intensity by the nanoparticle is much more intense than the one by the graphene, making it difficult to observe the variation of only a third of the carbon atoms.

The main part of the model is the nanoparticle itself. Based on symmetry considerations, its shape was chosen to be a truncated hexagonal pyramid, like in other studies [Franz *et al.* , 2013, N'Diaye *et al.* , 2009], with a number of layers and atoms per layers that can be changed according to the amount of material deposited on the surface. We disregard the expected distribution of size of the nanoparticles. They sit above the hcp regions of the moiré superlattice. In an general case, the occupancy of the atoms of the nanoparticles would be described as a function of parallel and perpendicular distances from an origin located at the bottom of the 3-fold axis. However, such a new model would add complexity with more parameters, thus the occupancies of the atoms are

parametrized layer per layer, O_1, O_2 and O_3. In addition, each layer has two relaxations, the interlayer separation and the extension/contraction of the in plane lattice parameter compared to bulk platinum, d_{1-2} and d_{2-3} respectively for the bottom-middle and middle-top interlayer separations and a_{bottom}, a_{middle} and a_{top} for the in-plane lattice parameters.

This model only describes the nanoparticles that are localised exactly above the hcp site. A general model would also take into account off-site particles and the other sites position occupancy. However, there are too many unknowns on their possible position, thus they are not considered here. This was also tested with a preliminary analysis were the nanoparticle in the model was allowed to move freely on the unit cell.

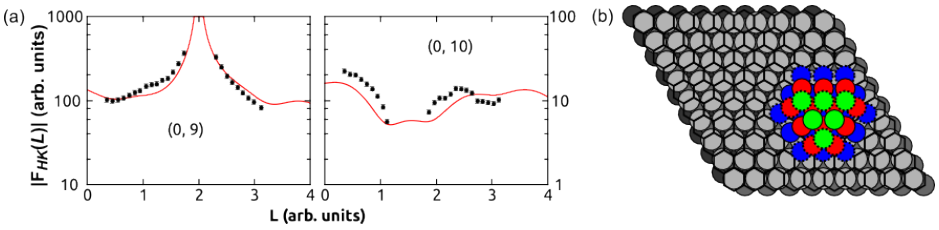

Figure 6.5: (a) Experimental structure factors $|F_{H,K}(L)|$ of the sample with $Co_{20}Pt_{20}$ bimetallic nanoparticles grown on the graphene measured with SXRD in black with their error bars. The solid red line represents the best fit with the $L1_0$ model presented in (b). (b) Top view of the hard sphere model of the structure of the unit cell of the moiré superlattice with the nanoparticle on top of the hcp region. The iridium atoms of the substrate are shown in grey, with the shades of grey highlighting the ABC stacking, the graphene is shown as black hexagons to facilitate the reading and the atoms of the nanoparticle are shown in blue for the first layer and red for the second, with platinum atoms with a solid outline and cobalt atoms with a dashed one.

Furthermore, the CoPt sample presents an additional complexity compared to the pure platinum one: the repartition, ordered or not, of the Co atoms within the nanoparticles. Different possibilities were tested, such as the $L1_0$ alloy structure as shown in Fig. 6.5. The two examples presented shows that on the (0,9) iridium CTR the bump located around $L = 1$ is missing and that the extinction on the (0,10) rod. Other missing or extra features are observed on the other simulated rods that do not agree with the experimental data and thus

this model is ruled out. Another configuration, one with a layer of Co between two layers of platinum all of them parallel to the surface was also tested. Other structures were considered using the model of Pt_{20} nanoparticles covered with a shell of Co atoms and its opposite. The model finally kept is the one with the cobalt shell, as it results in the better fit with the data as presented in Fig. 6.6 (a), for a 50 % of the islands rotated by 180° (so-called twins, see next paragraph). This would indicate that there is no reordering of the atoms, inside the nanoparticles, after deposition.

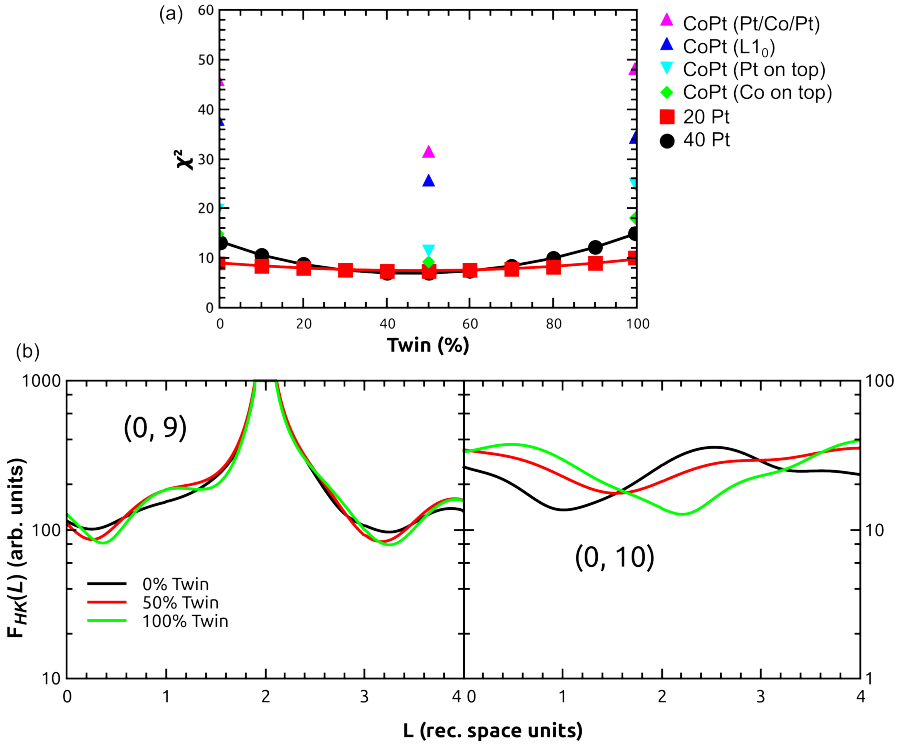

Figure 6.6: (a) Graph showing the evolution of the χ^2 of the best fit of the experimental data as a function of the proportion of twins in the model. (b) Example of simulation of an iridium CTR left (H,K=0,9) and a graphene rod right (H,K=0,10) with three proportions of twin in the model, 0, 50 and 100%, respectively in black, red and green for the Pt_{40} model.

Twins can frequently occur in such systems grown by atomic deposition.It has been reported previously that twins are present in nanoparticles grown

on graphene [Franz *et al.* , 2013], half the nanoparticles being twinned. The twin nanoparticles have a structure which is mirror to that of the nanoparticles described above. Both are shown in Fig. 6.4 (c). They have the same bottom layer but the middle and top layers are both rotated by 180° with respect to the center of the particle, resulting in a stacking inversion. This can be seen on the sketch as the triangle pointing downward for the initial model is pointing upward for the twin. The presence of twinned nanoparticles is observable in a simulation of the structure factors (Fig. 6.6 (b)). It shows more pronounced bumps outside the Bragg peaks on iridium CTRs. For example, bumps that were visible on the (9,0) CTR, are now on the (0,9) CTR with a 100% twins proportion, equivalent to a 180° rotation of the nanoparticles. At 50%, it is a combination of the too. The variation of the twin proportion results also in very different graphene rods. Indeed there is in fact both moiré and graphene rods located at these reciprocal space positions and the moiré rods are deeply affected by the twin proportion. The effect of the proportion of twin in the model on the final χ^2 agreement criterion is presented in Fig. 6.6 (a) on the different samples. Whatever the particle type, the χ^2 is found to be minimum for a twin proportion of 50% and is kept at that value in this analysis to limit the number of free parameters. It can be noted that fits of the final model with and without the twins have been done and fits with the twins yields the smaller χ^2 as shown in Fig. 6.6.

Finally, one can note the existence of deep minima of intensity in some places, in particular on the (0,10) rod. Such a minima signals a destructive interference, which is expected to stem from regions of the samples scattering with a 180° phase difference (note that the phase is not accessible to the x-ray diffraction experiments we performed). In Fig. 6.7, the simulations of scattering factors and phases reveal a minimum around L=1.3. By simulating the phase of separate elements of the whole model, it appears that the interference comes from a phase difference of 150-160° between the waves scattered by the nanoparticles and that scattered by graphene instead of the expected 180°. Note that the

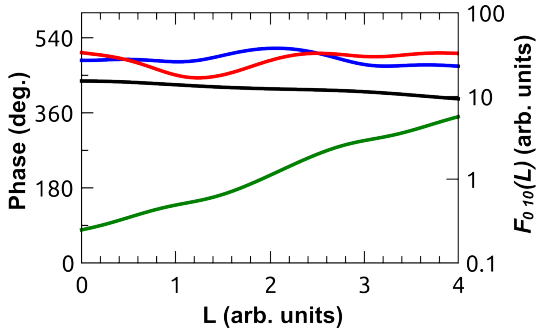

Figure 6.7: On top is displayed simulated structure factors of the (0,10) rod in three different cases, in red is the final result of the Pt_{40} sample fit with the experimental data, in blue is the simulation with just a nanoparticle and in black just graphene. On the bottom is the simulated for the phase difference between the free nanoparticle and graphene in green.

simulations were done on isolated systems, thus in reality, additional external contributions should lead to the phase difference of 180°. This indicates that structural informations from the graphene below the particle will be difficult to obtain with this experimental method, as the major effects observed is the result of interferences from the majority of the graphene, approximately two third, that is away from the particle.

6.3.3 Structure of the Pt_{40} nanoparticles

Let us start with the Pt_{40} nanoparticles. The measured CTRs and rods from the sample with 40 platinum atoms are shown in Fig. 6.8 (a). The structural model is shown in Fig. 6.8 (b), with a three layer truncated pyramidal structure of 37 atoms, slightly smaller than the 40 atoms per sites deposited but respecting the symmetry. A larger width of the bottom layer was tested but did not result in a better fit.

The best fit of the experimental data yields a χ^2 of 7.3. The results are displayed in Fig. 6.8 (b). The occupancy of the bottom and middle layers of the nanoparticle has doubled to $o_{1^{st}} = 75 \pm 2\%$ and $o_{2^{nd}} = 45 \pm 3\%$ respectively and the occupancy of the third layer is $o_{3^{rd}} = 34 \pm 3\%$. This effectively corresponds to

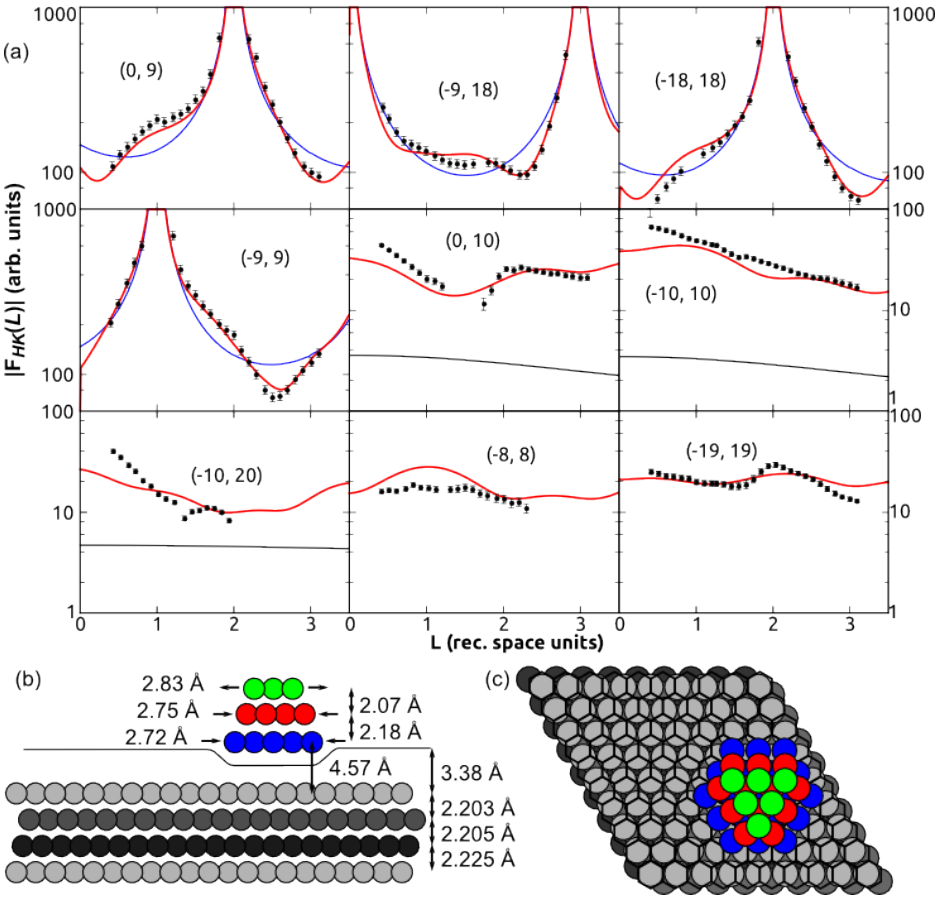

Figure 6.8: (a) Experimental structure factors $|F_{H,K}(L)|$ of the sample with Pt_{40} nanoparticles grown on the graphene measured with SXRD in black with their error bars. The solid red line represents the best fit with the model and the solid blue line represents the CTRs of a perfect bare iridium surface and the solid black line the rods of a perfectly flat graphene layer. (b) Side view of the hard sphere model of the structure of the unit cell of the moiré superlattice with the 37 Pt atoms nanoparticle on top of the hcp region. The iridium atoms of the substrate are shown in grey, with the shades of grey highlighting the ABC stacking, the graphene is shown as a black line to facilitate the reading and the platinum atoms of the nanoparticle are shown in blue for the first layer and red for the second. In addition, the interlayer distances and in-plane strains in the nanoparticle are shown with arrows. (c) Top view of the hard sphere model of the structure of the unit cell of the moiré superlattice with the Pt_{40} atoms nanoparticle on top of the hcp region.

particles of $N_{atoms} = 21.7 \pm 0.9$ atoms, actually $N_{atoms}/N_{deposited} = 54.2 \pm 0.3\%$ of the deposited amount. In addition, the distance between the nanoparticle and the iridium surface is $d_{NP-Ir} = 4.570 \pm 0.003$ Å. The bottom layer and the middle layer are separated by $d_{1-2} = 2.18 \pm 0.04$ Å and the middle and top layer by $d_{2-3} = 2.07 \pm 0.067$ Å, corresponding to contractions of 3.58 ± 1.72 % and 8.49 ± 2.96 %, respectively. Moreover, the layers have in-plane relaxations of $-2.55 \pm 0.10\%$, $-0.79 \pm 0.64\%$ and $1.94 \pm 0.76\%$ with respect to bulk Pt, for the bottom, middle and top layers, with respectively 2.72 ± 0.01 Å, 2.75 ± 0.04 Å 2.83 ± 0.05 Å. Furthermore, the roughness of the substrate surface ρ has also doubled, at 0.75 ± 0.04 Å.

6.3.4 Structure of the Pt_{20} nanoparticles

The model for the nanoparticle here is composed of 25 atoms in a two layer structure. The best fit of the model with the experimental data (Fig. 6.9) has a χ^2 of 7.8 and the structural parameters are displayed in Fig. 6.9 (b). The high value of the χ^2 comes mostly from the poor agreement between the model and the data at low L-values in the (0,10) and (-10,10) graphene rods. The distance between the nanoparticle and the surface is $d_{NP-Ir} = 4.46 \pm 0.01$ Å. The interlayer distance inside the nanoparticle d_{1-2} shows a contraction of 1 % compared to the bulk, at 2.13 ± 0.08 Å. Moreover, the contraction occurs also in-plane, as the bottom layer is contracted by $3.42 \pm 0.14\%$ with respect to bulk Pt at $a_{Pt} = 2.68 \pm 0.01$ Å and the top layer by $1.99 \pm 0.45\%$ at $a_{Pt} = 2.72 \pm 0.03$ Å. The occupancy of the bottom layer $o_{1^{st}}$ is $38 \pm 0.1\%$ and that of the second layer $o_{2^{nd}}$ is $17 \pm 0.2\%$, corresponding to $N_{atoms} = 8.2 \pm 0.3$ atoms per particles, *i.e.* only $N_{atoms}/N_{deposited} = 41.2 \pm 0.2\%$ of the deposited amount. Finally, the roughness ρ of the substrate surface is evaluated to 0.36 ± 0.02 Å.

6.3.5 Structure of the $Co_{20}Pt_{20}$ nanoparticles

Finally, the CTRs and rods from the third sample with bimetallic nanoparticles, formed using the previous 20 platinum atoms nanoparticles and further

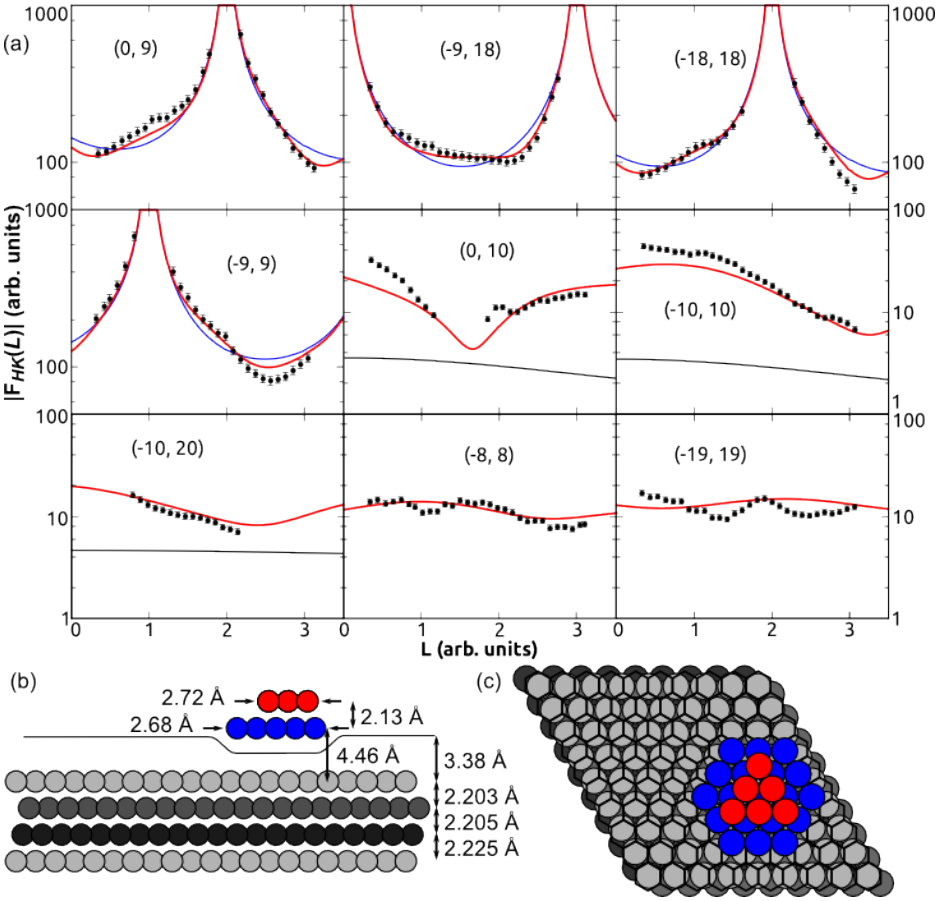

Figure 6.9: (a) Experimental structure factors $|F_{H,K}(L)|$ of the sample with Pt_{20} nanoparticles grown on the graphene measured with SXRD in black disks with error bars. The solid red line represents the best fit with the model, the solid blue line represents the CTRs of a perfect bare iridium surface and the solid black line the rods of a perfectly flat graphene layer. (b) Side view of the hard sphere model of the structure of the unit cell of the moiré superlattice with the Pt_{20} nanoparticle on top of the hcp region. The iridium atoms of the substrate are shown in grey, with the shades of grey highlighting the ABC stacking, the graphene is shown as a black line to facilitate the reading and the platinum atoms of the nanoparticle are shown in blue for the first layer and red for the second. In addition, the interlayer distances and in-plane strains in the nanoparticle are shown with arrows.

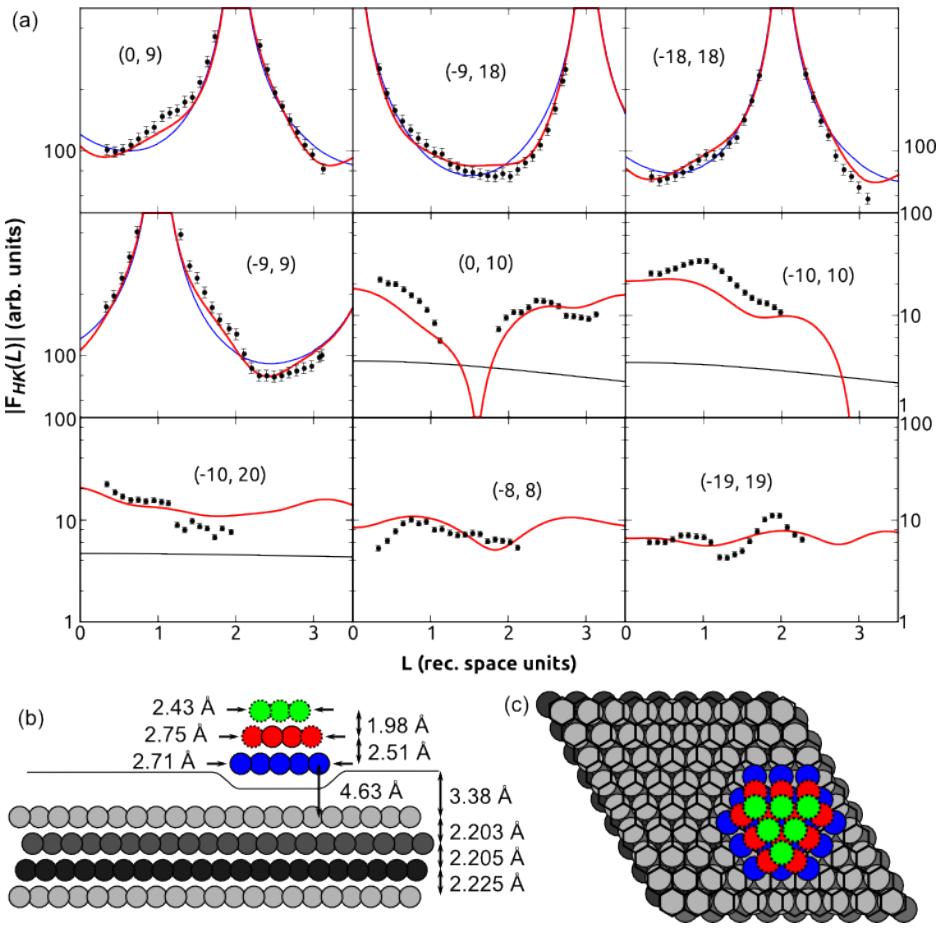

Figure 6.10: (a) Experimental structure factors $|F_{H,K}(L)|$ of the sample with $Co_{20}Pt_{20}$ bimetallic nanoparticles grown on the graphene measured with SXRD in black with their error bars. The solid red line represents the best fit with the model and the solid blue line represents the CTRs of a perfect bare iridium surface and the solid black line the rods of a perfectly flat graphene layer. (b) Side view of the hard sphere model of the structure of the unit cell of the moiré superlattice with the nanoparticle on top of the hcp region. The iridium atoms of the substrate are shown in grey, with the shades of grey highlighting the ABC stacking, the graphene is shown as a black line to facilitate the reading and the atoms of the nanoparticle are shown in blue for the first layer and red for the second, with platinum atoms with a solid outline and cobalt atoms with a dashed one. In addition, the interlayer distances and in-plane strains in the nanoparticle are shown with arrows.

depositing 20 cobalt atoms per moiré lattice, are shown in Fig. 6.10. These CTRs also show bumps at the same position as the previous samples, thus indicating that there are still organised nanoparticles on moiré sites. However, by comparison with the previous results, the shape of the CTRs is closer to the Pt_{20} nanoparticle sample than the Pt_{40} one. The previous in-plane measurements also showed a decrease in intensity in the moiré peaks in Fig. 6.2 and this is expected as f_{Co} is smaller than f_{Pt} but there could still be a decrease in the number of organised nanoparticles in addition. A modified model of the 40 Pt nanoparticle was used, keeping the same platinum atoms as the Pt_{20} model and replacing the additional ones of the 40 Pt model by cobalt atoms (shown with dashed outlines in the figure), and thus keeping the same number of free parameters as before. A model with additional cobalt atoms around the bottom platinum layer was also tested but did not improve the fit.

The best fit of the model has a χ^2 of 10.4 and its results are shown in Fig. 6.10 (b). First, the occupancy of the bottom layer $o_{1^{st}}$ is lower than in the previous Pt_{20} nanoparticle sample, at $31 \pm 2\%$, which is the opposite from the second sample, but confirms the prediction made from the shape of the CTRs. The middle and top layer have occupancies of $o_{2^{nd}} = 28 \pm 2\%$ and $o_{3^{rd}} = 10 \pm 4\%$ respectively, of the same order as the Pt_{40} nanoparticle sample. This corresponds to a $N_{Pt} = 7.57 \pm 0.5$ atoms and $N_{Co} = 2.28 \pm 0.36$ atoms, thus $N_{atoms} = 9.85 \pm 0.86$ per particles. The bottom layer is separated by $d_{NP-Ir} = 4.63 \pm 0.06$ Å with the iridium surface, a small increase compared to the 40 Pt nanoparticles. Furthermore, we find a modulation in the interlayer distances, with an increase of 2.43% of the bottom/middle separation at $d_{1-2} = 2.51 \pm 0.06$ Å while in bulk platinum one has 2.271 Å. There are also in-plane relaxations in the layers of the nanoparticles by comparison with the bulk lattices parameters, $-2.36 \pm 0.27\%$, $-0.86 \pm 0.77\%$ and $-3.07 \pm 1.08\%$ respectively for the bottom, middle and top layers at $a_{Pt} = 2.71 \pm 0.02$ Å, $a_{Pt} = 2.75 \pm 0.05$ Å and $a_{Co} = 2.43 \pm 0.07$ Å. It can also be noted that the roughness of the sample is evaluated to be at 1.25 ± 0.03 Å, an increase from the other samples.

6.4 Discussion on the nanoparticles structures

First, we can note that the number of CTRs and rods measured here is lower than what is presented in Ref. [Franz *et al.* , 2013], because of the smaller amount of material deposited (20 and 40 atoms versus 82 per moiré site), making less moiré rods measurable above the noise level on the detector. Moreover, the method used by Franz *etal*. to measure the CTRs and rods is different from the one we used. It consists in a succession of rocking scans at different L values following the rods. This method may be more precise to measure low intensity rods, such as moiré rods, but L-scans are as efficient for CTRs and take less time, with only one scan instead of several. We have higher χ^2 for the best fits in our study. Besides, the χ^2 values could be artificially high due to an underestimation of the uncertainties on the experimental data, which remains to be clarified.

The structural parameters deduced from the fit to the experimental data are summarized in Table 6.1. The Pt_{20} and Pt_{40} nanoparticles show a proportional occupancy of their atomic layers with the deposited amount of atoms, as it doubles with platinum deposition. In Ref. [Franz *et al.* , 2013], it was found that 53 % of the moiré sites were occupied by iridium nanoparticles. Supposing that the occupancy of the first layer is homogeneous, the occupancy of the nucleation sites is equal to that. Thus, with $38 \pm 1\%$ and $75 \pm 2\%$, respectively for Pt_{20} and Pt_{40} samples, this means that platinum self-organises more easily on the moiré superlattice at a lower coverage than iridium. However, the occupancies of the upper layers are lower, but the evolution between the first two samples indicates that with a higher deposition, the occupancies of these layers increase. Therefore, only 44 % of the Pt_{20} nanoparticles have a second layer. This is of the same order of previous similar results shown in Ref. [N'Diaye *et al.* , 2009]. In this work, the sample consisted of 0.25 monolayer of Pt deposited on graphene on Ir(111). By comparison, we have an equivalent of 0.22 monolayer. In particular, the STM image (Fig. 6 (a) of Ref. [N'Diaye *et al.* , 2009]) shows that while a

negligible number of sites are unoccupied and around 5% of the nanoparticles have three layers, 50 % of the nanoparticles have two layers. The major discrepancy is the site occupancies. At such small sizes, the STM analysis can overestimate the width of the nanoparticles Moreover, it is nearly impossible to distinguish with STM particles that are not exactly on top of the hcp sites. The Pt_{40} nanoparticules also exhibit such a height-dependent occupancy, suggesting that 45 % have three layers, 15 % only two and 40 % are monolayers. The refined Pt_{40} sample surface is sketched in Fig. 6.11 By comparison with the Pt_{20}, more sites are occupied but the proportion of nanoparticles with upper layers has only slightly increased, 55 % versus 44 %. There is no STM data to compare this directly with, but one can note that approximately the same amount of tungsten was also deposited in Ref. [N'Diaye *et al.* , 2009] and the result also show a wide variation of height.

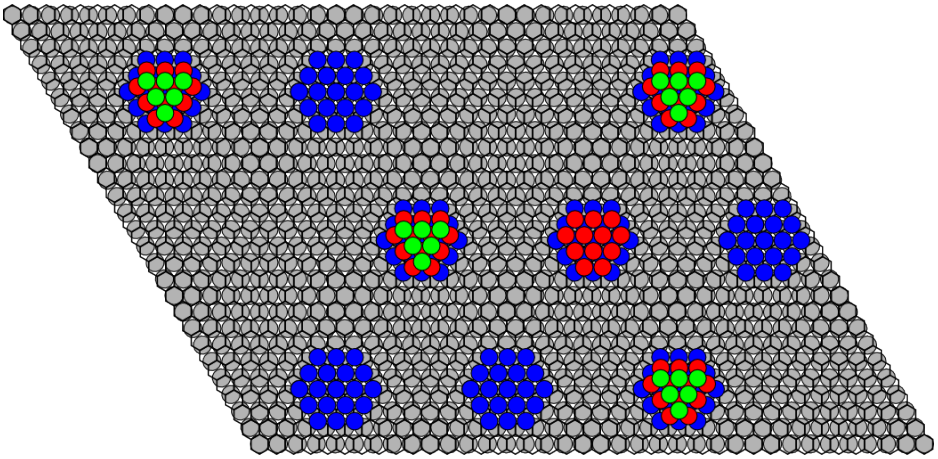

Figure 6.11: (a) Top view of the hard sphere model of the Pt_{40} surface including multiple unit cells of the moiré superlattice with the nanoparticles on top of the hcp region. Only the top atomic layer of iridium substrate is shown in grey, the graphene is shown as black hexagons and the atoms of the nanoparticle are shown in blue for the first layer, red for the second and green for the third.

Let us now discuss the lattice parameters. It was found that there is a contraction of the bottom layer in-plane lattice parameter a_{Pt} for both samples, bringing it at the same order as a_{Ir} or smaller in the case of the smaller particles.

This could be induced by covalent-like bonding with the carbon atoms, which has been argued to accompany a sp^2 to sp^3 rehybridization of carbon beneath the clusters [Feibelman, 2008]. In all three cases, the platinum lattice parameter is observed to be close to that of the iridium substrate, indicating that there is a tendency towards pseudomorphism with the substrate through the graphene, showing the strong interactions between all the elements on the surface. This point was raised before in the chapter and explains also the separation distance between the bottom of the particles and the substrate, corresponding to chemisorption of the particle on the graphene and bonding of the graphene to the substrate. In addition, this chemisorption seems to be modulated depending on the size and nature of the nanoparticle, as its separation with the substrate varies from 4.46 Å for the smaller one to 4.63 Å for the $Co_{20}Pt_{20}$ one. An explanation could be that the smaller nanoparticles have a larger fraction of low-coordinated atoms, for which increasing the interaction with other atoms, e.g. carbon ones, hence reducing interactomic distances, would be favorable. The larger separation observed for the $Co_{20}Pt_{20}$ sample would indicate in this case an enhanced interaction inside the particle also. We suggest that additional experiments such as XPS should be done to explore this further. This would lead to a new way to vary the strength of the superpotential associated with the moiré [Rusponi *et al.* , 2010] with a relatively easy method (atomic deposition), with two parameters, the nanoparticle size that has an observable effect and their nature. However we can note that the difference between pure platinum and the cobalt-platinum here is very small by comparison with the size effect, as the cobalt is not directly in contact with the graphene.

In our case, this also means that a non negligible portion of platinum atoms, approximately half the atoms, are not part of the organised nanoparticles and thus have possibly coalesced into non-monodisperse nanoparticles or have formed well organised nanoparticles positioned slightly off the hcp site for example. This is possibly indicated by the increased apparent surface roughness of the Pt_{40} sample with respect to the Pt_{20} one, as the iridium substrate surface alone

should not have such a dramatic change between the two sample preparation. This brings another issue, as the surface roughness is calculated from the iridium substrate parameters (in and out of plane), and the main effects are observed with the minima on the iridium CTRs. This means that the observed increase is associated to matter having an in-plane lattice parameter similar to that of Ir, such as the bottom layer of the nanoparticles. However, this would not be the case with $Co_{20}Pt_{20}$ particles and we discuss this in the next paragraph.

Concerning the bimetallic nanoparticles sample, we find a decrease of the fraction of sites occupied by nanoparticles, down to $31 \pm 2\%$ from the $38 \pm 1\%$ of the Pt_{20} sample used as a basis. However, in a previous study [Vo-Van *et al.* , 2011], similar bimetallic nanoparticles (13 Pt atoms and 26 Co atoms) were grown on graphene on Ir(111). The quality of the sample was observed to decrease with time as a result of prolonged exposure to synchrotron beam, possibly promoting the decomposition of the graphene by the nanoparticles. The $Co_{20}Pt_{20}$ sample was the longest exposed to the beam during our experiments, which supports this scenario. Additional experiments such as STM would be required to confirm this hypothesis. For now, the seeding method seems only partly successful. The increased apparent roughness of the surface, combined with the lower occupation of moiré sites, is an indication that the coalescence of a part of the nanoparticles occurred, with nanoparticles of various sizes not localised on a specific site of the moiré. High-resolution local probing could confirm this picture, which was observed on graphene on Ru(0001) in Ref. [Liao *et al.* , 2011]. In addition, the STM analysis of the $Co_{26}Pt_{13}$ nanoparticles in Ref. [Vo-Van *et al.* , 2011] shows that 15% of the particles coalesced. This combined to the probable degradation of the sample under the synchrotron beam would explain overall the lower ratio of organised particles on site with the increased roughness of the surface. As for the two other types of nanoparticles, we find strains in the organized nanoparticles. the bottom layer has a contraction of the same order as the pure platinum particles of the same size, thus confirming the tendency of the platinum lattice parameter to shrink to a close match with a_{Ir}.

Parameters	Pt_{20} NPs	Pt_{40} NPs	$Co_{20}Pt_{20}$ NPs
$o_{1^{st}}$	$38 \pm 1\%$	$75 \pm 2\%$	$31 \pm 2\%$
d_{NP-Ir}	4.46 ± 0.01 Å	4.57 ± 0.02 Å	4.63 ± 0.06 Å
1^{st} layer a_{Pt}	2.68 ± 0.01 Å	2.72 ± 0.01 Å	2.71 ± 0.02 Å
$o_{2^{nd}}$	$17 \pm 2\%$	$45 \pm 3\%$	$28 \pm 2\%$
d_{1-2}	2.13 ± 0.07 Å	2.18 ± 0.04 Å	2.51 ± 0.06 Å
2^{nd} layer a_{Pt}	2.72 ± 0.03 Å	2.75 ± 0.04 Å	2.75 ± 0.05 Å
$o_{3^{rd}}$		$34 \pm 3\%$	$10 \pm 4\%$
d_{2-3}		2.07 ± 0.07 Å	1.98 ± 0.01 Å
3^{rd} layer $a_{Pt/Co}$		2.83 ± 0.05 Å	2.43 ± 0.07 Å (a_{Co})
N_{atoms} per nanoparticle	8.24 ± 0.31	21.69 ± 0.92	9.85 ± 0.86
substrate roughness ρ	0.36 ± 0.02 Å	0.75 ± 0.04 Å	1.25 ± 0.03 Å

Table 6.1: Summary of the structural parameters of the nanoparticles in the three samples.

Furthermore, one can note that the nanoparticles are compressed with regards to the interlayer distances and in-plane lattice parameters of each layers. There is one exception : the in-plane lattice parameter a_{Pt} of the top layer in the 40 Pt nanoparticle increases. As we have discussed in this paragraph, the bottom layer in contact with the graphene is strained in-plane. In bulk materials, such an in-plane compression is accompanied by an out-of-plane Poisson-like expansion. The opposite is observed in the platinum nanoparticles, as the interlayer separation is found to decrease. In the case of the largest in-plane a_{Pt} on the Pt_{40} sample, where it has increased to 2.83 Å, the Poisson-like expansion would only have been a reduction of the out-of plane distance to 2.17 Å instead of the 2.07 Å observed. To explain the results, other possible effects may be considered. One would be the surface stress, an effect observed on crystalline free surfaces that can lead to overdensification of atomic layers and even reconstructions, like for the Au(111) surface [Barth *et al.* , 1990]. The contraction due to surface stress has also been studied and observed in nanoparticles of various nature for a large variety of metals (including platinum) [Jiang *et al.* , 2001], which form particles experiencing increasing effective compressive strain as their size decreases. A model was introduced that agrees with experimental data and it predicts a sharp increase of strain below 5 nm for platinum. There are however

no experimental data for platinum below 5 nm to confirm this dramatic effect and thus it is not possible to compare directly our results to previous experimental results. However, if that is confirmed by further experimental results on platinum, like it was for gold and copper. The values reported for these latter metals are comparable with our results of up to 3.42 % compressive strain for a_{Pt} on the bottom layer of the Pt_{20} nanoparticle, and are in accordance with the tendency of the model. Growing nanoparticles on graphene could even lead to new specific models, as nanoparticles are strongly affected by their interaction with the substrate. Finally, it would be interesting to test the model of Ref. [Jiang *et al.* , 2001] with more complex systems, such as bimetallic particles, as the atomic arrangement such as layer ordering should have a dramatic effects at such small scales.

6.5 Conclusion

In this chapter, we have observed the self-organisation of platinum on the moiré superlattice of graphene on Ir(111), with two different sizes of particles and the partial organisation of bimetallic nanoparticles made of a seed of platinum and cobalt. The occupancy of moiré sites by platinum nanoparticles increases with the amount of atoms deposited on the surface and is comparable to the occupancy deduced from a similar study for larger iridium nanoparticles. The atomic structure of the organised nanoparticles was determined by SXRD. The nanoparticles show compressive strains, which we interpret as arising from surface stress due to their small size. Also, depending on the size, their interaction with the graphene, as revealed through the distance between the particles and the substrate, varies, as seemingly stronger bonding occurs for smaller particles. In addition, the distance between the nanoparticles and the substrate is found to decrease with decreasing nanoparticle size, which we interpret as due to a stronger interaction with and through the sandwiched graphene layer. This variation of interaction can be compared to the variation of the graphene

interaction with the substrate material, but with the nanoparticle size as the major factor instead of the nature of the metal. In addition, it was observed that it is possible to obtain bimetallic nanoparticles but with a lower ratio than pure platinum ones, with the possibility that the beam induces damage in the sample by a catalytic reaction. To clarify these open questions, STM imaging before and after beam-time (not available unfortunately in the UHV system we used) should give valuable insights. In the future, one could look to other possible methods to obtain a better yield or use larger particles, such as preformed nanoparticles on the graphene. In addition, a study of the catalytic effects of the various nanoparticles would be interesting for various domains.

Chapter 7

Conclusion

7.1 General conlusion

We chose the moiré-like nanopattern between graphene and the (111) surface of iridium as a playground to address the structure and formation of self-organized two-dimensional lattices of metal nanoparticles. This choice was motivated by the high order and well-defined crystallographic orientation of graphene, the moiré-like nanopattern, and the cluster lattices, which makes the system ideally suited to a high resolution, ensemble averaging surface-sensitive probes as surface scattering - surface X-ray diffraction, grazing incidence X-ray diffraction, X-ray reflectivity, and reflection-high energy electron diffraction. The first step in our study was to determine the structure of graphene and of the nanopattern. We found that the system has a tendency to commensurability, but that the precise structure depends on temperature and on preparation conditions. We also provided high accuracy characterization about the debated structure of graphene perpendicular to the surface. The system, as expected, exhibits a high degree of order, which is only partly inherited by the nanoparticle lattices grown on top - these lattices however show very high degree of order, probably higher than other systems which had been studied thus far by X-ray scattering. We found that the nanoparticles strongly bond to their support, ex-

perience substantial surface strain related to their small size, and that bimetallic ones grown in a sequential manner retain a chemically layered structure.

In the first chapter, the main questions devoted to metallic nanoparticles and their (potential) applications over more than two decades in various domains was first discussed. We highlight the high degree of order which is only achievable in nanoparticle assemblies with bottom-up preparation techniques, and discuss the interest of atomic deposition onto surfaces in this respect, especially of graphene/metal moiré-like patterns. We briefly survey the desirable features that such systems exhibit, in terms of high order, variety of accessible systems, and potential applications, especially in view of nanomagnetism and nanocatalysis.

Chapter 2 addresses the various methods to grow graphene on metals in ultra-high vacuum conditions. The growth methods and the temperature in particular are important as they influence the final structure of the graphene. The graphene structure is primarily affected by the nature of the metallic substrate, *i.e.* by the nature of the metal-graphene interaction, which varies from chemisorption to physisorption depending on the metal. In addition, structural modulations along of the superlattice, caused by the lattices mismatch of the metal and graphene similar to a moiré effect, is dependant on that interaction. Various defects, some typical of membranes (wrinkles), some often encountered in metallurgy (grain boundaries), others characteristic of sp2-hybridized carbon (vacancies), form in graphene. All these structural features must be considered in order to rationalize other graphene properties, and on the longer term in view of tailoring these properties. High resolution structural probes are needed for these reasons.

Chapter 3 presents the basic key concepts and descriptions allowing for understanding the X-ray diffraction results and analysis. We adopt a pragmatic description, illustrated with the system of interest in the next chapters, graphene on Ir(111). This chapter also deals with the experimental conditions and setup, in particular with the detection methods with a 2D detector and the data pro-

cessing using a specific program, PyRod.

Chapter 4 presents the combination of two studies in relation with the evolution of the commensurability of graphene on Ir(111). On the one hand, it was found with electron diffraction during CVD growth that graphene goes through transitions between commensurate phases as defects density decreases over time. On the other hand, full graphene layer show hysteretical behaviour with large temperature changes. This is due to two competing tendencies : either tending to adopt commensurate phases with its substrate at low and high temperatures or releasing stress by forming or flattening wrinkles. Overall, these results show that a weakly hybridized system that was considered incommensurate in fact tends to commensurability. Finally, the graphene thermal expansion coefficient was found to be positive down to 10 K, showing that the weak interaction with the substrate is still enough to induce substantial in-plane heteroepitaxial stress.

The results presented in Chapter 5 focus on SXRD and specular XRR reflectivity measurements, with the inclusion of the specular rod, of graphene on Ir(111). This technique makes it possible to determine with a high precision the atomic structure in three dimensions of epitaxial graphene and its substrate. Structural parameters such as the out of plane modulation of each atomic layer and the interplanar separations were extracted - which were found to be 0.379 ± 0.044 Å and 3.38 ± 0.04 Å respectively. These precise results were possible due to the disentanglement of the surface roughness of the sample from the modulation due to the graphene/metal interaction. Moreover, the structure was described using a 2D Fourier series model, proving that a small number of parameters can describe a large number of atoms accurately and can be applied to hetero-interface systems.

In the last Chapter, three types of nanoparticles were studied with SXRD : two different sizes of platinum particles (Pt_{20} and Pt_{40}) and a bimetallic one ($Co_{20}Pt_{20}$). Platinum self-organise by itself and seeds of platinum were used for the bimetallic nanoparticles. It was found that the occupancy of moiré sites by platinum nanoparticles increases with the amount of atoms deposited on

the surface and that nanoparticles have compressive strains, probably caused to surface stress due to their small size. Moreover, it was observed that the graphene/nanoparticle interaction varies depending on their size, a stronger interaction seemingly occurring with smaller particles. In the case of bimetallic nanoparticles, it was found that they have less organisation than pure platinum nanoparticles of the same size.

7.2 Perspectives

Graphene on Ir(111), and small metal nanoparticles on graphene/Ir(111), are two challenging systems for X-ray scattering studies. Indeed, the low scattering power of graphene compared to the metallic substrate, its monolayer thickness, and the very small size of the nanoparticles make it difficult to achieve quantitative information in general. We showed that however valuable information can be deduced accordingly that cannot be attained by other techniques. We expect valuable information to be achieved as well for other related systems, graphene-based ones and other kinds of two-dimensional crystals as well.

Regarding graphene-based systems, intercalated ones have received much attention in the past few years, and open questions remain regarding the mechanisms at play during intercalation, regarding the structural changes (of the moiré, of the strain in graphene and of the intercalant) upon intercalation, for which X-ray scattering (including grazing incidence X-ray scattering, not discussed in this thesis, but which we have used during the last three years) will provide valuable insight. Still regarding graphene-based systems, we have recently addressed the study of the structure of pre-formed nanoparticles onto graphene/Ir(111), an original alternative to the systems we discussed in this thesis, which offers the possibility to address larger nanoparticles organized onto the moiré-like graphene/Ir(111) nanopattern.

Other two-dimensional crystals, for instance monolayer transition metal dichalcogenides, could prove better suited than graphene to X-ray scattering studies.

Indeed they comprise heavy elements and consist of 3 atomic layers. They have not been studied yet with high-resolution X-ray scattering and we expect that much could be learnt. In such systems, we might expect, for instance, to develop Fourier-series models of the moiré-like patterns beyond first order, or to identify the elementary processes during growth, or the stoechiometry of these systems, which is aknowledged as critical in the prospect of future applications.

Worth noting is probably the added-value of performing multi-technique characterizations of theses systems, for instance by combining X-ray scattering and scanning probe techniques, an approach which we have recently used to study pre-formed nanoparticles on graphene.

Bibliography

[Agostini & Lamberti, 2011] Agostini, G, & Lamberti, C. 2011. *Characterization of semiconductor heterostructures and nanostructures.*

[Ahniyaz *et al.* , 2007] Ahniyaz, Anwar, Sakamoto, Yasuhiro, & Bergström, Lennart. 2007. Magnetic field-induced assembly of oriented superlattices from maghemite nanocubes. *Proceedings of the National Academy of Sciences*, **104**(45), 17570–17574.

[Alayan *et al.* , 2004] Alayan, R, Arnaud, L, Bourgey, A, Broyer, M, Cottancin, E, Huntzinger, JR, Lermé, J, Vialle, JL, Pellarin, M, & Guiraud, G. 2004. Application of a static quadrupole deviator to the deposition of size-selected cluster ions from a laser vaporization source. *Review of scientific instruments*, **75**(7), 2461–2470.

[Alexander Liddle *et al.* , 2011] Alexander Liddle, J., Gallatin, Gregg M., & Ocola, Leonidas E. 2011. Resist Requirements and Limitations for Nanoscale Electron-Beam Patterning. *MRS Proceedings*, **739**(Feb.), H1.5.

[Als-Nielsen & McMorrow, 2001] Als-Nielsen, J, & McMorrow, D. 2001. *Elements of Modern X-Ray Physics.*

[Altenburg & Berndt, 2014] Altenburg, S J, & Berndt, R. 2014. Local work function and STM tip-induced distortion of graphene on Ir(111). *New Journal of Physics*, **16**(5), 053036.

[Arblaster, 2010] Arblaster, John W. 2010. Crystallographic Properties of Iridium. *Platinum Metals Review*, **54**(2), 93–102.

[Arnoult & McLellan, 1972] Arnoult, William J, & McLellan, Rex B. 1972. The solubility of carbon in rhodium ruthenium, iridium and rhenium. *Scripta Metallurgica*, **6**(10), 1013–1018.

[Bae *et al.* , 2010] Bae, Sukang, Kim, Hyeongkeun, Lee, Youngbin, Xu, Xiangfan, Park, Jae-Sung, Zheng, Yi, Balakrishnan, Jayakumar, Lei, Tian, Kim, Hye Ri, Song, Young Il, Kim, Young-Jin, Kim, Kwang S, Ozyilmaz, Barbaros, Ahn, Jong-Hyun, Hong, Byung Hee, & Iijima, Sumio. 2010. Roll-to-roll production of 30-inch graphene films for transparent electrodes. *Nature nanotechnology*, **5**(8), 574–8.

[Bardotti *et al.* , 2002] Bardotti, L, Prevel, B, Jensen, P, Treilleux, M, Mélinon, P, Perez, A, Gierak, J, Faini, G, & Mailly, D. 2002. Organizing nanoclusters on functionalized surfaces. *Applied surface science*, **191**(1), 205–210.

[Bardotti *et al.* , 2011a] Bardotti, L, Tournus, F, Mélinon, P, Pellarin, M, & Broyer, M. 2011a. Mass-selected clusters deposited on graphite: Spontaneous organization controlled by cluster surface reaction. *Physical Review B*, **83**(3), 035425.

[Bardotti *et al.* , 2011b] Bardotti, L, Tournus, F, Mélinon, P, Pellarin, M, & Broyer, M. 2011b. Self organisation of Pt and Au clusters deposited on graphite: the role of reactivity. *The European Physical Journal D-Atomic, Molecular, Optical and Plasma Physics*, **63**(2), 221–224.

[Barth *et al.* , 1990] Barth, JV, Brune, H, Ertl, G, & Behm, RJ. 1990. Scanning tunneling microscopy observations on the reconstructed Au (111) surface: Atomic structure, long-range superstructure, rotational domains, and surface defects. *Physical Review B*, **42**(15), 9307.

[Batzill, 2012] Batzill, Matthias. 2012. The surface science of graphene: Metal interfaces, CVD synthesis, nanoribbons, chemical modifications, and defects. *Surface Science Reports*, **67**(3-4), 83–115.

[Blanc *et al.* , 2012] Blanc, Nils, Coraux, Johann, Vo-Van, Chi, N'Diaye, Alpha, Geaymond, Olivier, & Renaud, Gilles. 2012. Local deformations and incommensurability of high-quality epitaxial graphene on a weakly interacting transition metal. *Physical Review B*, **86**(23), 235439.

[Blanc *et al.* , 2013] Blanc, Nils, Jean, Fabien, Krasheninnikov, Arkady V., Renaud, Gilles, & Coraux, Johann. 2013. Strains Induced by Point Defects in Graphene on a Metal. *Physical Review Letters*, **111**(8), 085501.

[Bloch, 1985] Bloch, JM. 1985. Angle and index calculations forz-axis' X-ray diffractometer. *Journal of applied crystallography*, 33–36.

[Bollmann & Nissen, 1968] Bollmann, W t, & Nissen, H-U. 1968. A study of optimal phase boundaries: the case of exsolved alkali feldspars. *Acta Crystallographica Section A: Crystal Physics, Diffraction, Theoretical and General Crystallography*, **24**(5), 546–557.

[Boneschanscher *et al.* , 2012] Boneschanscher, Mark P, van der Lit, Joost, Sun, Zhixiang, Swart, Ingmar, Liljeroth, Peter, & Vanmaekelbergh, Daniël. 2012. Quantitative atomic resolution force imaging on epitaxial graphene with reactive and nonreactive AFM probes. *ACS nano*, **6**(11), 10216–21.

[Bonnemann *et al.* , 2000] Bonnemann, H, Brinkmann, R, Britz, P, Endruschat, U, Mortel, R, Paulus, UA, Feldmeyer, GJ, Schmidt, TJ, Gasteiger, HA, & Behm, RJ. 2000. Nanoscopic Pt-bimetal colloids as precursors for PEM fuel cell catalysts. *Journal of New Materials for Electrochemical Systems*, **3**(3), 199–206.

[Bower *et al.* , 2000] Bower, Chris, Zhou, Otto, Zhu, Wei, Werder, DJ, & Jin, Sungho. 2000. Nucleation and growth of carbon nanotubes by microwave plasma chemical vapor deposition. *Applied Physics Letters*, **77**(17), 2767–2769.

[Brennan & Eisenberger, 1984] Brennan, S, & Eisenberger, P. 1984. A novel X-ray scattering diffractometer for studying surface structures under UHV conditions. *Nuclear Instruments and Methods in Physics ...*, **222**, 164–167.

[Burnside *et al.* , 1998] Burnside, Shelly D, Shklover, Valery, Barbé, Christophe, Comte, Pascal, Arendse, Francine, Brooks, Keith, & Grätzel, Michael. 1998. Self-organization of TiO2 nanoparticles in thin films. *Chemistry of materials*, **10**(9), 2419–2425.

[Busse *et al.* , 2011] Busse, Carsten, Lazić, Predrag, Djemour, Rabie, Coraux, Johann, Gerber, Timm, Atodiresei, Nicolae, Caciuc, Vasile, Brako, Radovan, N'Diaye, Alpha, Blügel, Stefan, Zegenhagen, Jörg, & Michely, Thomas. 2011. Graphene on Ir(111): Physisorption with Chemical Modulation. *Physical Review Letters*, **107**(3), 036101.

[Charrier *et al.* , 2002] Charrier, A., Coati, A., Argunova, T., Thibaudau, F., Garreau, Y., Pinchaux, R., Forbeaux, I., Debever, J.-M., Sauvage-Simkin, M., & Themlin, J.-M. 2002. Solid-state decomposition of silicon carbide for growing ultra-thin heteroepitaxial graphite films. *Journal of Applied Physics*, **92**(5), 2479.

[Coraux *et al.* , 2008] Coraux, Johann, N'Diaye, Alpha T, Busse, Carsten, & Michely, Thomas. 2008. Structural coherency of graphene on Ir(111). *Nano letters*, **8**(2), 565–70.

[Coraux *et al.* , 2009] Coraux, Johann, Engler, Martin, Busse, Carsten, Wall, Dirk, Buckanie, Niemma, Zu Heringdorf, Frank-J Meyer, Van Gastel, Raoul, Poelsema, Bene, Michely, Thomas, *et al.* . 2009. Growth of graphene on Ir (111). *New Journal of Physics*, **11**(2), 023006.

[Coraux *et al.* , 2012] Coraux, Johann, N'Diaye, Alpha T, Rougemaille, Nicolas, Vo-Van, Chi, Kimouche, Amina, Yang, Hong-Xin, Chshiev, Mairbek, Bendiab, Nedjma, Fruchart, Olivier, & Schmid, Andreas K. 2012. Air-protected epitaxial graphene/ferromagnet hybrids prepared by chemical vapor deposition and intercalation. *The Journal of Physical Chemistry Letters*, **3**(15), 2059–2063.

[Dedkov & Voloshina, 2014] Dedkov, Yuriy, & Voloshina, Elena. 2014. Multichannel scanning probe microscopy and spectroscopy of graphene moiré structures. *Physical chemistry chemical physics : PCCP*, **16**(9), 3894–908.

[Dong *et al.* , 2012] Dong, G C, van Baarle, D W, Rost, M J, & Frenken, J W M. 2012. Graphene formation on metal surfaces investigated by in-situ scanning tunneling microscopy. *New Journal of Physics*, **14**(5), 053033.

[Donner & Jakob, 2009] Donner, Kerstin, & Jakob, Peter. 2009. Structural properties and site specific interactions of Pt with the graphene/Ru (0001) moiré overlayer. *The Journal of chemical physics*, **131**(16), 164701.

[Drnec *et al.* , 2014] Drnec, Jakub, Zhou, Tao, Pintea, Stelian, Onderwaater, Willem, Vlieg, Elias, Renaud, Gilles, & Felici, Roberto. 2014. Integration techniques for surface X-ray diffraction data obtained with a two-dimensional detector. *Journal of Applied Crystallography*, **47**(1), 365–377.

[Fanton *et al.* , 2011] Fanton, Mark a, Robinson, Joshua a, Puls, Conor, Liu, Ying, Hollander, Matthew J, Weiland, Brian E, Labella, Michael, Trumbull, Kathleen, Kasarda, Richard, Howsare, Casey, Stitt, Joseph, & Snyder, David W. 2011. Characterization of graphene films and transistors grown on sapphire by metal-free chemical vapor deposition. *ACS nano*, **5**(10), 8062–9.

[Feibelman, 2008] Feibelman, Peter J. 2008. Pinning of graphene to Ir (111) by flat Ir dots. *Physical Review B*, **77**(16), 165419.

[Felter & Weinberg, 1981] Felter, TE, & Weinberg, WH. 1981. A model of ethylene and acetylene adsorption on the (111) surfaces of platinum and nickel. *Surface Science*, **103**(1), 265–287.

[Forbeaux *et al.* , 1998] Forbeaux, I, Themlin, J-M, & Debever, J-M. 1998. Heteroepitaxial graphite on 6 H-SiC (0001): Interface formation through conduction-band electronic structure. *Physical Review B*, **58**(24), 16396.

[Franz *et al.* , 2013] Franz, D, Runte, S, Busse, C, Schumacher, S, Gerber, T, Michely, T, Mantilla, M, Kilic, V, Zegenhagen, J, & Stierle, A. 2013. Atomic Structure and Crystalline Order of Graphene-Supported Ir Nanoparticle Lattices. *Physical review letters*, **110**(6), 065503.

[Fruchart *et al.* , 2003] Fruchart, O, Renaud, G, Barbier, A, Noblet, M, Ulrich, O, Deville, J-P, Scheurer, F, Mane-Mane, J, Repain, V, Baudot, G, *et al.* . 2003. X-ray super-cell crystallography of self-organized Co/Au (111) deposits. *EPL (Europhysics Letters)*, **63**(2), 275.

[Fuoss & Robinson, 1984] Fuoss, PH, & Robinson, IK. 1984. Apparatus for x-ray diffraction in ultrahigh vacuum. *Nuclear Instruments and Methods in Physics ...*, **222**, 171–176.

[Gao *et al.* , 2012] Gao, Libo, Ren, Wencai, Xu, Huilong, Jin, Li, Wang, Zhenxing, Ma, Teng, Ma, Lai-Peng, Zhang, Zhiyong, Fu, Qiang, Peng, Lian-Mao, Bao, Xinhe, & Cheng, Hui-Ming. 2012. Repeated growth and bubbling transfer of graphene with millimetre-size single-crystal grains using platinum. *Nature communications*, **3**(Jan.), 699.

[Gao *et al.* , 2011] Gao, M., Pan, Y., Huang, L., Hu, H., Zhang, L. Z., Guo, H. M., Du, S. X., & Gao, H.-J. 2011. Epitaxial growth and structural property of graphene on Pt(111). *Applied Physics Letters*, **98**(3), 033101.

[Gerber *et al.* , 2013] Gerber, Timm, Knudsen, Jan, Feibelman, Peter J, Granas, Elin, Stratmann, Patrick, Schulte, Karina, Andersen, Jesper N, & Michely, Thomas. 2013. CO-Induced Smoluchowski Ripening of Pt Cluster Arrays on the Graphene/Ir (111) Moire´. *ACS nano*, **7**(3), 2020–2031.

[Geringer *et al.* , 2009] Geringer, V, Liebmann, M, Echtermeyer, T, Runte, S, Schmidt, M, Rückamp, R, Lemme, Max C, & Morgenstern, M. 2009. Intrinsic and extrinsic corrugation of monolayer graphene deposited on SiO 2. *Physical review letters*, **102**(7), 076102.

[Granas *et al.* , 2012] Granas, Elin, Knudsen, Jan, Schröder, Ulrike a, Gerber, Timm, Busse, Carsten, Arman, Mohammad a, Schulte, Karina, Andersen, Jesper N, & Michely, Thomas. 2012. Oxygen intercalation under graphene

on Ir(111): energetics, kinetics, and the role of graphene edges. *ACS nano*, **6**(11), 9951–63.

[Granas *et al.* , 2013] Granas, Elin, Andersen, Mie, Arman, Mohammad A, Gerber, Timm, Hammer, Bjørk, Schnadt, Joachim, Andersen, Jesper N, Michely, Thomas, & Knudsen, Jan. 2013. CO intercalation of graphene on Ir (111) in the millibar regime. *The Journal of Physical Chemistry C*, **117**(32), 16438–16447.

[Guo *et al.* , 2009] Guo, Shaojun, Dong, Shaojun, & Wang, Erkang. 2009. Three-dimensional Pt-on-Pd bimetallic nanodendrites supported on graphene nanosheet: facile synthesis and used as an advanced nanoelectrocatalyst for methanol oxidation. *Acs Nano*, **4**(1), 547–555.

[Hall & Crangle, 1957] Hall, E. O., & Crangle, J. 1957. An X-ray investigation of the reported high-temperature allotropy of ruthenium. *Acta Crystallographica*, **10**(3), 240–241.

[Hämäläinen *et al.* , 2013] Hämäläinen, Sampsa K., Boneschanscher, Mark P., Jacobse, Peter H., Swart, Ingmar, Pussi, Katariina, Moritz, Wolfgang, Lahtinen, Jouko, Liljeroth, Peter, & Sainio, Jani. 2013. Structure and local variations of the graphene moiré on Ir(111). *Physical Review B*, **88**(20), 201406.

[Hannour *et al.* , 2005] Hannour, A, Bardotti, L, Prevel, B, Bernstein, E, Melinon, P, Perez, A, Gierak, J, Bourhis, E, & Mailly, D. 2005. 2D arrays of CoPt nanocluster assemblies. *Surface science*, **594**(1), 1–11.

[Haruta, 1997] Haruta, Masatake. 1997. Size-and support-dependency in the catalysis of gold. *Catalysis Today*, **36**(1), 153–166.

[Hattab *et al.* , 2011] Hattab, H., N'Diaye, a. T., Wall, D., Jnawali, G., Coraux, J., Busse, C., van Gastel, R., Poelsema, B., Michely, T., Meyer zu Heringdorf, F.-J., & Horn-von Hoegen, M. 2011. Growth temperature dependent graphene alignment on Ir(111). *Applied Physics Letters*, **98**(14), 141903.

[Hattab *et al.* , 2012] Hattab, Hichem, N'Diaye, Alpha T, Wall, Dirk, Klein, Claudius, Jnawali, Giriraj, Coraux, Johann, Busse, Carsten, van Gastel, Raoul, Poelsema, Bene, Michely, Thomas, zu Heringdorf, Frank-J Meyer, & Horn-von Hoegen, Michael. 2012. Interplay of wrinkles, strain, and lattice parameter in graphene on iridium. *Nano letters*, **12**(2), 678–82.

[Henzie *et al.* , 2013] Henzie, Joel, Andrews, Sean C, Ling, Xing Yi, Li, Zhiyong, & Yang, Peidong. 2013. Oriented assembly of polyhedral plasmonic nanoparticle clusters. *Proceedings of the National Academy of Sciences*, **110**(17), 6640–6645.

[Huang *et al.* , 2013] Huang, Xiao, Zeng, Zhiyuan, Bao, Shuyu, Wang, Mengfei, Qi, Xiaoying, Fan, Zhanxi, & Zhang, Hua. 2013. Solution-phase epitaxial growth of noble metal nanostructures on dispersible single-layer molybdenum disulfide nanosheets. *Nature Communications*, **4**, 1444.

[Huang *et al.* , 2006] Huang, Xiaohua, El-Sayed, Ivan H, Qian, Wei, & El-Sayed, Mostafa A. 2006. Cancer cell imaging and photothermal therapy in the near-infrared region by using gold nanorods. *Journal of the American Chemical Society*, **128**(6), 2115–2120.

[Hu¨lsen, 2004] Hu¨lsen, G. 2004. Pixel Detectors For Diffraction Experiments At The Swiss Light Source. *AIP Conference Proceedings*, **705**(2004), 1009–1012.

[Ibach, 1997] Ibach, Harald. 1997. The role of surface stress in reconstruction, epitaxial growth and stabilization of mesoscopic structures. *Surface science reports*, **29**(5), 195–263.

[Isett & Blakely, 1976] Isett, LC, & Blakely, JM. 1976. Segregation isosteres for carbon at the (100) surface of nickel. *Surface Science*, **58**, 397–414.

[Jean *et al.* , 2013] Jean, Fabien, Zhou, Tao, Blanc, Nils, Felici, Roberto, Coraux, Johann, & Renaud, Gilles. 2013. Effect of preparation on the commensurabilities and thermal expansion of graphene on Ir (111) between 10 and 1300 K. *Physical Review B*, **88**(16), 165406.

[Jiang *et al.* , 2001] Jiang, Q, Liang, LH, & Zhao, DS. 2001. Lattice contraction and surface stress of fcc nanocrystals. *The Journal of Physical Chemistry B*, **105**(27), 6275–6277.

[Jonsson, 2004] Jonsson, Petra E. 2004. Superparamagnetism and spin glass dynamics of interacting magnetic nanoparticle systems. *Advances in Chemical Physics*, **128**, 191–248.

[Kim *et al.* , 2009] Kim, Keun Soo, Zhao, Yue, Jang, Houk, Lee, Sang Yoon, Kim, Jong Min, Kim, Kwang S, Ahn, Jong-hyun, Kim, Philip, Choi, Jae-young, & Hong, Byung Hee. 2009. Large-scale pattern growth of graphene films for stretchable transparent electrodes. *Nature*, **457**(7230), 706–10.

[Kimouche *et al.* , 2014] Kimouche, Amina, Renault, Olivier, Samaddar, Sayanti, Winkelmann, Clemens, Courtois, Hervé, Fruchart, Olivier, & Coraux, Johann. 2014. Modulating charge density and inelastic optical response in graphene by atmospheric pressure localized intercalation through wrinkles. *Carbon*, **68**(Mar.), 73–79.

[Koma, 1992] Koma, Atsushi. 1992. Van der Waals epitaxy—a new epitaxial growth method for a highly lattice-mismatched system. *Thin Solid Films*, **216**(1), 72 – 76. Papers presented at the International Workshop on Science and Technology of Thin Films for the 21st Century, Evanston,IL, USA, July 28-August 2, 1991.

[Krasheninnikov & Nieminen, 2011] Krasheninnikov, AV, & Nieminen, RM. 2011. Attractive interaction between transition-metal atom impurities and vacancies in graphene: a first-principles study. *Theoretical Chemistry Accounts*, **129**(3-5), 625–630.

[Kreibig & Vollmer, 1995] Kreibig, Uwe, & Vollmer, Michael. 1995. Optical properties of metal clusters.

[Lacovig *et al.* , 2009] Lacovig, Paolo, Pozzo, Monica, Alfè, Dario, Vilmercati, Paolo, Baraldi, Alessandro, & Lizzit, Silvano. 2009. Growth of Dome-Shaped Carbon Nanoislands on Ir(111): The Intermediate between Carbidic Clusters and Quasi-Free-Standing Graphene. *Physical Review Letters*, **103**(16), 166101.

[Land *et al.* , 1992] Land, TA, Michely, Th, Behm, RJ, Hemminger, JC, & Comsa, G. 1992. STM investigation of single layer graphite structures produced on Pt (111) by hydrocarbon decomposition. *Surface Science*, **264**(3), 261–270.

[Leake *et al.* , 2014] Leake, Steven J., Reinle-Schmitt, Mathilde L., Kalichava, Irakli, Pauli, Stephan a., & Willmott, Philip R. 2014. Cluster method for analysing surface X-ray diffraction data sets using area detectors. *Journal of Applied Crystallography*, **47**(1), 207–214.

[Lee *et al.* , 2014] Lee, Jae-Hyun, Lee, Eun Kyung, Joo, Won-Jae, Jang, Yamujin, Kim, Byung-Sung, Lim, Jae Young, Choi, Soon-Hyung, Ahn, Sung Joon, Ahn, Joung Real, Park, Min-Ho, Yang, Cheol-Woong, Choi, Byoung Lyong, Hwang, Sung-Woo, & Whang, Dongmok. 2014. Wafer-scale growth of single-crystal monolayer graphene on reusable hydrogen-terminated germanium. *Science (New York, N.Y.)*, **344**(6181), 286–9.

[Lemire *et al.* , 2004] Lemire, Céline, Meyer, Randall, Shaikhutdinov, Sh K, & Freund, H-J. 2004. CO adsorption on oxide supported gold: from small clusters to monolayer islands and three-dimensional nanoparticles. *Surface Science*, **552**(1), 27–34.

[Li *et al.* , 2009] Li, Xuesong, Cai, Weiwei, An, Jinho, Kim, Seyoung, Nah, Junghyo, Yang, Dongxing, Piner, Richard, Velamakanni, Aruna, Jung, Inhwa, Tutuc, Emanuel, Banerjee, Sanjay K, Colombo, Luigi, & Ruoff, Rodney S. 2009. Large-area synthesis of high-quality and uniform graphene films on copper foils. *Science (New York, N.Y.)*, **324**(5932), 1312–4.

[Li *et al.* , 2011a] Li, Xuesong, Magnuson, Carl W, Venugopal, Archana, Tromp, Rudolf M, Hannon, James B, Vogel, Eric M, Colombo, Luigi, & Ruoff, Rodney S. 2011a. Large-area graphene single crystals grown by low-pressure chemical vapor deposition of methane on copper. *Journal of the American Chemical Society*, **133**(9), 2816–2819.

[Li *et al.* , 2011b] Li, Zhancheng, Wu, Ping, Wang, Chenxi, Fan, Xiaodong, Zhang, Wenhua, Zhai, Xiaofang, Zeng, Changgan, Li, Zhenyu, Yang, Jinlong, & Hou, Jianguo. 2011b. Low-temperature growth of graphene by chemical vapor deposition using solid and liquid carbon sources. *ACS nano*, **5**(4), 3385–90.

[Liao *et al.* , 2011] Liao, Q, Zhang, HJ, Wu, K, Li, HY, Bao, SN, & He, P. 2011. Nucleation and growth of monodispersed cobalt nanoclusters on graphene moire on Ru (0001). *Nanotechnology*, **22**(12), 125303.

[Liu *et al.* , 2002] Liu, Shantang, Zhu, Tao, Hu, Ruisheng, & Liu, Zhongfan. 2002. Evaporation-induced self-assembly of gold nanoparticles into a highly organized two-dimensional array. *Phys. Chem. Chem. Phys.*, **4**(24), 6059–6062.

[Loginova *et al.* , 2009a] Loginova, E, Bartelt, N C, Feibelman, P J, & McCarty, K F. 2009a. Factors influencing graphene growth on metal surfaces. *New Journal of Physics*, **11**(6), 063046.

[Loginova *et al.* , 2009b] Loginova, Elena, Nie, Shu, Thürmer, Konrad, Bartelt, Norman, & McCarty, Kevin. 2009b. Defects of graphene on Ir(111): Rotational domains and ridges. *Physical Review B*, **80**(8), 085430.

[Marchini *et al.* , 2007] Marchini, S., Günther, S., & Wintterlin, J. 2007. Scanning tunneling microscopy of graphene on Ru(0001). *Physical Review B*, **76**(7), 075429.

[Marinova & Kostov, 1987] Marinova, Ts.S, & Kostov, K.L. 1987. Adsorption of acetylene and ethylene on a clean Ir(111) surface. *Surface Science*, **181**(3), 573–585.

[Martoccia *et al.* , 2008] Martoccia, D., Willmott, P., Brugger, T., Björck, M., Günther, S., Schlepütz, C., Cervellino, a., Pauli, S., Patterson, B., Marchini, S., Wintterlin, J., Moritz, W., & Greber, T. 2008. Graphene on Ru(0001): A 25×25 Supercell. *Physical Review Letters*, **101**(12), 126102.

[Martoccia *et al.* , 2010] Martoccia, D, Björck, M, Schlepütz, C M, Brugger, T, Pauli, S a, Patterson, B D, Greber, T, & Willmott, P R. 2010. Graphene on Ru(0001): a corrugated and chiral structure. *New Journal of Physics*, **12**(4), 043028.

[Massies & Grandjean, 1993] Massies, J, & Grandjean, N. 1993. Oscillation of the lattice relaxation in layer-by-layer epitaxial growth of highly strained materials. *Physical review letters*, **71**(9), 1411.

[Matsumoto & Ogura, 2007] Matsumoto, M, & Ogura, S. 2007. Dynamical low-energy electron diffraction analyses of clean and H-adsorbed Ir (111) surfaces. *Journal of the Vacuum Society of Japan*, **49**(5), 43–46.

[McCarty *et al.* , 2009] McCarty, Kevin F., Feibelman, Peter J., Loginova, Elena, & Bartelt, Norman C. 2009. Kinetics and thermodynamics of carbon segregation and graphene growth on Ru(0001). *Carbon*, **47**(7), 1806–1813.

[Meng *et al.* , 2012] Meng, Lei, Wu, Rongting, Zhang, Lizhi, Li, Linfei, Du, Shixuan, Wang, Yeliang, & Gao, H-J. 2012. Multi-oriented moiré superstructures of graphene on Ir(111): experimental observations and theoretical models. *Journal of physics. Condensed matter : an Institute of Physics journal*, **24**(31), 314214.

[Milani *et al.* , 1990] Milani, Paolo, *et al.* . 1990. Improved pulsed laser vaporization source for production of intense beams of neutral and ionized clusters. *Review of scientific instruments*, **61**(7), 1835–1838.

[Mittendorfer *et al.* , 2011] Mittendorfer, F., Garhofer, A., Redinger, J., Klimeš, J., Harl, J., & Kresse, G. 2011. Graphene on Ni(111): Strong interaction and weak adsorption. *Physical Review B*, **84**(20), 201401.

[Moritz *et al.* , 2010] Moritz, W., Wang, B., Bocquet, M.-L., Brugger, T., Greber, T., Wintterlin, J., & Günther, S. 2010. Structure Determination of the Coincidence Phase of Graphene on Ru(0001). *Physical Review Letters*, **104**(13), 136102.

[Mounet & Marzari, 2005] Mounet, Nicolas, & Marzari, Nicola. 2005. First-principles determination of the structural, vibrational and thermodynamic properties of diamond, graphite, and derivatives. *Physical Review B*, **71**(20), 1–14.

[Murata *et al.* , 2010] Murata, Y., Starodub, E., Kappes, B. B., Ciobanu, C. V., Bartelt, N. C., McCarty, K. F., & Kodambaka, S. 2010. Orientation-dependent work function of graphene on Pd(111). *Applied Physics Letters*, **97**(14), 143114.

[N'Diaye *et al.* , 2006] N'Diaye, Alpha T., Bleikamp, Sebastian, Feibelman, Peter J, Michely, Thomas, *et al.* . 2006. Two-dimensional Ir cluster lattice on a graphene moiré on Ir (111). *Physical Review Letters*, **97**(21), 215501.

[N'Diaye *et al.* , 2008] N'Diaye, Alpha T, Coraux, Johann, Plasa, Tim N, Busse, Carsten, & Michely, Thomas. 2008. Structure of epitaxial graphene on Ir(111). *New Journal of Physics*, **10**(4), 043033.

[N'Diaye *et al.* , 2009] N'Diaye, Alpha T., Gerber, Timm, Busse, Carsten, Mysliveček, Josef, Coraux, Johann, Michely, Thomas, *et al.* . 2009. A versatile fabrication method for cluster superlattices. *New Journal of Physics*, **11**(10), 103045.

[Nelson & Riley, 1945] Nelson, JB, & Riley, DP. 1945. The thermal expansion of graphite from 15 c. to 800 c.: Part I. Experimental. *Proceedings of the Physical Society*, **57**(6), 477.

[Nesselberger *et al.* , 2013] Nesselberger, Markus, Roefzaad, Melanie, Hamou, R Fayçal, Biedermann, P Ulrich, Schweinberger, Florian F, Kunz, Sebastian, Schloegl, Katrin, Wiberg, Gustav KH, Ashton, Sean, Heiz, Ueli, *et al.* . 2013. The effect of particle proximity on the oxygen reduction rate of size-selected platinum clusters. *Nature materials*, **12**(10), 919–924.

[Neto *et al.* , 2009] Neto, AH Castro, Guinea, F, Peres, NMR, Novoselov, Kostya S, & Geim, Andre K. 2009. The electronic properties of graphene. *Reviews of modern physics*, **81**(1), 109.

[Nguyen *et al.* , 2012] Nguyen, Manh-Thuong, Erni, Rolf, & Passerone, Daniele. 2012. Two-dimensional nucleation and growth mechanism explaining graphene oxide structures. *Physical Review B*, **86**(11), 115406.

[Nie *et al.* , 2011] Nie, Shu, Walter, Andrew L, Bartelt, Norman C, Starodub, Elena, Bostwick, Aaron, Rotenberg, Eli, & McCarty, Kevin F. 2011. Growth from below: Graphene bilayers on Ir (111). *ACS nano*, **5**(3), 2298–2306.

[Nie *et al.* , 2012] Nie, Shu, Bartelt, Norman C., Wofford, Joseph M., Dubon, Oscar D., McCarty, Kevin F., & Thurmer, Konrad. 2012. Scanning tunneling microscopy study of graphene on Au(111): Growth mechanisms and substrate interactions. *Physical Review B*, **85**(20), 205406.

[Nieuwenhuys *et al.* , 1976] Nieuwenhuys, B.E., Hagen, D.I., Rovida, G., & Somorjai, G.A. 1976. LEED, AES and thermal desorption studies of chemisorbed Hydrogen and hydrocarbons (C2H2, C2H4, C6H6, C6H12) on the (111) and stepped [6(111) × (100)] iridium crystal surfaces; comparison with platinum. *Surface Science*, **59**(1), 155–176.

[Odahara *et al.* , 2011] Odahara, Genki, Otani, Shigeki, Oshima, Chuhei, Suzuki, Masahiko, Yasue, Tsuneo, & Koshikawa, Takanori. 2011. In-situ observation of graphene growth on Ni(111). *Surface Science*, **605**(11-12), 1095–1098.

[Otero *et al.* , 2010] Otero, G., González, C., Pinardi, a., Merino, P., Gardonio, S., Lizzit, S., Blanco-Rey, M., Van de Ruit, K., Flipse, C., Méndez, J., de Andrés, P., & Martín-Gago, J. 2010. Ordered Vacancy Network Induced by the Growth of Epitaxial Graphene on Pt(111). *Physical Review Letters*, **105**(21), 1–4.

[Pan *et al.* , 2009] Pan, Yi, Gao, Min, Huang, Li, Liu, Feng, & Gao, H-J. 2009. Directed self-assembly of monodispersed platinum nanoclusters on graphene moiré template. *Applied Physics Letters*, **95**(9), 093106.

[Pletikosić *et al.* , 2009] Pletikosić, I., Kralj, M., Pervan, P., Brako, R., Coraux, J., N'Diaye, A., Busse, C., & Michely, T. 2009. Dirac Cones and Minigaps for Graphene on Ir(111). *Physical Review Letters*, **102**(5), 056808.

[Renaud *et al.* , 2009] Renaud, Gilles, Lazzari, Rémi, & Leroy, Frédéric. 2009. Probing surface and interface morphology with Grazing Incidence Small Angle X-Ray Scattering. *Surface Science Reports*, **64**(8), 255–380.

[Repain *et al.* , 2002] Repain, V, Baudot, G, Ellmer, H, & Rousset, S. 2002. Ordered growth of cobalt nanostructures on a Au (111) vicinal surface: nucleation mechanisms and temperature behavior. *Materials Science and Engineering: B*, **96**(2), 178–187.

[Ritter *et al.* , 1998] Ritter, M, Ranke, W, & Weiss, W. 1998. Growth and structure of ultrathin FeO films on Pt (111) studied by STM and LEED. *Physical Review B*, **57**(12), 7240–7251.

[Robinson, 1986] Robinson, IK. 1986. Crystal truncation rods and surface roughness. *Physical Review B*, **33**(6), 3830–3836.

[Robinson & Tweet, 1992] Robinson, IK, & Tweet, DJ. 1992. Surface x-ray diffraction. *Reports on Progress in Physics*, 599–651.

[Rougemaille *et al.* , 2012] Rougemaille, N., N'Diaye, A. T., Coraux, J., Vo-Van, C., Fruchart, O., & Schmid, A. K. 2012. Perpendicular magnetic anisotropy of cobalt films intercalated under graphene. *Applied Physics Letters*, **101**(14), 142403.

[Rousset *et al.* , 2002] Rousset, S, Repain, V, Baudot, G, Ellmer, H, Garreau, Y, Etgens, V, Berroir, JM, Croset, B, Sotto, M, Zeppenfeld, P, *et al.* . 2002. Self-ordering on crystal surfaces: fundamentals and applications. *Materials Science and Engineering: B*, **96**(2), 169–177.

[Runte *et al.* , 2014] Runte, Sven, Lazić, Predrag, Vo-Van, Chi, Coraux, Johann, Zegenhagen, Jörg, & Busse, Carsten. 2014. Graphene buckles under stress: An x-ray standing wave and scanning tunneling microscopy study. *Physical Review B*, **89**(15), 155427.

[Rusponi *et al.* , 2010] Rusponi, S, Papagno, M, Moras, P, Vlaic, S, Etzkorn, M, Sheverdyaeva, PM, Pacilé, D, Brune, H, & Carbone, C. 2010. Highly anisotropic Dirac cones in epitaxial graphene modulated by an island superlattice. *Physical review letters*, **105**(24), 246803.

[Saito & Ogino, 2014] Saito, Kosuke, & Ogino, Toshio. 2014. Direct Growth of Graphene Films on Sapphire (0001) and (112[U+0305]0) Surfaces by Self-Catalytic Chemical Vapor Deposition. *The Journal of Physical Chemistry C*, **118**(10), 5523–5529.

[Sánchez-Barriga *et al.* , 2013] Sánchez-Barriga, J, Bihlmayer, G, Wortmann, D, Marchenko, D, Rader, O, & Varykhalov, a. 2013. Effect of structural modulation and thickness of a graphene overlayer on the binding energy of the Rashba-type surface state of Ir(111). *New Journal of Physics*, **15**(11), 115009.

[Santis *et al.* , 1999] Santis, M De, Dolle, P, Geaymond, O, Taunier, P, Jeantet, P, Roux, J P, Renaud, G, Barbier, A, Robach, O, Ulrich, O, & Mougin, A. 1999. A new UHV diffractometer for surface structure and real time molecular beam deposition studies with synchrotron radiations at ESRF. *Nuclear Instruments and Methods in Physics Research B*, **149**, 213–227.

[Schlepütz *et al.* , 2005] Schlepütz, C M, Herger, R, Willmott, P R, Patterson, B D, Bunk, O, Brönnimann, Ch, Henrich, B, Hülsen, G, & Eikenberry, E F. 2005. Improved data acquisition in grazing-incidence X-ray scattering experiments using a pixel detector. *Acta crystallographica. Section A, Foundations of crystallography*, **61**(Pt 4), 418–25.

[Schumacher *et al.* , 2013] Schumacher, Stefan, Förster, Daniel, Rösner, Malte, Wehling, Tim, & Michely, Thomas. 2013. Strain in Epitaxial Graphene Visualized by Intercalation. *Physical Review Letters*, **110**(8), 086111.

[Shaikhutdinov *et al.* , 2003] Shaikhutdinov, Sh K, Meyer, Randall, Lahav, Doron, Bäumer, Marcus, Klüner, Thorsten, & Freund, H-J. 2003. Determination of atomic structure of the metal-oxide interface: Pd nanodeposits on an FeO (111) film. *Physical review letters*, **91**(7), 076102.

[Shchukin & Bimberg, 1999] Shchukin, Vitaliy A, & Bimberg, Dieter. 1999. Spontaneous ordering of nanostructures on crystal surfaces. *Reviews of Modern Physics*, **71**(4), 1125.

[Shelton *et al.* , 1974] Shelton, JC, Patil, HR, & Blakely, JM. 1974. Equilibrium segregation of carbon to a nickel (111) surface: A surface phase transition. *Surface Science*, **43**(2), 493–520.

[Shipway *et al.* , 2000] Shipway, Andrew N, Katz, Eugenii, & Willner, Itamar. 2000. Nanoparticle arrays on surfaces for electronic, optical, and sensor applications. *ChemPhysChem*, **1**(1), 18–52.

[Singh *et al.* , 2010] Singh, Vibhor, Sengupta, Shamashis, Solanki, Hari S, Dhall, Rohan, Allain, Adrien, Dhara, Sajal, Pant, Prita, & Deshmukh, Mandar M. 2010. Probing thermal expansion of graphene and modal dispersion at low-temperature using graphene nanoelectromechanical systems resonators. *Nanotechnology*, **21**(16), 165204.

[Song *et al.* , 2012] Song, Hyun Jae, Son, Minhyeok, Park, Chibeom, Lim, Hyunseob, Levendorf, Mark P, Tsen, Adam W, Park, Jiwoong, & Choi, Hee Cheul. 2012. Large scale metal-free synthesis of graphene on sapphire and transfer-free device fabrication. *Nanoscale*, **4**(10), 3050–4.

[Starodub *et al.* , 2011] Starodub, Elena, Bostwick, Aaron, Moreschini, Luca, Nie, Shu, Gabaly, Farid El, McCarty, Kevin F., & Rotenberg, Eli. 2011. In-plane orientation effects on the electronic structure, stability, and Raman scattering of monolayer graphene on Ir(111). *Physical Review B*, **83**(12), 125428.

[Süle & Szendrő, 2014] Süle, P., & Szendrő, M. 2014. The classical molecular dynamics simulation of graphene on Ru(0001) using a fitted Tersoff interface potential. *Surface and Interface Analysis*, **46**(1), 42–47.

[Sun *et al.* , 2004] Sun, Shouheng, Zeng, Hao, Robinson, David B, Raoux, Simone, Rice, Philip M, Wang, Shan X, & Li, Guanxiong. 2004. Monodisperse MFe2O4 (M= Fe, Co, Mn) nanoparticles. *Journal of the American Chemical Society*, **126**(1), 273–279.

[Sun *et al.* , 2011] Sun, Zhixiang, Hämäläinen, Sampsa K., Sainio, Jani, Lahtinen, Jouko, Vanmaekelbergh, Daniël, & Liljeroth, Peter. 2011. Topographic and electronic contrast of the graphene moiré on Ir(111) probed by scanning tunneling microscopy and noncontact atomic force microscopy. *Physical Review B*, **83**(8), 081415.

[Sutter *et al.* , 2009] Sutter, E., Acharya, D. P., Sadowski, J. T., & Sutter, P. 2009. Scanning tunneling microscopy on epitaxial bilayer graphene on ruthenium (0001). *Applied Physics Letters*, **94**(13), 133101.

[Sutter & Albrecht, 2013] Sutter, P, & Albrecht, Peter. 2013. Mechanical Decoupling of Graphene from Ru (0001) by Interfacial Reaction with Oxygen. *The Journal of Physical ...*, 6320–6324.

[Sutter *et al.* , 2008] Sutter, Peter W, Flege, Jan-Ingo, & Sutter, Eli a. 2008. Epitaxial graphene on ruthenium. *Nature materials*, **7**(5), 406–11.

[Tetlow *et al.* , 2014] Tetlow, H, Posthuma de Boer, J, Ford, IJ, Vvedensky, DD, Coraux, Johann, & Kantorovich, L. 2014. Growth of epitaxial graphene: Theory and experiment. *Physics Reports*.

[Tonnoir *et al.* , 2013] Tonnoir, C., Kimouche, A., Coraux, J., Magaud, L., Delsol, B., Gilles, B., & Chapelier, C. 2013. Induced Superconductivity in Graphene Grown on Rhenium. *Phys. Rev. Lett.*, **111**(Dec), 246805.

[Ugeda *et al.* , 2011] Ugeda, MM, Fernández-Torre, D, Brihuega, I, Pou, P, Martínez-Galera, AJ, Pérez, Rubén, & Gómez-Rodríguez, JM. 2011. Point defects on graphene on metals. *Physical review letters*, **107**(11), 116803.

[van Gastel *et al.* , 2009] van Gastel, R., N'Diaye, a. T., Wall, D., Coraux, J., Busse, C., Buckanie, N. M., Meyer zu Heringdorf, F.-J., Horn von Hoegen, M., Michely, T., & Poelsema, B. 2009. Selecting a single orientation for millimeter sized graphene sheets. *Applied Physics Letters*, **95**(12), 121901.

[Varykhalov *et al.* , 2008] Varykhalov, A., Sánchez-Barriga, J., Shikin, A., Biswas, C., Vescovo, E., Rybkin, A., Marchenko, D., & Rader, O. 2008. Electronic and Magnetic Properties of Quasifreestanding Graphene on Ni. *Physical Review Letters*, **101**(15), 157601.

[Varykhalov *et al.* , 2012] Varykhalov, a., Marchenko, D., Scholz, M. R., Rienks, E. D. L., Kim, T. K., Bihlmayer, G., Sánchez-Barriga, J., & Rader, O. 2012. Ir(111) Surface State with Giant Rashba Splitting Persists under Graphene in Air. *Physical Review Letters*, **108**(6), 066804.

[Vazquez de Parga *et al.* , 2008] Vazquez de Parga, a., Calleja, F., Borca, B., Passeggi, M., Hinarejos, J., Guinea, F., & Miranda, R. 2008. Periodically Rippled Graphene: Growth and Spatially Resolved Electronic Structure. *Physical Review Letters*, **100**(5), 056807.

[Vinogradov *et al.* , 2012] Vinogradov, N. a., Zakharov, a. a., Kocevski, V., Rusz, J., Simonov, K. a., Eriksson, O., Mikkelsen, a., Lundgren, E., Vinogradov, a. S., Må rtensson, N., & Preobrajenski, a. B. 2012. Formation and Structure of Graphene Waves on Fe(110). *Physical Review Letters*, **109**(2), 026101.

[Vita *et al.* , 2014] Vita, H, Böttcher, S, Horn, K, Voloshina, E N, Ovcharenko, R E, Kampen, Th, Thissen, a, & Dedkov, Yu S. 2014. Understanding the origin of band gap formation in graphene on metals: graphene on Cu/Ir(111). *Scientific reports*, **4**(111), 5704.

[Vlaic *et al.* , 2014] Vlaic, S., Kimouche, a., Coraux, J., Santos, B., Locatelli, a., & Rougemaille, N. 2014. Cobalt intercalation at the graphene/iridium(111) interface: Influence of rotational domains, wrinkles, and atomic steps. *Applied Physics Letters*, **104**(10), 101602.

[Vlieg, 1997] Vlieg, E. 1997. Integrated Intensities Using a Six-Circle Surface X-ray Diffractometer. *Journal of Applied Crystallography*, **30**(5), 532–543.

[Vlieg, 2000] Vlieg, Elias. 2000. ROD: a program for surface X-ray crystallography. *Journal of Applied Crystallography*, 401–405.

[Vlieg, 2012] Vlieg, Elias. 2012. X-ray diffraction from surfaces and interfaces. *Surface and Interface Science, Vol. 1: Concepts and Methods*, **1**, 1–48.

[Vo-Van *et al.* , 2011] Vo-Van, Chi, Kimouche, Amina, Reserbat-Plantey, Antoine, Fruchart, Olivier, Bayle-Guillemaud, Pascale, Bendiab, Nedjma, & Coraux, Johann. 2011. Epitaxial graphene prepared by chemical vapor deposition on single crystal thin iridium films on sapphire. *Applied Physics Letters*, **98**(18), 181903.

[Voigtländer *et al.* , 1991a] Voigtländer, Bert, Meyer, Gerhard, & Amer, Nabil M. 1991a. Epitaxial growth of Fe on Au (111): a scanning tunneling microscopy investigation. *Surface Science Letters*, **255**(3), L529–L535.

[Voigtländer *et al.* , 1991b] Voigtländer, Bert, Meyer, Gerhard, & Amer, Nabil M. 1991b. Epitaxial growth of thin magnetic cobalt films on Au (111) studied by scanning tunneling microscopy. *Physical Review B*, **44**(18), 10354.

[Voloshina & Dedkov, 2012] Voloshina, Elena, & Dedkov, Yuriy. 2012. Graphene on metallic surfaces: problems and perspectives. *Physical chemistry chemical physics : PCCP*, **14**(39), 13502–14.

[Voloshina *et al.* , 2013] Voloshina, Elena N, Fertitta, Edoardo, Garhofer, Andreas, Mittendorfer, Florian, Fonin, Mikhail, Thissen, Andreas, & Dedkov, Yu S. 2013. Electronic structure and imaging contrast of graphene moire on metals. *Scientific reports*, **3**(1072).

[Wang *et al.* , 2012] Wang, Bo, Yoon, Bokwon, Ko¨nig, Michael, Fukamori, Yves, Esch, Friedrich, Heiz, Ueli, & Landman, Uzi. 2012. Size-Selected Monodisperse Nanoclusters on Supported Graphene: Bonding, Isomerism, and Mobility. *Nano letters*, **12**(11), 5907–5912.

[Wang *et al.* , 2013] Wang, Lu, Zhang, Xiuyun, Chan, Helen LW, Yan, Feng, & Ding, Feng. 2013. Formation and healing of vacancies in graphene chemical vapor deposition (CVD) growth. *Journal of the American Chemical Society*, **135**(11), 4476–4482.

[Weiss *et al.* , 2005] Weiss, N, Cren, T, Epple, M, Rusponi, S, Baudot, G, Rohart, S, Tejeda, Antonio, Repain, Vincent, Rousset, Sylvie, Ohresser, P, *et al.* . 2005. Uniform magnetic properties for an ultrahigh-density lattice of noninteracting Co nanostructures. *Physical review letters*, **95**(15), 157204.

[Westwater *et al.* , 1997] Westwater, John, Gosain, DP, Tomiya, S, Usui, S, & Ruda, H. 1997. Growth of silicon nanowires via gold/silane vapor–liquid–solid reaction. *Journal of Vacuum Science & Technology B*, **15**(3), 554–557.

[Wintterlin & Bocquet, 2009] Wintterlin, J., & Bocquet, M.-L. 2009. Graphene on metal surfaces. *Surface Science*, **603**(10-12), 1841–1852.

[Woods *et al.* , 2001] Woods, SI, Kirtley, JR, Sun, Shouheng, & Koch, RH. 2001. Direct investigation of superparamagnetism in Co nanoparticle films. *Physical review letters*, **87**(13), 137205.

[Xia *et al.* , 2009] Xia, Younan, Xiong, Yujie, Lim, Byungkwon, & Skrabalak, Sara E. 2009. Shape-Controlled Synthesis of Metal Nanocrystals: Simple Chemistry Meets Complex Physics. *Angewandte Chemie International Edition*, **48**(1), 60–103.

[Xu *et al.* , 2008] Xu, Chao, Wang, Xin, & Zhu, Junwu. 2008. Graphene- metal particle nanocomposites. *The Journal of Physical Chemistry C*, **112**(50), 19841–19845.

[Yazyev & Pasquarello, 2010] Yazyev, Oleg V, & Pasquarello, Alfredo. 2010. Metal adatoms on graphene and hexagonal boron nitride: Towards rational design of self-assembly templates. *Physical Review B*, **82**(4), 045407.

[Ye *et al.* , 2010] Ye, Xingchen, Collins, Joshua E, Kang, Yijin, Chen, Jun, Chen, Daniel TN, Yodh, Arjun G, & Murray, Christopher B. 2010. Morphologically controlled synthesis of colloidal upconversion nanophosphors and their shape-directed self-assembly. *Proceedings of the National Academy of Sciences*, **107**(52), 22430–22435.

[Yoo *et al.* , 2009] Yoo, EunJoo, Okata, Tatsuhiro, Akita, Tornoki, Kohyama, Masanori, Nakamura, Junji, & Honma, Itaru. 2009. Enhanced electrocatalytic activity of Pt subnanoclusters on graphene nanosheet surface. *Nano letters*, **9**(6), 2255–2259.

[Yoon *et al.* , 2011] Yoon, Duhee, Son, Young-Woo, & Cheong, Hyeonsik. 2011. Negative thermal expansion coefficient of graphene measured by Raman spectroscopy. *Nano letters*, **11**(8), 3227–31.

[Yu *et al.* , 2008] Yu, Qingkai, Lian, Jie, Siriponglert, Sujitra, Li, Hao, Chen, Yong P., & Pei, Shin-Shem. 2008. Graphene segregated on Ni surfaces and transferred to insulators. *Applied Physics Letters*, **93**(11), 113103.

[Zakharchenko *et al.* , 2009] Zakharchenko, K., Katsnelson, M., & Fasolino, a. 2009. Finite Temperature Lattice Properties of Graphene beyond the Quasiharmonic Approximation. *Physical Review Letters*, **102**(4), 046808.

[Zhang *et al.* , 2009] Zhang, Hui, Fu, Qiang, Cui, Yi, Tan, DaLi, & Bao, XinHe. 2009. Fabrication of metal nanoclusters on graphene grown on Ru (0001). *Chinese Science Bulletin*, **54**(14), 2446–2450.

[Zhang *et al.* , 2010] Zhang, Yi, Gomez, Lewis, Ishikawa, Fumiaki N., Madaria, Anuj, Ryu, Koungmin, Wang, Chuan, Badmaev, Alexander, & Zhou, Chongwu. 2010. Comparison of Graphene Growth on Single-Crystalline and Polycrystalline Ni by Chemical Vapor Deposition. *The Journal of Physical Chemistry Letters*, **1**(20), 3101–3107.

[Zhou *et al.* , 2010] Zhou, Zihao, Gao, Feng, & Goodman, D Wayne. 2010. Deposition of metal clusters on single-layer graphene/Ru (0001): Factors that govern cluster growth. *Surface Science*, **604**(13), L31–L38.

[Zi-Pu *et al.* , 1987] Zi-Pu, H, Ogletree, DF, Hove, MA Van, & Somorjai, GA. 1987. LEED theory for incommensurate overlayers: Application to graphite on Pt (111). *Surface Science*, **180**(1985), 402–414.